PolyPublie
Polytechnique Montréal

POLYTECHNIQUE MONTRÉAL
UNIVERSITÉ D'INGÉNIERIE

Titre: Title:	Integral equation techniques for analysis of NRD-guide based millimeter-wave circuits
Auteur: Author:	Duochuan Li
Date:	2005
Type:	Mémoire ou thèse / Dissertation or Thesis
Référence: Citation:	Li, D. (2005). Integral equation techniques for analysis of NRD-guide based millimeter-wave circuits [Thèse de doctorat, École Polytechnique de Montréal]. PolyPublie. https://publications.polymtl.ca/7562/

Document en libre accès dans PolyPublie
Open Access document in PolyPublie

URL de PolyPublie: PolyPublie URL:	https://publications.polymtl.ca/7562/
Directeurs de recherche: Advisors:	
Programme: Program:	Non spécifié

Ce fichier a été téléchargé à partir de PolyPublie, le dépôt institutionnel de Polytechnique Montréal
This file has been downloaded from PolyPublie, the institutional repository of Polytechnique Montréal

https://publications.polymtl.ca

UNIVERSITÉ DE MONTRÉAL

INTEGRAL EQUATION TECHNIQUES FOR ANALYSIS OF NRD-GUIDE BASED MILLIMETER-WAVE CIRCUITS

DUOCHUAN LI
DÉPARTEMENT DE GÉNIE ÉLECTRIQUE
ÉCOLE POLYTECHNIQUE DE MONTRÉAL

THÈSE PRÉSENTÉE EN VUE DE L'OBTENTION
DU DIPLÔME DE PHILOSOPHIAE DOCTOR (Ph.D.)
(GÉNIE ÉLECTRIQUE)

AUGUST 2005

© Duochuan Li, 2005

Library and Archives Canada

Published Heritage Branch

395 Wellington Street
Ottawa ON K1A 0N4
Canada

Bibliothèque et Archives Canada

Direction du Patrimoine de l'édition

395, rue Wellington
Ottawa ON K1A 0N4
Canada

Your file Votre référence
ISBN: 978-0-494-17003-8
Our file Notre référence
ISBN: 978-0-494-17003-8

NOTICE:
The author has granted a non-exclusive license allowing Library and Archives Canada to reproduce, publish, archive, preserve, conserve, communicate to the public by telecommunication or on the Internet, loan, distribute and sell theses worldwide, for commercial or non-commercial purposes, in microform, paper, electronic and/or any other formats.

The author retains copyright ownership and moral rights in this thesis. Neither the thesis nor substantial extracts from it may be printed or otherwise reproduced without the author's permission.

AVIS:
L'auteur a accordé une licence non exclusive permettant à la Bibliothèque et Archives Canada de reproduire, publier, archiver, sauvegarder, conserver, transmettre au public par télécommunication ou par l'Internet, prêter, distribuer et vendre des thèses partout dans le monde, à des fins commerciales ou autres, sur support microforme, papier, électronique et/ou autres formats.

L'auteur conserve la propriété du droit d'auteur et des droits moraux qui protège cette thèse. Ni la thèse ni des extraits substantiels de celle-ci ne doivent être imprimés ou autrement reproduits sans son autorisation.

In compliance with the Canadian Privacy Act some supporting forms may have been removed from this thesis.

While these forms may be included in the document page count, their removal does not represent any loss of content from the thesis.

Conformément à la loi canadienne sur la protection de la vie privée, quelques formulaires secondaires ont été enlevés de cette thèse.

Bien que ces formulaires aient inclus dans la pagination, il n'y aura aucun contenu manquant.

Canada

UNIVERSITÉ DE MONTRÉAL

ÉCOLE POLYTECHNIQUE DE MONTRÉAL

Cette thèse intitulée:

INTEGRAL EQUATION TECHNIQUES FOR ANALYSIS OF NRD-GUIDE BASED MILLIMETER-WAVE CIRCUITS

Présentée par: LI Duochuan

en vue de l'obtention du diplôme de Philosophiae Doctor

a été dûment acceptée par le jury d'examen constitué de :

M. LAURIN Jean-Jackes, Ph.D., président

M. REGGIO Marcelo, Ph.D., membre

M. SEBAK Abdel, Ph.D., membre externe

M. WU Ke, Ph.D., membre et directeur de recherche

To my wife Yi Feng and my parents

ACKNOWLEDGEMENTS

I would like to warmly thank Professor Ke Wu for his guidance during the whole process of this project. I especially appreciate his confidence in me and his encouragement when I met difficulties during this project. Professor Wu has always been ready to give his generosity to discuss ideas and difficulties, to provide invaluable advice, and to share his technical experience with me. His keen technique insight and profound expertise have greatly benefited me and have been the driving force behind this research. I would also like to thank him for the financial assistance I was accorded throughout this study.

I wish to acknowledge the help of Steve Dube and Jean-Frédéric Gagné in the fabrication and measurements of the couplers. I am also grateful to other members of the laboratory support team.

My thanks also go to the research members of the Poly-Grames Reseach Center, particularly Dr. Yves Cassivi, Mr. Ping Yang, and Dr. Feng Xu for their fruitful discussions, co-operation and their friendliness.

I have learned also much from the professors and developed so many friendships in my time at Poly-Grames Research Center. I would like to thank you all for an unforgettable experience.

RÉSUMÉ

Depuis l'introduction du concept de guide d'onde diélectrique non rayonnement (guide DNR), un large éventail de guides DNR modifiés, de composants DNR et de circuits planaires hybrides DNR ont été proposés, étudiés et ont démonté des propriétés très intéressantes pour des applications dans des circuits du domaine des ondes millimétriques. Cette thèse présentera une série de techniques de résolution d'intégrales qui ont été publiées ou qui le seront [98]-[100] et permettent d'analyser des circuits d'ondes millimétriques basés sur la technologie DNR. La théorie derrière les techniques de solution par équations intégrales, comprenant les équations intégrales, les fonctions dyadiques de Green et la méthode des moments seront aussi présentées. Les avantages et les inconvénients des équations intégrales de surface et de volume, des fonctions dyadiques de Green dans les domaines spatial et spectral, de la méthode d'accord des points, de la méthode des moindres carrés et de celle de Galerkin seront abordés, en plus d'une discussion sur les différentes fonctions de base.

Les propriétés de l'onde guidée par le guide diélectrique planaire à bandes parallèles, qui comprend les guides DNR standards ainsi que le guide de type H, seront présentées. Les expressions des champs des modes LSM et LSE, comprenant les modes symétriques et antisymétriques, sont obtenues de manière analytique. Le spectre des modes du guide diélectrique planaire à bandes parallèles est divisé entre les modes d'onde de surface, les modes de radiation continue et les régions interdites. Les coefficients de couplage sont obtenus et les résultats indiquent que le couplage devient plus important pour des bandes plus étroit et pour une constante diélectrique plus faible.

Une méthode par équations intégrales pour les guides d'onde dont la section est inhomogène dans un milieu multicouches est proposée et les propriétés de l'onde guidée sont obtenues pour les guides DNR modifiés. Les conditions des modes liées et des modes de fuite d'un guide d'onde DNR simplifié sans recouvrement seront discutées. Un nouveau coupleur directionnel DNR utilisant deux guides DNR simplifiés/modifiés reliés par un pont est proposé et la constante de propagation du guide est étudiée à l'aide

d'une méthode d'équation intégrale du champ électrique. Les résultats de simulation montrent que la longueur de couplage est réduite d'environ 60% et la largeur de bande, pour une tolérance de ±0.5dB sur un couplage de 3dB, est presque doublée en comparaison avec le coupleur conventionnel lorsque la largeur du pont équivaut environ à 0.68 fois la séparation entre les plaques. L'utilisation du pont rend le coupleur mécaniquement plus stable et rend ses performances plus reproductibles. Des prototypes expérimentaux sont fabriqués et une méthode de calibrage est utilisée lors de la prise de mesure. Les avantages de ce coupleur pour les applications en ondes millimétriques sont montrés.

Une approche par intégrale de volume à ordre réduit est proposée pour modéliser et analyser les circuits à guides DNR et les guides H dans le cas d'une géométrie planaire arbitraire et de diélectriques inhomogènes. Une variation des champs en demi-sinus est utilisée de façon à ce que la discrétisation du courant pour l'intégrale de volume se fasse dans un plan. Des fonctions de base combinées de propagation et de modes locaux sont utilisées dans la méthode des moments de Galerkin afin d'analyser le spectre des guides DNR et des guides H. Une intégration verticale dans le domaine spatial est réalisée analytiquement et la fonction de Green du premier ordre est développée. De cette façon, la solution de l'intégrale de volume pour modéliser les guides DNR et H se réduit à un problème à deux dimensions. L'application de cette méthode est démontrée pour un guide DNR à bouts ouverts. De plus, les guides H à bouts ouverts, les résonateurs et un filtre à trois pôles à couplage par proximité sont modélisés et analysés. Les résultats sont en accord avec les mesures et avec les résultats des autres méthodes.

Une approche générale par équations intégrales de surface ou de volume est proposée et développée pour modéliser avec précision et analyser les circuits intégrés de type planaire hybride et à guide DNR. En étendant la méthode d'intégrale de volume à ordre réduit aux cas multimodes, une intégration verticale dans le domaine spatiale est réalisée analytiquement pour chaque mode vertical et un ensemble de fonction de Green du premier ordre est construit. Dans ce cas, la solution à l'intégrale de volume dans le

cas de circuits intégrés à guide DNR se réduit à un problème à deux dimensions pour chaque mode vertical. De cette façon, seulement les sous-matrices diagonales ont besoin d'être calculées puisque les différents modes verticaux sont orthogonaux. Une technique de calcul sur une région réduite est utilisée pour les modes verticaux élevés pour lesquels le champ est confiné aux fentes et aux régions attenantes. Des exemples seront présentés pour démontrer les propriétés et l'efficacité de la méthode proposée : un résonateur micro-ruban couplé en guide DNR, une interconnexion de circuits planaire en guide DNR et une transition intégrée entre micro-ruban et guide DNR. Les résultats correspondent bien aux mesures expérimentales et aux résultats obtenus par d'autres méthodes.

Les techniques par équations intégrales développées au cours de cette thèse sont très efficaces pour modéliser et analyser les circuits d'ondes millimétriques basés sur la technologie DNR. Ces techniques peuvent aussi être appliquées au domaine spatial et utilisées pour des circuits intégrés sur différents substrats.

ABSTRACT

Since the inception of the NRD-guide concept, a large class of modified NRD-guides, NRD-guide components, and the hybrid planar/NRD-guide integrated circuits have been proposed, studied, and shown to be promising in the design of millimeter-wave circuits and systems. In this work, a set of integral equation techniques, which has been or will be published in [98]-[100], has been developed for the analysis of NRD-guide based millimeter-wave circuits. The basic theory of integral equation technique, which comprises integral equations, dyadic Green's functions, and method of moments, are presented. The advantages and disadvantages of surface and volume integral equations, dyadic Green's functions in spatial and spectral domains, the method of point matching, least squares, and Galerkin's method, and categories of basis functions are discussed.

Guided wave properties of the dielectric strip loaded parallel plate guide, which comprises the standard NRD-guide and H-guide, are presented and discussed. The field expressions of the LSM and LSE modes, including symmetric mode and anti-symmetric modes, are obtained analytically. The mode spectrum of the dielectric strip loaded parallel-plate guide is described with a set of spectrum figures in which the spectrum space is divided into surface wave mode, continuous radiation mode, and prohibited regions. Coupled guide characteristics in terms of the coupling coefficient are obtained and the results indicate that the coupling can be enhanced for strips of smaller width and lower dielectric constant.

An electric field integral equation method for dielectric waveguides with inhomogeneous cross-section in multilayered media is formulated and the solution to the guided wave properties of the modified NRD-guides is obtained. The condition of bounded and leakage mode of a simplified modified NRD-guide without overlays is discussed. A new NRD-guide directional coupler using two NRD-guides interconnected with a bridge is proposed and the propagation constants of the structure are investigated with the electric field integral equation method. Modeling results show that the coupling

length is reduced about 60% and the bandwidth under the tolerance limits of ±0.5dB of deviation for 3dB coupling is nearly doubled with reference to its conventional counterparts when the thickness of the bridge is made around 0.68 of the plate separation. The use of a bridge can improve the mechanical stability and make the coupler performance reproducible. Experimental prototypes are fabricated and a calibration procedure is used in the measured results. Advantages of the new coupler as passive component are shown for millimeter-wave integrated circuits.

An order-reduced volume-integral equation approach is proposed for the modeling and analyzing of NRD-guide and H-guide millimeter-wave circuits that involve arbitrarily shaped planar geometry and inhomogeneous dielectric. A half-sinusoidal vertical variation of fields is used so that the discretization of current for the volume-integral equation is made in a plane. Combined basis functions of propagating and local modes are used in the Garlerkin's method of moments on the basis of spectral analysis of NRD-guide and H-guide. A vertical integration in the space domain is carried out analytically and a first-order Green's function is developed. The solution for the volume-integral equation in modeling NRD-guide and H-guide circuits is then reduced to a 2-D planar problem. The framework of this technique is demonstrated through its application to NRD-guide open-end. In addition, H-guide open-end, resonators, and a 3-pole gap-coupled filter are modeled and analyzed. The results agree with the measurements and results obtained by other methods very well.

A generalized surface-volume integral-equation approach has been proposed and developed for accurate modeling and analysis of hybrid planar/NRD-guide integrated circuits. By extending the order-reduced volume integral equation method to multi-mode case, vertical integration in space-domain is carried out analytically for each vertical mode and a set of first-order Green's functions is constructed. Then, the solution of the volume integral-equation concerning with the NRD-guide circuits has been reduced to a 2-D planar problem in connection with each vertical mode. In this way, only the diagonal sub-matrices need to be calculated due to the orthogonal property of different vertical modes. A reduced calculation region technique is used to the high vertical

modes in which the fields are confined in the slot areas and their vicinities. Examples, comprising the microstrip coupled NRD-guide resonator, NRD-guide interconnect between planar circuits, and integrated transition of microstrip-line-to NRD-guide structures, are modeled to demonstrated properties and efficiency of the proposed method. The results are in good agreement with measured results or the results obtained with other methods.

Integral equation techniques developed in this thesis are very efficient for modeling and analysis the NRD-guide based millimeter-wave circuits. These techniques also can be realized in space-domain and can be used to new substrate integrated circuits.

CONDENSÉ EN FRANÇAIS

TECHNIQUE PAR ÉQUATIONS INTÉGRALES POUR L'ANALYSE DE CIRCUITS D'ONDES MILLIMÉTRIQUES FABRIQUÉS AVEC LA TECHNOLOGIE DES GUIDES DNR

1. Introduction

Les faibles pertes en transmission ainsi que l'absence de radiation aux discontinuités et aux virages sont les deux caractéristiques importantes de la technologie des guides DNR qui permettent de réaliser des circuits d'ondes millimétriques compacts et de haute performance. Depuis l'introduction du concept de guide DNR, un large éventail de guides DNR modifiés, de composants DNR et de circuits intégrés hybrides DNR ont été proposés et étudiés et démontrent des caractéristiques prometteuses pour les applications en ondes millimétriques. Cependant, les techniques numériques utilisées pour analyser les circuits en technologie DNR sont très spécifiques ou demandent une puissance de calcul très élevée. Dans cette thèse, une série de techniques par équations intégrales, qui ont ou seront publiées [98]-[100], ont été développées pour l'analyse des circuits à base de la technologie des guides DNR dans le domaine des ondes millimétriques.

2. Présentation de la technique par équations intégrales

La technique par équations intégrales, comprenant des équations intégrales, des fonctions de Green dyadiques et la méthode des moments, est particulièrement avantageuse dans les cas comportant des régions homogènes ou ouvertes. Les équations intégrales, de surface et de volume, sont obtenues en utilisant le principe d'équivalence ou en imposant les conditions aux frontières. Les fonctions de Green dyadiques pour un milieu homogène ou un milieu multicouches sont obtenues dans les domaines temporel et spatial. La méthode des moments (MdM) est utilisée afin de discrétiser les équations intégrales et les méthodes d'accord des points, des moindres carrés et de Galerkin sont

considérées comme trois cas particuliers. Une discussion sur le choix des fonctions de base est présentée en fonction des propriétés du domaine complet et de sous-sections, ainsi que celles des fonctions de base d'ordre faible ou élevé. Les avantages et inconvénients des équations intégrales de volume, de l'intégration numérique dans les domaines spatial et temporel ainsi que ceux des différentes catégories de fonction de base seront discutés.

3. Propriétés de l'onde guidée dans un guide DNR standard ou dans un guide H

Les propriétés de l'onde guidée par le guide diélectrique planaire à bandes parallèles, qui comprend les guides DNR standards ainsi que le guide de type H, seront présentées. Les modes propres de ce type de guide peuvent être divisés en un nombre entier d'ondes de surface, les modes LSE et LSM, et un ensemble continu de modes radiatifs. Dans un diélectrique homogène et sans pertes, les champs électriques (E) et magnétiques (H) peuvent être décrits chacun par un potentiel vecteur. En remplaçant le potentiel vecteur par un potentiel scalaire, les expressions de mode LES et LSM peuvent être obtenues analytiquement, y compris les modes symétriques et antisymétriques.

Dans un guide diélectrique planaire à bandes parallèles, la présence des bandes métalliques parallèles entraîne une discrétisation du nombre d'onde vertical m (m est nul ou entier) alors que le nombre d'onde horizontal s'obtient à partir d'une équation transcendante reliée au guide diélectrique. Le spectre des modes du guide diélectrique planaire à bandes parallèles est décrit par un spectre de figures dont l'espace spectral est divisé entre les modes d'ondes de surface, les modes de radiation continue et les régions interdites. Le mode de propagation radiative m=o peut exister pour toutes les fréquences et peut provoquer des pertes radiatives dans les guides DNR et les circuits intégrés planaires hybrides DNR. Dans la région où $a/\lambda 0<0.5$, le mode de radiation continu m=1 devient complètement évanescent et la structure se comporte comme un guide DNR alors que dans la région $a/\lambda 0>0.5$, le mode est en partie évanescent et en partie propagatif, la structure se comporte alors comme un guide H.

Le couplage entre deux guides DNR parallèles est dû à l'interaction entre les champs à décroissance exponentielle, il est donc sensible à la distance séparant les deux guides et à la longueur du coupleur. Le coefficient de couplage en fonction de l'espacement des bandes, normalisé par rapport à la longueur d'onde dans le vide, est obtenu pour trois constantes diélectriques différentes, soit ε_r=2.04, 2.56 et 9.5. Les résultats indiquent que le couplage devient plus important pour des bandes plus minces et pour une constante diélectrique plus faible.

4. Solution par équation intégrale des propriétés de l'onde guide pour les guides DNR modifiés

Une équation intégrale du champ électrique (EICE) pour les guides d'ondes diélectriques à section inhomogène dans un milieu multicouches est formulée. Elle est réduite à une équation intégrale en deux dimensions pour la section du guide en utilisant une transformation de Fourier sur la variable axiale. L'équation est utilisée pour un guide DNR générique modifié dans lequel une bande diélectrique à constante élevée et de forme arbitraire est placée en sandwich entre deux couches d'un diélectrique à constante plus faible recouvrant des plaques conductrices. La fonction de Green dyadique est obtenue en considérant le coefficient de réflexion aux deux interfaces air-diélectrique; celui du haut et celui du bas. L'équation intégrale est résolue par la méthode de moments de Galerkin en utilisant des fonctions de base de type impulsion. La constante de propagation β peut alors être obtenue en fixant le déterminant de la matrice d'impédance Z à zéro.

La valeur de β peut soit être un nombre réel pour les modes liés ou un nombre complexe dans le cas des modes à fuites, le mode apparaissant dépendamment de la forme de la bande diélectrique et du recouvrement. Dans un guide DNR simplifié modifié sans le recouvrement, le pôle de la composante $\hat{\mathbf{z}}\hat{\mathbf{z}}$ de la fonction de Green correspond au mode fondamental de la plaque parallèle qui peut causer des pertes dans la structure. De manière générale, les pertes ne peuvent exister dans un guide DNR simplifié modifié qui possède une symétrie verticale, les pertes n'apparaissent que si la

symétrie est brisée. Au cours de l'intégration numérique, l'intégrande possède un comportement d'oscillations rapides dont l'amplitude décroît en $1/k_y^v$. Une technique asymptotique est utilisée pour atteindre la convergence plus rapidement.

Comme exemple d'application importante, un nouveau coupleur directionnel DNR utilisant deux guides DNR simplifiés/modifiés reliés par un pont est proposé et la constante de propagation du guide est étudiée à l'aide d'une méthode d'équation intégrale du champ électrique. Les résultats de simulation montrent que la longueur de couplage est réduite d'environ 60% et la largeur de bande, pour une tolérance de ±0.5dB sur un couplage de 3dB, est presque doublée en comparaison avec le coupleur conventionnel lorsque la largeur du pont équivaut environ à 0.68 fois la séparation entre les plaques. Par contre, des modes d'ordre élevé à l'intérieur de la bande passante autour de 77 GHz pourraient se propager si l'épaisseur du pont devient trop grande. En considérant la longueur de couplage, la largeur de bande et la bande d'opération à un seul mode, la rapport optimum c/a est entre 0.4 et 0.68. Le pont mince permet aussi la réduction de la réflexion à la jonction entre le bras d'alimentation du coupleur et la section couplée où est situé le pont. Pour cette structure, le niveau de couplage peut être ajusté non seulement en variant la distance entre les deux guides, mais aussi en ajustant l'épaisseur du pont. De plus, l'utilisation du pont rend le coupleur mécaniquement plus stable et rend ses performances plus reproductibles.

Des prototypes expérimentaux coupleurs DNR conventionnels et du nouveau design incluant le pont sont fabriqués avec deux coudes de 90o pour les bras. L'épaisseur du pont a été choisie à c/a=0.5 et le coupleur se termine aux deux extrémités par des sections trapézoïde/demi-cercle. Une procédure de calibrage est ensuite utilisée afin d'adapter le guide DNR au guide rectangulaire utilisé pour prendre les mesures. Les avantages de ce coupleur comme élément de circuit d'ondes millimétriques passif sont vérifiés expérimentalement.

5. Une approche par équation intégrale de volume à ordre réduit pour les circuits d'ondes millimétriques en guide DNR et guide H

Une approche par équation intégrale de volume à ordre réduit (EIVOR) est proposée pour la modélisation et l'analyse de circuits d'ondes millimétriques en guide DNR ou H comportant une géométrie planaire arbitraire et un diélectrique inhomogène. Avec une excitation du mode vertical m=1, seuls les modes m=1, incluant les modes d'ondes de surface et les modes de radiation continue, apparaissent dans le circuit à cause de l'orthogonalité des modes m. Une variation des champs en demi-sinus ($\sin(\pi(z+a)/a)$ pour les composantes x et y et $\cos(\pi(z+a)/a)$ pour la composante z) reste inaltérée dans le circuit en entier et la discrétisation du courant peut se faire dans le plan parallèle uniquement. Les modes d'ondes de surface qui se propagent peuvent être utilisés comme fonctions de base des modes propagatifs dans les lignes d'alimentation et le champ restant peut être représenté par des fonctions de base de modes locaux qui peuvent représenter un mode complet ou une sous-section de mode. En utilisant les modes locaux comme fonction de test, l'équation intégrale de volume est résolue en utilisant la méthode des moments de Galerkin. Les valeurs de la matrice du système peuvent être obtenues par une intégration du domaine spectral tout en conservant la partie verticale dans le domaine spatial. Une nouvelle fonction de Green avec m=1 est construite afin de résoudre analytiquement l'intégration dans le domaine spatial. Finalement, la solution de l'équation intégrale de volume pour les circuits à guide DNR ou H a été réduite à un problème de modélisation en deux dimensions.

La nouvelle fonction de Green avec m=1 dans le problème à deux dimensions est beaucoup plus simple que la fonction pour le problème tridimensionnelle, non seulement parce que la variable dans la direction verticale est éliminée par l'intégration analytique, mais aussi parce que les fonction triangulaires complexes sont remplacées par des fonctions algébriques simples. Seuls les pôles m=1 apparaissent dans cette fonction de Green quand $a/\lambda_0 > 0.5$, les autres pôles, en particulier m=0, sont éliminés.

Lorsqu'il n'y a pas de pôles dans la fonction de Green comme dans le cas de guides DNR, il est plus efficace d'effectuer l'intégration en coordonnées cartésiennes plutôt que polaires puisque l'intégrande oscille sinusoïdalement. Une technique asymptotique est aussi utilisée pour rendre l'intégration numérique plus efficace.

La technique EIVOR peut être utilisée pour calculer plusieurs caractéristiques de composantes de guides d'ondes et de circuits multiports comme les fréquences de résonance et les paramètres S. L'application de cette méthode est démontrée pour un guide DNR à bouts ouverts. Une excitation sous forme d'onde progressive est appliquée avec succès à la ligne d'alimentation, ce qui est important pour l'analyse de circuit DNR multiports.

Dans le cas d'un guide H à bout ouvert, le pôle m=1 apparaît dans la fonction de Green et l'intégration numérique doit se faire en coordonnées polaires. À mesure que la fréquence augmente, le coefficient de réflexion diminue très rapidement à cause des pertes radiatives.

L'approche EIVOR peut être facilement utilisée pour analyser des résonateurs DNR en fixant le terme d'excitation à zéro. Les caractéristiques de quatre résonateurs planaires à section rectangulaire ont été calculées afin de les comparer aux résultats mesurés de manière à valider la méthode. Ensuite, un résonateur à section carrée à encoche et un résonateur inhomogène sont modélisés pour démontrer la capacité de cette approche dans le cas d'une géométrie planaire arbitraire et d'un diélectrique dont la permittivité varie selon les coordonnées x et y.

Un filtre guide DNR à trois pôles à couplage par proximité est modélisé en tant que structure entière pour déterminer ses fréquences caractéristiques. L'accord entre les résultats calculés et mesurés est bon au sujet pertes d'insertion.

6. Une approche généralisée par équation intégrale de surface-volume pour l'analyse des circuits intégrés hybrides planaires à guides DNR

Une approche générale par équations intégrales de surface ou de volume est proposée et développée pour modéliser avec précision et analyser les circuits intégrés de type planaire hybride et à guide DNR. En utilisant une équation intégrale de surface du champ électrique, dans le cas d'un circuit micro-ruban, une équation intégrale de surface du champ magnétique pour les plans à fentes, dans le cas des circuits à fentes ou coplanaires et une intégrale de volume pour les circuits DNR, des équations intégrales

de volume-surface peuvent être formulées pour les circuits hybrides planaires DNR. En utilisant une excitation de courant magnétique équivalent provenant des fentes dans la plaque métallique, non seulement le mode d'opération m=1, mais aussi le mode radiatif m=0 et les modes évanescents m≥2 sont excités simultanément. En étendant la méthode EIVOR aux cas multimodes, la discrétisation du courant pour les guides DNR est effectuée sous forme planaire pour chaque mode vertical. Ensuite, l'intégration verticale dans le domaine spatial est faite analytiquement pour chaque mode vertical et un ensemble de fonctions de Green du premier ordre est construit. Finalement, la solution à l'intégrale de volume dans le cas de circuits intégrés à guide DNR se réduit à un problème à deux dimensions pour chaque mode vertical. De cette façon, seulement les sous-matrices diagonales ont besoin d'être calculées puisque les différents modes verticaux sont orthogonaux. Une technique de calcul sur une région réduite est utilisée pour les modes verticaux élevés pour lesquels le champ est confiné aux fentes et aux régions attenantes. De façon générale, seulement quelques modes verticaux sont nécessaires pour les structures hybrides. Dans les nouvelles fonctions de Green, les pôles n'existent que pour la fonction de Green de premier ordre m=0, ce qui correspond au mode radiatif m=0. Puisqu'il n'y a pas de pôles dans les intégrales pour les modes m≥1, elles peuvent être résolues en coordonnées cartésiennes avec une convergence rapide grâce au comportement d'oscillations sinusoïdales. La demande en puissance de calcul est considérablement réduite par rapport à la méthode d'équations intégrales de surface-volume (EISV) conventionnelle, ce qui rend cette approche très efficace pour les circuits hybrides planaires DNR.

L'utilité de la méthode et son application sont démontrées pour trois circuits différents en technologie hybride. Pour le résonateur micro-ruban couplé DNR, seulement deux modes verticaux (M=1) suffisent puisque les fentes ne touchent pas au diélectrique, ce qui rend le champ des modes m≥2 très petit dans la région diélectrique. De cette façon, la demande en puissance de calcul est réduite considérablement avec moins de modes verticaux. Cependant, dans le cas d'une interconnexion entre un guide DNR et un circuit planaire, il faut jusqu'à treize modes (M=12) pour assurer la

convergence puisque les modes élevés sont concentrés entre les deux fentes. La technique de calcul en région réduite est essentielle pour modéliser cette structure avec plus de modes verticaux. Généralement, M=5 permet une assez grande précision sur toute la bande de fréquences dans le cas d'une structure de transition micro-ruban vers guide DNR.

Ces résultats numériques sont en bon accord avec les mesures expérimentales et les résultats obtenus par d'autres méthodes. Comparativement à des logiciels commerciaux tels que Ansoft-HFSS, cette méthode n'exige non seulement moins de temps de calculs, mais permet aussi d'obtenir plus d'informations sur la structure, notamment les pertes radiatives m=0 et la distribution du champ de chaque mode vertical.

7. Conlusions

Les techniques par équations intégrales développées dans cette thèse sont très efficaces pour modéliser et analyser les circuits d'ondes millimétriques en technologie DNR. La méthode EICE peut s'appliquer aux structures ouvertes ou fermées et permet de décrire des phénomènes physiques comme les fuites. L'approche EIVOR réduit le problème tridimensionnel en problème à deux dimensions, simples dans le cas de circuit à guide DNR ou H. La méthode générale EISV développée réduit considérablement la puissance de calcul requise pour modéliser les circuits hybrides planaires DNR. Ces techniques peuvent aussi être utilisées dans le domaine spatial et appliquées à de nouveaux substrats.

TABLE OF CONTENTS

LIST OF TABLES

LIST OF FIGURES

LIST OF ABBREVIATIONS

BEM	Boundary Element Method
CFIE	Combined Field Integral Equation
CPW	Co-Planar Waveguide
DGF	Dyadic Green's Function
EFIE	Electric Field Integral Equation
FDTD	Finite-Difference Time Domain
FEM	Finite Element Method
LSE	Longitudinal Sectional Electric
LSM	Longitudinal Sectional Magnetic
MFIE	Magnetic-Field Integral Equation
MoM	Method of Moments
MPIE	Mixed Potential integral Equation
NRD	Non-Radiative Dielectric
ORVIE	Order-Reduced Volume Integral Equation
PEC	Perfect Electric Conductor
SIC	Substrate Integrated Circuit
SINRD	Substrate Integrated Non-radiative Dielectric
SIRW	Substrate Integrated Rectangular Waveguide
SVIE	Surface-Volume Integral Equation
TE	Transverse Electric
TLGF	Transmission Line Green's Function
TLM	Transmission Line Method
TM	Transverse Magnetic
3-D	Three Dimensional
2-D	Two Dimensional

LIST OF SYMBOLS

f	frequency
C	coupling coefficient
V	voltage
I	current
L_c	coupling length
E	electric intensity
H	magnetic intensity
J	electric current density
Γ	voltage reflection coefficient
α	evanescent constant
β	propagation constant
λ_0	wavelength of vacuum
λ	wavelength
$\overline{I}$	identity operator
$\Im$	a linear operator
$\Re$	a compact operator
$\eta = \sqrt{\mu/\varepsilon}$	intrinisic impedance
ε	capacitivity of the medium
ε_0	permittivity of vacuum
ε_r	dielectric constant or relative compacitivity
μ_0	permeability of vacuum
μ	inductivity of the medium
σ	conductivity of the medium
$k = \omega\sqrt{\mu\varepsilon}$	wavenumber
ω	angle frequency
ϕ^e	electric scalar potential function

ϕ^h	magnetic scalar potential function
ζ	decay constant in the air region
β_y	y-directed propagation constant in the dielectric region
$\bar{\mathbf{G}}$	dyadic Green's function in space domain
$\tilde{\bar{\mathbf{G}}}$	dyadic Green's function in spectral domain
$\bar{\mathbf{Z}}$	impedance matrix

CHAPTER 1

INTRODUCTION

1.1 Millimeter-wave Integrated Circuits

Millimeter-wave techniques have become increasingly important in recent years because of emerging wireless communications and non-communication applications [1], [2]. Over this frequency range, the commonly used planar techniques, such as stripline, microstrip, slotline, coplanar waveguide, and finline, suffer from problems of prohibitive conductor loss and critical dimensional tolerance. Therefore, non-planar technologies, which include mainly metallic and dielectric waveguides, should be considered. Presently, metallic waveguides are widely used in most practical millimeter wave components and systems. However, metallic waveguides are bulky and cannot provide a high-level circuit integration. Most dielectric waveguides [3], [4], such as image guides, H-guides, are found to have a relatively low propagation loss and may provide a high-level of integration. On the other hand, they are difficult to use for comprehensive circuit configurations involving discontinuities, sharp bends, and truncations due to radiation. From the electromagnetic-field point-of-view, this radiation loss is obvious as the waveguide is theoretically made in an open environment. This perception was held until the invention of non-radiative dielectric (NRD) waveguide which can effectively suppress the radiation loss along circuit bends and discontinuities. Since its inception in 1981 [5], the NRD-guide technology has been used in the design and fabrication of a large class of integrated circuits and antennas that have demonstrated superior electrical performance at millimeter wave frequencies [6]-[12].

Non-planar circuits exhibit advantages at higher frequencies for their low loss properties. However, they generally present some difficult problems when active device integration is required. Obviously, the hybrid scheme based on combined planar circuit and non-planar circuit technology is an attractive choice for practical circuit design.

Based on this consideration, many types of hybrid planar/non-planar integration technologies were proposed as building blocks for constructing microwave and millimeter-wave circuits. A number of techniques of planar circuits integrated with rectangular waveguides have been reported [13]-[17]. However, they may not be so attractive for widespread applications because of their poor transition properties and low-level integrations. On the other hand, dielectric waveguides have received little attention because of the two fundamental problems of a dielectric waveguide: radiation loss due to discontinuity and difficult transition to planar circuits [18]. Therefore, the hybrid planar/NRD-guide integrated circuits are more appealing because of the non-radiative and easy for integration properties of NRD-guide circuits [19]-[22]. This hybrid technology offers a unique possibility of exploiting the complementary advantages of each individual building block while eliminating (at least partly if not completely) inherent drawbacks.

1.2 NRD-Guide Based Microwave and Millimeter-wave Integrated Circuits

NRD-guide plays an important role in the development of millimeter-wave circuits because of its non-radiative properties in bends and discontinuities. In this section, we will discuss the NRD guide based millimeter-wave circuits that include the standard and modified NRD-guides, NRD-guide discontinuities and components, and the hybrid planar/NRD-guide integrated circuits. The NRD-guide antennas are well discussed in [23] and are therefore not included in this thesis.

1.2.1 Standard NRD-Guide

The standard NRD-guide, which was proposed by Yonyama and Nishida [5], consists of a parallel-plate guide with a dielectric strip inserted between the plates as in Fig. 1.1. Structurally, it is identical to the H-guide except that the plate separation is less than half the free-space wavelength ($\lambda_0/2$).

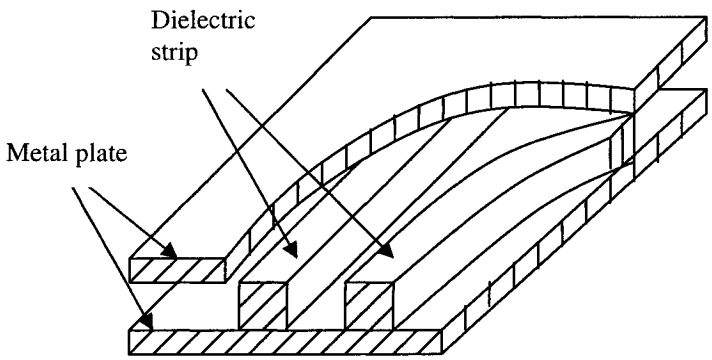

Fig. 1.1. Geometry of NRD-guide.

In a parallel-plate guide with air as the intervening medium, the TM modes, which have the electric fields parallel to the metal plates, form the low-loss modes. For a plate separation less than $\lambda_0/2$, these TM modes are cut off. In the NRD guide, the presence of the dielectric strip enables electromagnetic waves to propagate along the strip whereas the radiated waves, if any, are suppressed because of the cutoff nature of the air-filled region.

The above two important features of the NRD guide, namely, low transmission loss and absence of radiation from bends and discontinuities make it suitable for realizing compact and high-performance millimeter wave integrated circuits. Considering the physical size of guide and the convenience of fabrication, the most useful frequency range for practical applications is 30 GHz to about 100 GHz. The guided wave properties of standard NRD-guide and coupled NRD-guide are discussed in Chapter 3.

1.2.2 **Modified NRD-Guides**

Besides the standard NRD-guide, several types of modified NRD guides have also been proposed to fit various millimeter-waves applications.

An insulated NRD-guide [24], as shown in Fig. 1.2(a), is a high-dielectric strip sandwiched between low-dielectric overlays on conducting plates. These overlays not only reduce transmission losses, but also suppress the generation of unwanted higher modes. The radiation from being generated at bends and discontinuities can be avoided when the separation of the conducting plates is smaller than a certain critical value determined by the dielectric constant and thickness of the overlays. The improved design of a dielectric waveguide can successfully eliminate most difficulties associated with the high-dielectric NRD-guide without spoiling the non-radiative nature of the waveguide itself.

The groove NRD guide [25]-[27], the cross-section of which is shown in Fig. 1.2(b), is another useful variation of the NRD-guide which enables the dielectric strip to be positioned properly. Besides acting as a support for the dielectric strip, the grooves help in enhancing the field concentration in the dielectric strip. With dielectric strips of lower dielectric constant, the useful bandwidth of a groove NRD-guide is higher than that of the standard NRD-guide.

A channelized NRD-guide [28], [29], whose cross-section is shown in Fig. 1.2(c), consists of a core NRD-strip that is simply surrounded by dielectric media other than air with lower dielectric constant. In this way, the non-radiating condition can be well respected as long as the two metallic plates are separated by a distance smaller than a half wavelength of the TM parallel plate mode intrinsic to the surrounding media. The channelized NRD-guide forms a composite dielectric geometry and can be used to operate down to lower microwave frequencies, say, below 20 GHz with reasonable geometrical compactness if high dielectric constants are used in the building blocks.

The effect of an air gap between the top metal plate and the dielectric strip in NRD-guide, as shown in Fig. 1.2 (d), was studied in [30]. In this structure, leakage is produced in the form of a TEM wave that propagates away at an angle from the dielectric strip on both sides. The leakage from small gaps can cause crosstalk between neighboring components. However, when the gap size is large, the leakage is so strong that this structure can furnish a new type of leaky wave antenna for millimeter-waves.

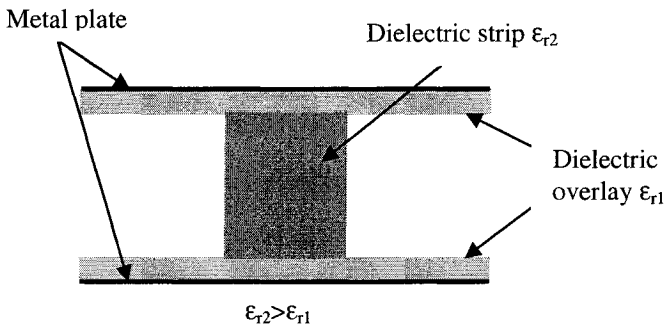

(a)

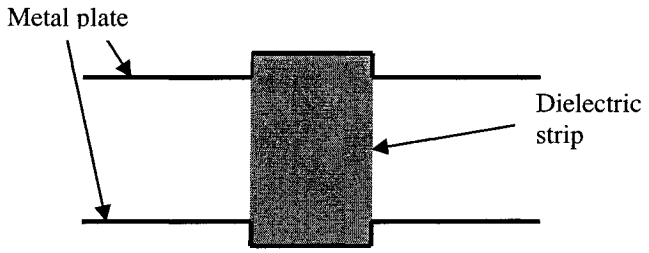

(b)

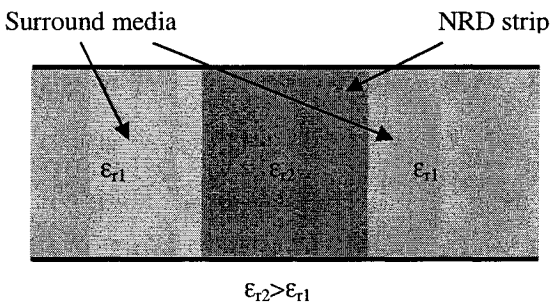

(c)

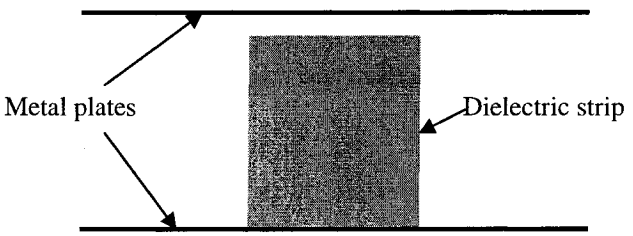

(d)

Fig. 1.2. The cross-sections of modified NRD-guides. (a) Insulated NRD-guide. (b) Groove NRD-guide. (c) Channelized NRD-guide. (d) NRD-guide with an air gap.

Other modified NRD-guides, such as engraved NRD-guide [31], [32], NRD-guide with a pseudochiral Ω-slab [33], are also good candidates for millimeter-wave circuits. In chapter 4, an integral equation solution is presented for the analysis of the guided wave properties for a generalized modified NRD-guide in which an arbitrarily shaped dielectric strip is sandwiched between low dielectric overlays on conducting plates.

1.2.3 **NRD-Guide Discontinuities and Components**

The inherent advantages of the NRD guide especially at high frequencies have led to the development of various NRD-guide circuit components, such as resonators, filters, couplers, circulators, terminators, and power combiners. The realization of these NRD-guide components invariably involves the incorporation of discontinuities in the form of an open end, a gap, a step, a bend, a right angle elbow, and so on. In this section, a discussion regarding NRD-guide discontinuities and components using different configuration is presented.

Since there is no radiation loss in the bends in an NRD-guide, the main cause of the bending loss was found to be due to the reflection and mode conversion at the transitions between the straight and curved waveguides [34], [35]. The bending loss could be totally nullified by a proper choice of dielectric strip width for a given radius of curvature of the bend. The critical width can be adopted as a design criterion for a low loss and very sharp NRD-guide bend. A further study in [36] shows that the unwanted parasitic mode due to mode conversion can be suppressed by adjusting properly the phase constant difference $\Delta\beta$ between LSM- and LSE-modes in a bend with arbitrary radius of curvature. In order to change $\Delta\beta$, it is found to be effective to locate a metal rod or ring near the bend.

A class of discontinuities in the form of open ends, junctions, steps, and gaps were studied in [37]. Mode conversion and power transfer among principal NRD-guide modes are, in particular, characterized for the design consideration of NRD-guide

components and circuits. The presence of an NRD-guide taper can greatly reduce the reflection in the transition from rectangular to NRD-guide [38]. The right angle elbow was studied in [39] and indicates that the input power of LSM_{11} mode can almost completely be converted into LSE_{11} mode in the output arm by properly adjusting the positions of the ends of the two arms.

An NRD-guide T-junction which incorporates a dielectric stub as an extension of the main arm and the rectangular metal patches on the free surfaces of the main arm as matching elements were proposed in [40]. A practical T-junction of this type was reported to offer well-balanced power outputs of more than -4dB over a bandwidth of 2 GHz centered at 35 GHz. On the analysis with a mode-matching method, the T-junction is optimized to reach the maximum power transfer from LSM to LSE mode [41]. The LSM_{11} mode at the input is equally divided in amplitude in two LSE_{11} modes at outputs with an attenuation of 3.18dB.

It is possible to use low cost materials of low permittivity like Teflon ($\varepsilon_r = 2.04$) to design high-Q NRD-guide resonator with reduced radiation loss. The nonradiative nature of the structure prevents leakage and coupling with other external components, and thus the Q-factor is limited almost only by material losses. The size of resonator is larger due to the use of low permittivity materials allowing the designer to have a larger mechanical tolerance. The resonator can be built in either cylindrical or cubic form with the added advantages of symmetry in the latter case. High-frequency stability of the resonator can also be achieved through the use of a temperature-stabilized material such as the Roger's TMM dielectric materials. Several types of NRD resonators were studied in [42]-[45] and demonstrated good performances.

Because of low propagation and radiation losses, NRD-guide technology is also proven ideal in the design of filters, especially at high frequencies. Rectangular and ring resonators, coupled to the NRD-guide, offer excellent performance as bandpass and bandstop filters. Proper design of the dielectric resonator and a selection of appropriate coupling distance are crucial parameters affecting the filter design in this technology. Various NRD-guide configurations including gap-coupled three, four and five pole NRD

guide, multiple dielectric strips, two-path multimode, round holes drilled through the dielectric, were used to construct the bandpass NRD-guide filters [46]-[50]. NRD-guide bandstop filters were realized with NRD-guide gap coupled to ring resonators and side-coupled guides of rectangular resonators [51]-[53].

The coupling mechanism of a conventional proximity NRD-guide coupler is due to the interaction of exponentially decaying fields between the two NRD-guides. The coupling is a function of the spacing between the two guides. NRD-guide symmetric and nonsymmetrical couplers constructed using two curved NRD-guide sections or a straight and a curved NRD guide section were presented in [54], together with quadrature hybrid couplers and an in-phase power divider at 47-50 GHz. The coupling is improved by filling the gap between the waveguides with a low permittivity dielectric [55]. An NRD-guide leaky-wave type coupler, in which the coupling between the two guides does not primarily depend on the spacing between the guides, was also proposed in [56].

Other components like E-plane double-Y junction circulator [57], power combiners [58], and terminators [59], were also realized in the framework of NRD-guide technology. In Chapter 5, an order-reduced integral equation technique is proposed for the analysis of NRD-guide discontinuities and components.

1.2.4 **Hybrid Planar/NRD-Guide Integrated Circuits**

The NRD-guide has been shown to be a very promising design platform for millimeter-wave integrated circuits owing to its non-radiating and low-loss transmission properties. However, like any other dielectric waveguide, it presents some difficult problems when active device integration is required. For this reason, an architecture called hybrid planar/NRD-guide integration technology was proposed as a building block for constructing both passive and active microwave and millimeter-wave circuits [19]-[22], [60].

In a generalized hybrid planar/NRD-guide structure as shown in Fig. 1.3(a), the microstrip circuits can be relocated on both sides of the parallel metallic plates of the

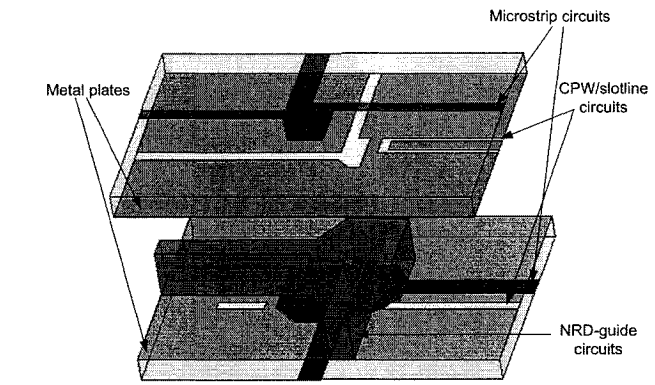

(a)

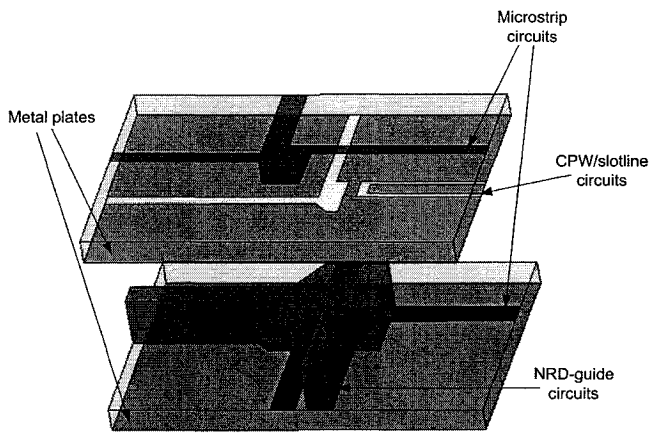

(b)

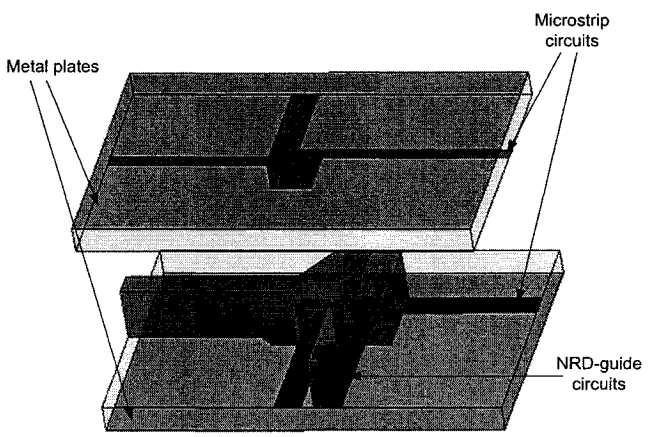

(c)

Fig.1.3. The structures of hybrid planar/NRD-guide integrated circuits.

NRD-guide circuits. In this way, the microstrip circuits share the common ground plane with the NRD-guide circuits that is actually one of the parallel metallic plates. The coupling between the two dissimilar structures is achieved through apertures that are made in the common ground plane. The slotline and coplanar waveguide (CPW) circuits can be constructed on the common ground plates and coupled with microstrip and NRD-guide circuits directly. The three different types of circuits on five layers make the hybrid structures extremely compact. Such a hybrid scheme is particularly suitable for millimeter-wave systems in which active devices can be made with the planar-line technique while passive components can be made with the NRD-guide technique.

Additionally, two alternative hybrid planar/NRD-guide integrated circuits based on the unbalanced and balanced NRD-guide were also proposed in [21], [61]. The unbalanced NRD-guide consists of a core dielectric strip deposited on the top of a relatively thin dielectric substrate and the whole structure is sandwiched between two parallel metallic plates in the same way as required in the standard NRD-guide. In the unbalanced hybrid integrated structure as in Fig. 1.3(b), the microstrip circuits are formed on the relatively thin dielectric substrate and the circuit integration is achieved in a co-layered form. Another thin dielectric substrate can be deposited on the opposite side of the metal plate to form another layer for the design of integrated microstrip circuits. In the balanced NRD-guide, the dielectric strip is sandwiched between two identical relatively thin dielectric substrates with metallization as shown in Fig. 1.3(c). The microstrip circuits that are designed on both thin dielectric substrates can directly be coupled to the NRD-guide on the opposite sides of dielectric strip. These two structures are rather useful if monolithic circuits are required to be integrated with the NRD-guide.

The most important part for the hybrid integration of planar and non-planar structures is related to the design of an integrated transition between the two dissimilar geometries. The transition should feature low-loss broadband. There exit two types of coupling schemes, namely, aperture coupling and co-layer coupling, in the three above hybrid integration techniques. Generally, the aperture-based multilayer technique allows for a greater flexibility of hybrid planar/nonplanar integration and interconnects without

modifying inherent characteristics of the two individual building blocks. The theoretical and experimental results for a microstrip-based aperture coupling integration show that an insertion loss of less than 0.5dB can easily be obtained with 20% bandwidth for a single transition [20]. In a co-layered topology, the planar circuits are in direct physical contact with the NRD-guide, thus yielding a strong electromagnetic coupling between the two dissimilar structures. In the unbalanced case, a potential leakage may exist but it could be suppressed or becomes negligible as compared to conductor loss if an adequate parametric design is made [61], [62].

In practical circuit design, the first type of hybrid-integrated structure as shown in fig. 1.3(a) is more useful than the other two hybrid structures. Many experimental prototypes including transitions, passive components, and active devices based on this hybrid technology have been studied and have shown that this novel hybrid technology is very promising in the design of microwave and millimeter-wave circuits and systems [63]-[69]. In Chapter 6, a generalized surface-volume integral-equation technique is developed for modeling of this type of hybrid integrated circuits.

1.3 Numerical Techniques for NRD Guide Based Millimeter-Wave Circuits

Numerical characterizations and modeling of passive components in microwave and millimeter-wave circuits have been an important research topic and powerful simulation tools are necessary for a reliable and effective design process [70]. In the process of developing NRD-guide based millimeter-wave circuits, a series of numerical methods have been proposed to investigate electric performances and design rules of the structures.

The mode-coupling theory was applied in [34], [35] to analyze loss characteristics of the NRD-guide bends. A rigorous expression for coupling coefficient between LSM_{11} and LSE_{11} modes was derived and then used in the two-mode coupling equations to be solved for the bending loss analysis. A method based on the WKB approximation was used in [38] to predict shifts in field maxima at NRD-guide bends and achieve a proper

width for designing a low loss sharp bend. The coupled mode theory was also used to analyze NRD-guide leaky wave couplers, while potential functions and odd-even mode principle were applied to study NRD-guide directional couplers in [57]. K. Watanabe and K. Yasumoto [71], [72] developed a coupled mode theory using the singular perturbation technique which was shown to yield a better accuracy over the conventional coupled-mode theory, especially in a strong coupling regime of the NRD-guide coupler. The perturbation method was used in [45] to predict the unloaded quality factor of parallelepiped NRD-guide resonators. An efficient design technique of NRD-guide filter based on a variational principle was developed in [46], and both gap-coupled and alternating-width type filters were successfully designed. In the study of a microstrip-coupled NRD-guide resonator in [73], a reciprocity principle together with a modal-field-expansion was employed and scattering parameters were computed using a transmission line analysis of the structure. A small aperture coupling theory, though limited in its applicability by the size of the aperture, was employed in [20] to investigate microstrip-line-to-NRD-guide transitions. The above methods were developed for specific configurations and hard to be extended for generalized NRD-guide based circuits.

Mode-matching method [74] is one of the most frequently used methods for formulating boundary-value problems. In this method, the eigenmodes of each region are found or formulated first and then matched to each other at the junction discontinuity to satisfy the boundary conditions. This method is widely used for modeling dielectric waveguides [30], [75], [76] and was used to design a multiple strip NRD-guide filter in [77]. Furthermore, an iterative optimization process based on the mode-matching method was used in [78] to design a band-pass filter at 28 GHz with 70 dB attenuation in the stop band. A combination of the network approach and the mode matching theory was applied to study of periodic NRD-guide gratings for filter based applications in [79]. The mode-matching technique with a multi-modal transverse resonance condition was applied in [37], [40], [41] to study scattering parameters and characteristics of higher modes generated by several NRD guide components. A method which combines a

staircase approximation with a multimode network theory and a mode-matching procedure was used to systematically investigate leakage characteristics of NRD guide with arbitrary profile of cross section [80], [81]. Another combination of the method of lines along with the mode matching method was deployed to analyze NRD-guide resonators with inhomogeneous dielectric and housing grooves [82]. Nevertheless, the mode-matching method generally fails once the planar section (the top view of dielectric circuits) of the guiding structure is of arbitrary shape and/or has inhomogeneous dielectric permittivity. This method is especially unsuitable for the hybrid planar/NRD-guide integrated circuits.

Techniques based on differential equations, such as finite element method (FEM) [83], finite-difference time domain method (FDTD) [84], and transmission line method (TLM) [85], are the most popular numerical methods for microwave and millimeter-wave circuits. The differential form of Maxwell's equations yields point relations that must be satisfied by the electromagnetic field at every point in space. The first step of a numerical technique based on the differential equations is therefore to divide the configuration and the surrounding space into a number of small pieces or cells.

The FEM is one of the most common frequency domain techniques while the FDTD is a very popular technique for time domain problems. They are often used to construct commercial software such as Ansoft-HFSS and EMPIRE. Obviously, NRD-based circuits can be modeled through such software. A transition using an NRD-guide multi ring resonator as the feedback element was treated in [67] using the TLM algorithm with a field-theoretical model employed to determine resonant frequencies of the resonator. The TLM algorithm has also been employed to design both preliminary and optimized microstrip to NRD-guide transitions in [65], [66]. A rigorous TLM-based modal-extraction approach was developed in [86] to analyze discontinuities in guided-wave structures in general, with particular attention to the NRD-guide.

The main advantage of differential equation based methods is their ability to handle arbitrary, inhomogeneous, and non-linear material. This ability stems from the fact that every point in space needs to be discretized. If the configuration includes

homogeneous regions, or an open region in an even worse case, these methods may require excessive memory and computational time. Open region problems can be treated with absorbing boundary conditions or perfectly matched layers. These boundary conditions may cause computational errors because the real computational region is terminated with these boundaries. Other important issues are numerical dispersion and stability since the field propagates from cell to cell and solutions may diverge.

1.4 Objectives and thesis outline

Integral equation techniques solve for sources of an electromagnetic field rather than the field itself. The starting point is therefore to obtain a source-field relationship in the form of an integro-differential operator in terms of the source. The integral equation is then obtained by enforcing appropriate boundary conditions or using equivalent principles, and a discretization scheme is invoked to solve the equation [87], [88]. The integral equation technique is particularly advantageous for configurations involving homogeneous regions and open regions since only the boundaries need to be discretized. Therefore, integral based techniques are always preferable over differential equation based techniques. Although integral equation techniques are advantageous in computing the open structures, it is still difficult to use them as a general method for modeling complicated structures such as the NRD-guide based circuits as discussed in section 1.2. Until now, no integral equation techniques have been used for the analysis of NRD-guide based millimeter-wave circuits.

The primary objective of this Ph. D. thesis is to develop a set of integral equation techniques for the analysis and modeling of NRD-guide based millimeter-wave circuits systematically. An electric field integral equation method was presented in [89]-[94] for dielectric waveguides with inhomogeneous cross-section in multilayered media. This method will be used to investigate guided-wave properties of the modified NRD-guides with or without leakage loss in this work. However, when this method extends to three dimensions, referred as volume integral-equation method, only a few simple problems

with finite dielectric regions can be solved because of large memory and CPU time requirement [95], [96]. Therefore, an order-reduced volume integral-equation (ORVIE) approach will be proposed in this thesis to model and analyze NRD-guide discontinuities and components as discussed in section 1.2.3. A surface-volume integral-equation approach was developed in [97] for the electrodynamic analysis of structures embedded in multilayered media, which consist of both microstrip/stripline and CPW/slotline comprising three-dimensional (3-D) components like vertical interconnects, finite dielectric fillings, or coatings. In the hybrid planar/NRD-guide integrated structure, the 3-D structure that is concerned with the volume integral-equation is a multi-port NRD-guide circuit of arbitrarily shaped planar section and arbitrarily varied dielectric permittivity in the planar section. The above-mentioned approach is difficult for this hybrid structure not only because of the existence of multi-ports but also because of large memory and CPU time requirement for the complicated dielectric circuit geometry. So a generalized surface-volume integral equation approach will be developed for solutions of the hybrid circuits by extending the ORVIE method to multimode case.

This thesis is organized as follows: Chapter 2 presents the basic theory of integral equation technique. The surface and volume integral equations are formulated for the real and equivalent currents. The dyadic Green's functions in unbounded media and multilayered media are introduced. The framework of method of moments is given and the choice of basis functions is discussed.

Chapter 3 deals with guided wave properties of the standard NRD-guide and H-guide. The field expressions for eigen-modes supported by the NRD-guide and H-guide are presented. The mode spectrum of NRD-guide and H-guide is described based on the characteristic equations. The properties of coupled NRD-guides are discussed.

Chapter 4 addresses the integral equation solution to guided wave properties of the modified NRD-guides. An electric field integral equation method for dielectric waveguides with inhomogeneous cross-section in multilayered media is formulated and the solution to guidance and leakage properties of the modified NRD-guides is discussed. As an important application, a new NRD-guide directional coupler using two

NRD waveguides interconnected with a bridge is proposed and propagation constants of even modes and odd modes of the structure are calculated with the electric field integral equation method. A 3dB directional coupler with optimized parameters is designed on the basis of numerical results. Furthermore, experimental prototypes of both conventional and the proposed coupler are fabricated and measured to verify the advantages of the new couplers as well as the calculated results.

In Chapter 5, an order-reduced volume-integral equation approach is proposed for the analysis of NRD-guide and H-guide millimeter-wave circuits. The volume integral equation is formulated with the spectral dyadic Green's function for the NRD-guide and H-guide circuits. Current discretization only in planar form is realized with the help of mono-vertical mode. A system matrix is obtained with the Garlerkin's method of moments. The solution for the volume-integral equation is reduced to a two-dimensional problem by carrying out the vertical integration in the space domain. The framework of this technique is demonstrated through its application to NRD-guide open-end. In addition, H-guide open-end, three types of resonators, and 3-pole gap-coupled NRD guide filters are modeled and the numerical results are validated with the measured data and results obtained by other methods.

Chapter 6 develops a generalized surface-volume integral equation approach for the analysis of hybrid planar/NRD-guide integrated circuits. Surface-volume integral equations are formulated for the hybrid planar/NRD-guide integrated circuits. The current discretization in planar form for NRD-guide is carried out with each vertical mode and the element matrix is obtained with approximate basis function in planar circuits and NRD-guide circuits. Analytical evaluation in space-domain integration is carried out and a set of first-order Green's functions is obtained. Examples that comprise the microstrip coupled NRD-guide resonator, NRD-guide interconnect between planar circuits, and integrated transition of microstrip-line to NRD-guide structures are case-studied and discussed to demonstrated properties and efficiency of the proposed method.

Finally, Chapter 7 presents the conclusions of the thesis work and recommendations for its related future work. It is noted that some of the work presented in the thesis has been or will be published in [98]-[100].

CHAPTER 2

BASIC THEORY OF INTEGRAL EQUATION TECHNIQUE

Integral equation techniques solve for the sources of an electromagnetic field by obtaining dyadic Green's functions for infinitesimal source terms. The integral equation is obtained by employing an equivalence principle and enforcing appropriate boundary conditions and a discretization scheme of the method of moments (MoM) is involved to solve the equation [87], [88]. In this Chapter, three issues of the integral equation technique, namely, integral equations, dyadic Green's functions, and MoM, will be presented.

2.1 Integral Equations

For a given set of sources, the field may easily be found if the dyadic Green's functions (DGFs) of the environment, which will be discussed in detail in next section,

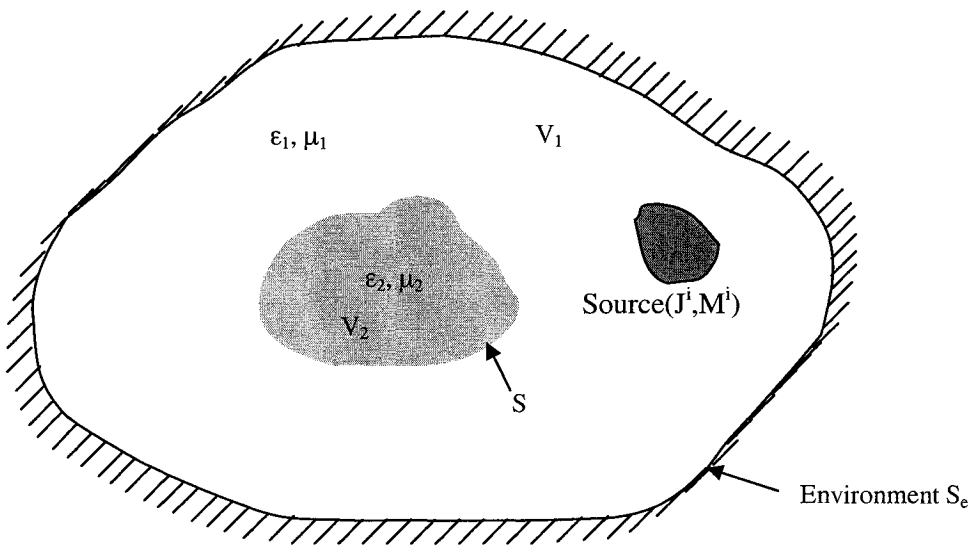

Fig. 2.1. Arbitrarily shaped object V_2 embedded in an homogenous space V_1 which is surrounded by a environment S_e.

are available. When the currents are not known, the Green's functions may be used to formulate integral equations for the real (true) or equivalent currents, which are then solved numerically by the MoM [88]. A standard scattering problem is shown in Fig.2.1 in which an arbitrarily shaped object is embedded in an homogeneous space surrounded by an arbitrary environment. Generally, two classes of integral equations: surface integral equations and volume integral equations, can be formulated for this problem.

2.1.1 Surface Integral Equations

When inhomogeneities are piecewisely constant in each region, we may solve such problems using the surface integral equation technique. This technique is also suitable for non-perfect conductors and perfect electric conductors. In this technique, the homogeneous-medium Green's functions are found for each region. Then, the field in each region is written in terms of the field due to any sources in that region plus the field due to surface sources at interfaces between the regions. Next, the boundary conditions at these interfaces are used to set up integral equations that surface source at the interfaces can be solved for.

Let us consider an arbitrarily shaped object embedded in any environment and excited by known electric and magnetic currents ($\mathbf{J}^i$, $\mathbf{M}^i$), as illustrated in Fig. 2.1. The equations governing the resulting electric and magnetic fields ($\mathbf{E}$, $\mathbf{H}$) are quite easily derived by means of a surface equivalence principle [101]. As an external equivalent problem, the equivalent surface current ($\mathbf{J}_s$, $\mathbf{M}_s$) on S and the impressed currents ($\mathbf{J}^i$, $\mathbf{M}^i$) radiating in V_1 produce the fields ($\mathbf{E}$, $\mathbf{H}$) exterior to S and null fields inside S.

$$\mathbf{E}_s(\mathbf{r}) = \iint_S d\mathbf{r}' \bar{\mathbf{G}}_1^{EJ}(\mathbf{r},\mathbf{r}') \cdot \mathbf{J}_s(\mathbf{r}') + \iint_S d\mathbf{r}' \bar{\mathbf{G}}_1^{EM}(\mathbf{r},\mathbf{r}') \cdot \mathbf{M}_s(\mathbf{r}') \tag{2.1}$$

$$\mathbf{H}_s(\mathbf{r}) = \iint_S d\mathbf{r}' \bar{\mathbf{G}}_1^{HJ}(\mathbf{r},\mathbf{r}') \cdot \mathbf{J}_s(\mathbf{r}') + \iint_S d\mathbf{r}' \bar{\mathbf{G}}_1^{HM}(\mathbf{r},\mathbf{r}') \cdot \mathbf{M}_s(\mathbf{r}') \tag{2.2}$$

$$\mathbf{E}^i(\mathbf{r}) = \left\langle \bar{\mathbf{G}}_1^{EJ}(\mathbf{r},\mathbf{r}'); \mathbf{J}^i(\mathbf{r}') \right\rangle + \left\langle \bar{\mathbf{G}}_1^{EM}(\mathbf{r},\mathbf{r}'); \mathbf{M}^i(\mathbf{r}') \right\rangle \tag{2.3}$$

$$\mathbf{H}^i(\mathbf{r}) = \left\langle \bar{\mathbf{G}}_1^{HJ}(\mathbf{r},\mathbf{r}'); \mathbf{J}^i(\mathbf{r}') \right\rangle + \left\langle \bar{\mathbf{G}}_1^{HM}(\mathbf{r},\mathbf{r}'); \mathbf{M}^i(\mathbf{r}') \right\rangle \tag{2.4}$$

Clearly, $(\mathbf{E}, \mathbf{H})=(\mathbf{E}^i+\mathbf{E}_s, \mathbf{H}^i+\mathbf{H}_s)$, where $(\mathbf{E}^i, \mathbf{H}^i)$ are the impressed fields due to $(\mathbf{J}^i, \mathbf{M}^i)$ and $(\mathbf{E}_s, \mathbf{H}_s)$ are the scattered fields due to $(\mathbf{J}_s, \mathbf{M}_s)$. $\bar{\mathbf{G}}_1^{PQ}(\mathbf{r},\mathbf{r}')$ is the DGF relating to P-type fields at $\mathbf{r}$ and Q-type currents at $\mathbf{r}'$ in the absence of scatter V_2. The notation $\langle,\rangle$ is used for integrals of products of two functions separated by the comma over their common spatial support, with a dot over the comma indicating a dot product. The integral can be either a surface integral or a volume integral depending on the type of impressed currents. If the DGFs of the environment are available, one can use (2.3) and (2.4) to compute the impressed fields and to express the scattered fields in (2.1) and (2.2) in terms of the unknown currents $(\mathbf{J}_s, \mathbf{M}_s)$.

The boundary conditions at S^+ dictate that

$$\mathbf{M}_s^+ = -\hat{\mathbf{n}}\times\left(\mathbf{E}^i+\mathbf{E}^s\left[\mathbf{J}_s,\mathbf{M}_s\right]\right)_{S^+} \tag{2.5}$$

$$\mathbf{J}_s^+ = \hat{\mathbf{n}}\times\left(\mathbf{H}^i+\mathbf{H}^s\left[\mathbf{J}_s,\mathbf{M}_s\right]\right)_{S^+} \tag{2.6}$$

where $\hat{\mathbf{n}}$ is the outward unit vector normal to S and the subscript S^+ indicates that the fields are evaluated as the observation point approaches S from the exterior region.

For penetrable objects, an interior equivalent problem may be constructed, in which the surface currents $(-\mathbf{J}_s, -\mathbf{M}_s)$, radiating in the presence of the object, produce the correct fields $(\mathbf{E}, \mathbf{H})$ inside S and null fields outside. If the object is homogenous, its medium may be extended to fill the entire space surrounded by S_e and the field is computed as:

$$\mathbf{E}_s(\mathbf{r}) = -\iint_S d\mathbf{r}'\bar{\mathbf{G}}_2^{EJ}(\mathbf{r},\mathbf{r}')\cdot\mathbf{J}_s(\mathbf{r}') - \iint_S d\mathbf{r}'\bar{\mathbf{G}}_2^{EM}(\mathbf{r},\mathbf{r}')\cdot\mathbf{M}_s(\mathbf{r}') \tag{2.7}$$

$$\mathbf{H}_s(\mathbf{r}) = -\iint_S d\mathbf{r}'\bar{\mathbf{G}}_2^{HJ}(\mathbf{r},\mathbf{r}')\cdot\mathbf{J}_s(\mathbf{r}') - \iint_S d\mathbf{r}'\bar{\mathbf{G}}_2^{HM}(\mathbf{r},\mathbf{r}')\cdot\mathbf{M}_s(\mathbf{r}') \tag{2.8}$$

Similarly, $(\mathbf{E}, \mathbf{H})=(\mathbf{E}_s, \mathbf{H}_s)$. $\bar{\mathbf{G}}_2^{PQ}(\mathbf{r},\mathbf{r}')$ is the DGF relating to P-type fields at $\mathbf{r}$ and Q-type currents at in the absence of scatter V_1.

The boundary conditions at S^- dictate that

$$\mathbf{M}_s^- = -\hat{\mathbf{n}}\times\left(\mathbf{E}^s\left[-\mathbf{J}_s,-\mathbf{M}_s\right]\right)_{S^-} \tag{2.9}$$

$$\mathbf{J}_s^- = \hat{\mathbf{n}} \times \left(\mathbf{H}^s \left[-\mathbf{J}_s, -\mathbf{M}_s \right] \right)_{S^-} \tag{2.10}$$

where the subscript S^- indicates that the fields are evaluated as the observation point approaches S from the interior region.

Combining them with those of the exterior problem yields a coupled set of uniquely solvable for ($\mathbf{J}_s$, $\mathbf{M}_s$) [102].

$$\mathbf{M}_s(\mathbf{r})^+ = \mathbf{M}_s(\mathbf{r})^- \tag{2.11}$$

$$\mathbf{J}_s(\mathbf{r})^+ = \mathbf{J}_s(\mathbf{r})^- \tag{2.12}$$

Non-perfect conductors can often be modeled as surface impedance objects characterized by the impedance boundary condition (IBC) $\mathbf{M}_s = Z_s \mathbf{J}_s \times \hat{\mathbf{n}}$ where Z_s is the skin effect surface impedance [103], [104]. One can use this IBC in either (2.5) or (2.6) to eliminate $\mathbf{M}_s$.

$$\mathbf{n} \times \left(\mathbf{E}^i + \mathbf{E}^s \left(\mathbf{J}_s, Z_s \mathbf{J}_s \times \hat{\mathbf{n}} \right) \right) - Z_s(\mathbf{r}) \mathbf{J}_s(\mathbf{r}) = 0 \tag{2.13}$$

$$\mathbf{n} \times \left(\mathbf{H}^i + \mathbf{H}^s \left(\mathbf{J}_s, Z_s \mathbf{J}_s \times \hat{\mathbf{n}} \right) \right) - \mathbf{J}_s = 0 \tag{2.14}$$

The resulting equations are referred to, respectively, as the electric-field integral equation (EFIE) and the magnetic-filed integral equation (MFIE).

By setting Z_s equals zero, the integral equations for perfect electric conductor (PEC) can be obtained:

$$\mathbf{n} \times \mathbf{E}(\mathbf{r}) = \mathbf{n} \times \left(\mathbf{E}^i(\mathbf{r}) + \mathbf{E}^s(\mathbf{J}_s) \right) = 0, \qquad \mathbf{r} \in S \tag{2.15}$$

$$\mathbf{n} \times \mathbf{H}(\mathbf{r}) = \mathbf{n} \times \left(\mathbf{H}^i(\mathbf{r}) + \mathbf{H}^s(\mathbf{J}_s) \right) = \mathbf{J}_s(\mathbf{r}), \qquad \mathbf{r} \in S \tag{2.16}$$

Only the EFIE is applicable to open, infinitesimally thin shells made of a PEC. In the analysis of microstrip structures, it is common to use a simplified form of the EFIE, which neglects the contribution of $\mathbf{M}_s$ to $\mathbf{E}_s$ as [105].

$$\mathbf{n} \times \left(\mathbf{E}^i + \mathbf{E}^s(\mathbf{J}_s) \right) - Z_s(\mathbf{r}) \mathbf{J}_s = 0 \tag{2.17}$$

There are important applications where the object in Fig. 2.1 is excited through an aperture in a PEC plane. In such cases the aperture is "shorted" and an equivalent magnetic surface current is placed over the shorted region to support the correct electric

field there. The contribution of this current is then included in (2.5) and (2.6). Since the equivalent aperture current is typically unknown, the MPIE's are supplemented by an integral equation obtained by enforcing the continuity of the tangential magnetic filed across the aperture [106].

The EFIE in (2.15) can be written in a shorter notation as

$$\Im \mathbf{J}_s = \mathbf{n} \times \mathbf{E}^i \tag{2.18}$$

Where $\Im$ is a linear operator. Integral equations in the form of (2.18) are referred to as Fredholm integral equations of the first kind since the unknown quantity only appears inside the integral [107].

The MFIE may be written in a shorter notation

$$\left(\frac{1}{2} \bar{\mathrm{I}} + \Re \right) \mathbf{J}_s = \mathbf{n} \times \mathbf{H}^i \tag{2.19}$$

where $\bar{\mathrm{I}}$ is the identity operator and $\Re$ is a compact operator. Integral equations that can be written as in (2.19) are known as Fredholm integral equations of the second kind and are much more amenable for a stable numerical solution than integral equations of the first kind [108].

When applied to a closed object the EFIE and MFIE fail to provide a unique solution for all frequencies. The non-uniqueness is caused by homogeneous solutions, i.e., solutions that fulfill the boundary conditions with zero incident fields. The homogeneous solutions also are known as spurious solutions. The most common way to avoid homogeneous solutions is by solving the combined field integral equation (CFIE) [109]. The CFIE is obtained as a linear combination of the EFIE and MFIE which in operator form leads to

$$\alpha \Im \mathbf{J}_s + (1+\alpha)\eta \left(\frac{1}{2} \bar{\mathrm{I}} + \Re \right) \mathbf{J}_s = \alpha \mathbf{n} \times \mathbf{E}^i + (1-\alpha)\eta \mathbf{n} \times \mathbf{H}^i \tag{2.20}$$

where α is a real number between 0 and 1 and $\eta = \sqrt{\mu / \varepsilon}$ is the intrinsic impedance. Usually, $0.2<\alpha<0.8$ is a good choice.

2.1.2 Volume Integral Equations

When the arbitrarily shaped object in Fig. 2.1 is inhomogeneous, an alternative method is to view the scattered field as due to the induced currents flowing in the inhomogeneity. The induced currents are proportional to the total field in the inhomogeneity, and, in turn, the total field is the incident field plus the field due to induced currents in the inhomogeneity. So, this concept yields an equation called the volume integral equation from which the unknown field inside the inhomogeneity can be solved for.

We shall show how the corresponding volume integral equation can be derived for a finite size, inhomogeneous scatter for the electromagnetic wave case as shown in Figure 2.1. First, from Maxwell's equations, it follows that the electric field everywhere satisfies the following equation:

$$\mu_2 \nabla \times \mu_2^{-1} \nabla \times \mathbf{E}(\mathbf{r}) - k_2^2(\mathbf{r})\mathbf{E}(\mathbf{r}) = i\omega\mu_2 \mathbf{J}^i(\mathbf{r}) \tag{2.21}$$

Where μ_2, ε_2, and $k_2^2 = \omega^2 \mu_2 \varepsilon_2$ are functions of position inside the inhomogeneous region V_2. Next, using the vector identity that $\nabla \times \psi \mathbf{A} = \nabla\psi \times \mathbf{A} + \psi \nabla \times A$, the above can be rewritten as

$$\nabla \times \nabla \times \mathbf{E}(\mathbf{r}) + \left(\mu_2 \nabla \mu_2^{-1}\right) \times \nabla \times \mathbf{E}(\mathbf{r}) - k_2^2 \mathbf{E}(\mathbf{r}) = i\omega\mu_2 \mathbf{J}^i(\mathbf{r}) \tag{2.22}$$

We can rewrite (2.22) as

$$\nabla \times \nabla \times \mathbf{E}(\mathbf{r}) - k_1^2 \mathbf{E}(\mathbf{r}) = i\omega\mu_2 \mathbf{J}^i(\mathbf{r}) + \left[k_2^2(r) - k_1^2\right]\mathbf{E}(\mathbf{r}) - \left(\mu_2 \nabla \mu_2^{-1}\right) \times \nabla \times \mathbf{E}(\mathbf{r}) \tag{2.23}$$

Physically, the terms on the right-hand side of equation (2.23) are effective current sources. Therefore, the solution to (2.23) is

$$\begin{aligned} \mathbf{E}(\mathbf{r}) = i\omega\mu_2 \int_V d\mathbf{r}' \bar{\mathbf{G}}_1^{EJ}(\mathbf{r},\mathbf{r}') \cdot \mathbf{J}^i(\mathbf{r}') + \int_V d\mathbf{r}' \bar{\mathbf{G}}_1^{EJ}(\mathbf{r},\mathbf{r}') \cdot \left[k_2^2(\mathbf{r}') - k_1^2\right]\mathbf{E}(\mathbf{r}') \\ - \int_V d\mathbf{r}' \bar{\mathbf{G}}_1^{EJ}(\mathbf{r},\mathbf{r}') \cdot \left(\mu_2 \nabla \mu_2^{-1}\right) \times \nabla \times \mathbf{E}(\mathbf{r}') \end{aligned} \tag{2.24}$$

In the above, the first term is just the incident field. $\bar{\mathbf{G}}_1^{EJ}(\mathbf{r},\mathbf{r}')$ is the DGF in the absence of the scatter. Hence, (2.24) becomes

$$\mathbf{E}(\mathbf{r})=\mathbf{E}^{i}(\mathbf{r})+\int_{V} d\mathbf{r}'\bar{\mathbf{G}}_1^{EJ}(\mathbf{r},\mathbf{r}')\cdot\left[k_2^2(\mathbf{r}')-k_1^2\right]\mathbf{E}(\mathbf{r}') \\ -\int_{V} d\mathbf{r}'\bar{\mathbf{G}}_1^{EJ}(\mathbf{r},\mathbf{r}')\cdot\left(\mu_2\nabla\mu_2^{-1}\right)\times\left[\nabla\times\mathbf{E}(\mathbf{r}')\right] \tag{2.25}$$

The integrals in (2.25) are contributions to the field **E** from the volume current induced in the scatter by the total electric field **E** and magnetic field **H** (note that $\nabla\times\mathbf{E}=i\omega\mu\mathbf{H}$). Hence, the first term is generated by the electric polarization current or displacement current, while the second term is generated by the magnetic polarization charges. Moreover, when the scatter is conductive such that $\varepsilon=\varepsilon'+i\sigma/\omega$, the first integral in (2.25) is due to the conduction current induced by the field as well. This is obviated by substituting the complex permittivity into (2.25) and identifying a term proportional to $\sigma\mathbf{E}$ corresponding to conduction currents. On the other hand, if μ is assumed constant, equation (2.25) is simplified to

$$\mathbf{E}(\mathbf{r})=\mathbf{E}^{i}(\mathbf{r})+\int_{V} d\mathbf{r}'\bar{\mathbf{G}}_1^{EJ}(\mathbf{r},\mathbf{r}')\cdot O(\mathbf{r}')\mathbf{E}(\mathbf{r}') \tag{2.26}$$

where $O(\mathbf{r}')=k_2^2(\mathbf{r}')-k_1^2$.

Obviously, equations (2.25) and (2.26) are Fredholm integral equations of the second kind because the unknown is both inside and outside the integral.

2.2 Dyadic Green's Functions

The Green's function of a wave equation is the solution of the wave equation for a point source. A DGF is a dyad that relates a vector field to a vector current source. The scalar Green's function in V_1 in Fig. 2.1 is the solution to the following scalar wave equation:

$$\left(\nabla^2+k^2\right)g(\mathbf{r},\mathbf{r}')=-\delta(\mathbf{r}-\mathbf{r}'). \tag{2.27}$$

Similarly, the DGF in V_1 is the solution to the following vector wave equation:

$$\nabla\times\nabla\times\bar{\mathbf{G}}_e(\mathbf{r},\mathbf{r}')-k^2\bar{\mathbf{G}}_e(\mathbf{r},\mathbf{r}')=\bar{\mathbf{I}}\delta(\mathbf{r}-\mathbf{r}'), \tag{2.28}$$

When the solution to the wave equation due to a point source is known, the solution due to a general source can be obtained by the principle of linear superposition. This is merely a result of the linearity of the wave equation, and that a general source is just a linear superposition of point sources.

The use of DGFs makes the formulations and the solutions of some electromagnetic problems more compact. Even though most problems can be solved without using DGFs, the symbolic simplicity they offer makes their use attractive. Only in a few simple geometries the DGFs can be solved in closed form. In many instances, the DGFs are obtained in terms of the vector wave functions of the geometry considered.

2.2.1 DGF in a Homogeneous Medium

The spatial representation of the DGF in a homogeneous, isotropic medium (ε, μ) can be represented in terms of simple algebraic functions which are the derivatives of the scalar Green's function as follows,

$$\bar{\mathbf{G}}(\mathbf{r},\mathbf{r}') = \left[\bar{\mathbf{I}} + \frac{\nabla\nabla}{k_0^2}\right] g(\mathbf{r},\mathbf{r}') \tag{2.29}$$

where $k_0 = \omega\sqrt{\mu\varepsilon}$ and $g(\mathbf{r},\mathbf{r}')$ is the scalar Green's function in a homogeneous, isotropic medium as

$$g(\mathbf{r},\mathbf{r}') = \frac{e^{ik_0|\mathbf{r}-\mathbf{r}'|}}{4\pi|\mathbf{r}-\mathbf{r}'|}, \tag{2.30}$$

But if **r**, the point where the field **E**(**r**) is observed, is in the source region V, $|\mathbf{r}-\mathbf{r}'|$ could be zero. When $|\mathbf{r}-\mathbf{r}'| \to 0$, $g(\mathbf{r},\mathbf{r}')$ becomes singular, and the term $\nabla\nabla$, operating on $g(\mathbf{r},\mathbf{r}')$, gives rise to terms $O\left(1/|\mathbf{r}-\mathbf{r}'|^3\right)$. Hence, the resultant integral is non-uniformly convergent.

The singularity can be removed by the principal volume method as

$$\mathbf{E}(\mathbf{r}) = i\omega\mu P.V.\int_V d\mathbf{r}'\bar{\mathbf{G}}(\mathbf{r},\mathbf{r}')\cdot\mathbf{J}(\mathbf{r}') + \frac{\bar{\mathbf{L}}\cdot\mathbf{J}(\mathbf{r})}{i\omega\varepsilon}, \tag{2.31}$$

When r ∈ V, where

$$P.V.\int_V = \lim_{V_\delta \to 0} \int_{V-V_\delta}$$

stands for a shape dependent principal value integral and $\bar{\mathbf{L}}$ is a dyad dependent on the shape of V_δ [110]. As a consequence, a symbolic way to write the DGF which is valid for all observation points is

$$\bar{\mathbf{G}}(\mathbf{r},\mathbf{r}') = P.V.\bar{\mathbf{G}}(\mathbf{r},\mathbf{r}') - \frac{\bar{\mathbf{L}}\delta(\mathbf{r}-\mathbf{r}')}{k_0^2} \tag{2.32}$$

The DGF in its spectral representation can also be derived by first Fourier transformation equation (2.28) in the variable and giving

$$-\mathbf{k}\times\mathbf{k}\times\tilde{\bar{\mathbf{G}}}(\mathbf{k},\mathbf{r}') - k_0^2\tilde{\bar{\mathbf{G}}}(\mathbf{k},\mathbf{r}') = \bar{\mathbf{I}}e^{-i\mathbf{k}\cdot\mathbf{r}'} \tag{2.33}$$

where $\mathbf{k} = \hat{x}k_x + \hat{y}k_y + \hat{z}k_z$. The above can be inverted to yield

$$\tilde{\bar{\mathbf{G}}}(\mathbf{k},\mathbf{r}') = \frac{\bar{\mathbf{I}}k_0^2 - \mathbf{kk}}{k_0^2\left(k^2 - k_0^2\right)}e^{-i\mathbf{k}\cdot\mathbf{r}'} \tag{2.34}$$

where $k^2 = k_x^2 + k_y^2 + k_z^2$. Equation (2.34) can be shown to be a solution of (2.33) by back-substituting (2.34) into (2.33). Consequently, we can write

$$\bar{\mathbf{G}}(\mathbf{r},\mathbf{r}') = \frac{1}{(2\pi)^2}\int\int\int_{-\infty}^{\infty} d\mathbf{k}e^{i\mathbf{k}\cdot(\mathbf{r}-\mathbf{r}')}\frac{\bar{\mathbf{I}}k_0^2 - \mathbf{kk}}{k_0^2\left(k^2 - k_0^2\right)} \tag{2.35}$$

where $d\mathbf{k} = dk_x dk_y dk_z$.

The above Fourier representation of $\bar{\mathbf{G}}(\mathbf{r},\mathbf{r}')$ is a non-convergent integral in the classical sense because the magnitude of the integrand tends to a constant when $|\mathbf{k}| \to \infty$. This Fourier representation, however, includes generalized functions or distributions such as the Dirac delta function. By extracting the delta function singularity from Equation (2.29), we come up with

$$\bar{\mathbf{G}}(\mathbf{r},\mathbf{r}') = \frac{i}{8\pi^2}\int_{-\infty}^{\infty}\int d\mathbf{k}_s e^{i\mathbf{k}_s\cdot(\mathbf{r}_s-\mathbf{r}_s')+ik_{0z}|z-z'|}\frac{\bar{\mathbf{I}}k_0^2-\mathbf{k}_0\mathbf{k}_0}{k_0^2 k_{0z}} - \frac{\hat{\mathbf{z}}\hat{\mathbf{z}}}{k_0^2}\delta(\mathbf{r}-\mathbf{r}') \tag{2.36}$$

where $k_s = \hat{x}k_x + \hat{y}k_y$, $d\mathbf{k}_s = dk_x dk_y$, $k_{0z} = \sqrt{k_0^2 - k_x^2 - k_y^2}$, $r_s = \hat{x}x + \hat{y}y$, and

$$\mathbf{k}_0 = \begin{cases} \hat{x}k_x + \hat{y}k_y + \hat{z}k_z, & z\text{-}z'>0, \\ \hat{x}k_x + \hat{y}k_y - \hat{z}k_z & z\text{-}z'<0. \end{cases}$$

2.2.2 DGFs for Multilayered Media

In a variety of applications, such as geophysical prospecting, remote sensing, wave propagation, and microstrip circuits and antennas, it is necessary to compute the electromagnetic field in a layered medium. The DGFs of the multilayered media will be used in this thesis. Here we will give the main formulations for the DGFs and the detailed derivation of these formulations is given in Appendix A or in reference [111].

In a planar multilayered media as in Fig. 2.2, the solution of Maxwell's equations is sought by decomposing the electromagnetic waves into TE and TM types. More specifically, for the TE waves, the electric field is transverse to the z direction, while for the TM waves, the magnetic field is transverse to the z direction. By introducing the Fourier transform formalism, the spectral fields can be expressed in terms of voltages and currents on the transmission-line analog of the medium.

$$\tilde{\mathbf{E}} = \hat{\mathbf{u}}V^e + \hat{\mathbf{v}}V^h - \hat{\mathbf{z}}\frac{1}{j\omega\varepsilon}\left(jk_\rho I^e + \tilde{J}_z\right) \tag{2.37}$$

$$\tilde{\mathbf{H}} = -\hat{\mathbf{u}}I^h + \hat{\mathbf{v}}I^e + \hat{\mathbf{z}}\frac{1}{j\omega\mu}\left(jk_\rho V^h - \tilde{M}_z\right) \tag{2.38}$$

which indicates that outside the source region (V^e, I^e) and (V^h, I^h) represent fields that are, respectively, TM and TE to z. $\tilde{J}_z$, $\tilde{M}_z$ are the z-component of electric and magnetic current sources in spectral space respectively. The unit vectors $(\hat{\mathbf{u}}, \hat{\mathbf{v}})$ are given by

$$\hat{\mathbf{u}} = \frac{k_x}{k_\rho}\hat{\mathbf{x}} + \frac{k_y}{k_\rho}\hat{\mathbf{y}}, \qquad \hat{\mathbf{v}} = -\frac{k_y}{k_\rho}\hat{\mathbf{x}} + \frac{k_x}{k_\rho}\hat{\mathbf{y}} \tag{2.39}$$

where $k_\rho = \sqrt{k_x^2 + k_y^2}$. The space-domain fields (**E**, **H**) are obtained from (2.37) and (2.38) via the inverse Fourier transform.

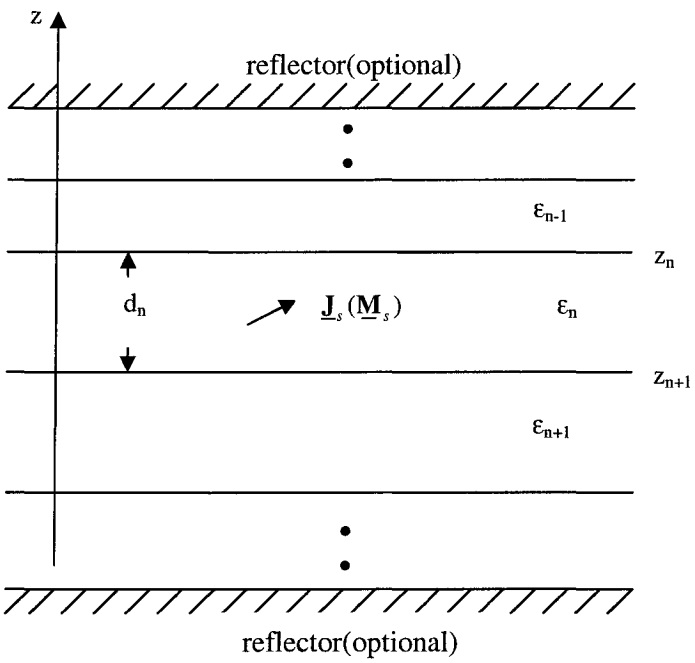

Fig. 2.2. A point source embedded in a multilayered planar structure.

The DGFs for a medium with an unspecified stratification are formulated in terms of the transmission-line Green's functions (TLGFs).

$$\begin{aligned}\bar{\bar{\mathbf{G}}}^{EJ} = &-\hat{\mathbf{u}}\hat{\mathbf{u}}V_i^e - \hat{\mathbf{v}}\hat{\mathbf{v}}V_i^h + \hat{\mathbf{z}}\hat{\mathbf{u}}\frac{k_\rho}{\omega\varepsilon}I_i^e + \hat{\mathbf{u}}\hat{\mathbf{z}}\frac{k_\rho}{\omega\varepsilon}V_v^e \\ &+ \hat{\mathbf{z}}\hat{\mathbf{z}}\frac{1}{j\omega\varepsilon}\left[\frac{k_\rho^2}{j\omega\varepsilon}I_v^e - \delta(z-z')\right]\end{aligned} \tag{2.40}$$

Other types of DGFs as $\bar{\bar{\mathbf{G}}}^{HJ}$, $\bar{\bar{\mathbf{G}}}^{EM}$, and $\bar{\bar{\mathbf{G}}}^{HM}$ have a similar expression and are shown in Appendix A. The space-domain DGFs follow from (2.40) upon first projecting the unit vectors $(\hat{\mathbf{u}}, \hat{\mathbf{v}})$ on the (k_x, k_y)-coordinate system via (2.39) and then applying the inverse Fourier transformation.

At last, the formulation for multilayered media with piecewise-constant parameters can be obtained by introducing a cascaded connection of uniform transmission line sections. Consider the case m=n, when z is within the source section. The TLGF V_i^p is then readily determined as

$$V_i^p(z|z') = \frac{Z_n^p}{2}\left[e^{-jk_{zn}^p|z-z'|} + \frac{1}{D_n^p}\sum_{s=1}^{4} R_{ns}^p e^{-jk_{zn}^p \gamma_{ns}} \right] \tag{2.41}$$

where

$$D_n^p = 1 - \Gamma_{\cup n}^p \Gamma_{\cap n}^p t_n^p \tag{2.42}$$

$$R_{n1}^p = \Gamma_{\cap n}^p, \qquad R_{n2}^p = \Gamma_{\cup n}^p, \qquad R_{n3}^p = R_{n4}^p = \Gamma_{\cup n}^p \Gamma_{\cap n}^p \tag{2.43}$$

$$\gamma_{n1} = 2z_{n+1} - (z+z'), \qquad \gamma_{n2} = (z+z') - 2z_n$$

$$\gamma_{n3} = 2d_n + (z-z'), \qquad \gamma_{n4} = 2d_n - (z-z') \tag{2.44}$$

$\Gamma_{\cup n}^p$ and $\Gamma_{\cap n}^p$ are the voltage reflection coefficients looking to the up and down sides, respectively, out of the terminals of section n. These coefficients may be computed from the relations

$$\Gamma_{\cup n+1}^p = \frac{\Gamma_{n,n+1}^p + \Gamma_{\cup n}^p t_n^p}{1 + \Gamma_{n,n+1}^p \Gamma_{\cup n}^p t_n^p}, \qquad \Gamma_{\cap n-1}^p = \frac{\Gamma_{n,n-1}^p + \Gamma_{\cap n}^p t_n^p}{1 + \Gamma_{n,n-1}^p \Gamma_{\cap n}^p t_n^p} \tag{2.45}$$

where

$$\Gamma_{ij}^p = \frac{Z_i^p - Z_j^p}{Z_i^p + Z_j^p} \tag{2.46}$$

and $t_n^p = e^{-j2k_{zn}^p d_n}$ with $d_n = z_{n+1} - z_n$.

The remaining TLGFs, $V_v^p(z|z')$, $I_v^p(z|z')$ and $I_i^p(z|z')$, may already be derived from (2.41) upon using the solutions of the transmission line equations and the reciprocity properties. The m≠n case is given in the appendix. A.

2.3 The Method of Moments

The integral equations in section 2.1 in general do not have closed-form solutions and the unknowns have to be solved numerically. The MoM, which becomes popular in the electromagnetic community through the work of Harrington [88], is among the most widely used numerical techniques in electromagnetics and is selected in this thesis.

2.3.1 Solutions by the MoM

Most solutions of functional equations can be interpreted in terms of projections onto subspaces of functional spaces. For computation, these subspaces must necessarily be finite dimensional. For theoretical work, they may be infinite dimensional.

Consider the deterministic equation

$$\Re \mathbf{f} = \mathbf{g} \tag{2.47}$$

where $\Re$ is a linear operator, $\mathbf{g}$ is a known function, and $\mathbf{f}$ is the unknown function to be determined. Typical examples of such equations are the EFIE and MFIE in (2.18) and (2.19), respectively. The first step in the MoM is to approximate the unknown function $\mathbf{f}$ by a linear combination of known functions $\mathbf{B}_n$, n=1,2,....,N in the domain of $\Re$. The approximation is

$$\mathbf{f} \approx \mathbf{f}^N = \sum_{n=1}^{N} I_n \mathbf{B}_n \tag{2.48}$$

where scalars I_n are unknown coefficients to be determined. The functions $\mathbf{B}_n$ are called basis functions or expansion functions and their form will be discussed later. In practical problems it is always required to use a finite N such that $\mathbf{f}$ is approximated in the finite-dimensional subspace spanned by the basis functions. The residual is defined as

$$\mathbf{r}^N = \mathbf{g} - \Re \mathbf{f}^N = \mathbf{g} - \sum_{n=1}^{N} I_n \Re \mathbf{B}_n \tag{2.49}$$

where the linearity of the operator was used. The residual is forced to be orthogonal to another N-dimensional subspace spanned by a set of functions $\mathbf{T}_m$, m=1,2,....,N. This condition is expressed as

$$\left\langle \mathbf{T}_m, \mathbf{r}^N \right\rangle = 0, \qquad m = 1, 2, ..., N, \tag{2.50}$$

where $\langle \cdot, \cdot \rangle$ is the inner product. The functions $\mathbf{T}_m$ are known as testing or weighting functions. The MoM is sometimes referred to as the method of weighted residuals which is clear from the expression above. Inserting (2.49) in (2.50) leads to the matrix equation

$$\bar{\mathbf{Z}}\mathbf{I} = \mathbf{V} \tag{2.51}$$

where $\bar{\mathbf{Z}}$ and $\mathbf{V}$ have the elements

$$Z_{mn} = \langle \mathbf{T}_m, \Re \mathbf{B}_n \rangle, \tag{2.52a}$$

$$V_m = \langle \mathbf{T}_m, \mathbf{g} \rangle. \tag{2.52b}$$

The elements I_n of I are the desired coefficients in (2.48). The matrix $\bar{\mathbf{Z}}$ is often referred to as the MoM matrix of the impedance matrix and $\mathbf{V}$ is referred to as the excitation vector.

The name "method of moments" derives from the original terminology that $\int x^n f(x) dx$ is the nth moment of f. When x^n is replaced by an arbitrary $\mathbf{T}_n$, we continue to call the integral a moment of f.

The MoM is also called method of projection since it projects an unknown function onto the N-dimensional subspace spanned by the basis functions. The coefficients in the projection are chosen to ensure that the residual is orthogonal to the N-dimensional subspace spanned by the testing functions. For a general $\Re$ it is not possible to say anything about the convergence of $\mathbf{f}^N$ to $\mathbf{f}$ [112]. In fact, the MoM does not guarantee that the coefficients I_n are optimal. If the testing functions are poorly chosen the residual might have large components outside the space spanned by the testing functions. In general, this is avoided if the testing functions can accurately represent both $\mathbf{g}$ and $\Re \mathbf{f}^N$. This requires that $\mathbf{T}_m$ is in the range of $\Re$ [113].

The simplest specialization for computation is the point matching or collocation method. By choosing the testing functions to be Dirac delta functions, the integrations represented by the inner products now become trivial, which is the major advantage of this method. The solution is sometimes sensitive to the points at which the equation is

matched, which is the major disadvantage of the method. However, if a judicious choice of points of match is taken, the method often gives answers of good accuracy.

Another possibility is that of minimizing the length or norm of the residual as

$$\begin{aligned}\left\|\mathbf{r}^N\right\|^2 &= \left\langle \mathbf{g}-\sum I_m \Re\mathbf{B}_m, \mathbf{g}-\sum I_n \Re\mathbf{B}_n \right\rangle \\ &= \left\langle \mathbf{g},\mathbf{g}\right\rangle - 2\sum I_m \left\langle \Re\mathbf{B}_m, \mathbf{g}\right\rangle + \sum\sum I_m I_n \left\langle \Re\mathbf{B}_m, \Re\mathbf{B}_n \right\rangle\end{aligned} \tag{2.53}$$

The minimum is obtained by setting the derivatives of $\left\|\mathbf{r}^N\right\|^2$ with respect to each I_k equal to zero. This gives

$$\frac{\partial\left\|\mathbf{r}^N\right\|^2}{\partial I_k} = 0 = -2\left\langle \Re\mathbf{B}_k, \mathbf{g}\right\rangle + 2\sum I_n \left\langle \Re\mathbf{B}_k, \Re\mathbf{B}_n \right\rangle \tag{2.54}$$

K=1,2,3,... These equations are identical to (2.51) if

$$\mathbf{T}_m = \Re\mathbf{B}_m \tag{2.55}$$

This condition ensures that the testing functions belong to the range of the operator. This is desirable since $\mathbf{r}^N$ also belongs to the range of the operator and $\mathbf{T}_m$ must be a good approximation of $\mathbf{r}^N$. This special case of MoM is known as the method of least squares. However, the testing functions in (2.55) are not practical.

The EFIE and MFIE operators presented in sections 2.1 have the same domain and range. In other words, if $\mathbf{B}_m$ is a good basis for the domain of $\Re$ it is also a good basis for the range of $\Re$. This suggests that the choice

$$\mathbf{T}_m = \mathbf{B}_m \tag{2.56}$$

might be as good as (2.55) since both conditions ensure that $\mathbf{T}_m$ is in the range of $\Re$. The condition of orthogonality in (2.50) then becomes

$$\left\langle \mathbf{B}_m, \mathbf{r}^N \right\rangle = 0, \qquad m = 1,2,...,N \tag{2.57}$$

This special case of MoM is known as Galerkin's method or MoM with Galerkin testing and it results in so-called super-convergence for scattering computations [114].

2.3.2 Choices of Basis Functions

Basis functions can be categorized as entire-domain or subsectional. Entire-domain basis functions are defined on the entire computational domain. Subsectional basis functions are defined on a subdomain of the object and for surfaces the subdomains are usually taken as triangles or quadrilaterals. Well-known examples of such subsectional basis functions are the RWG functions for triangles [115] and the rooftop functions for quadrilaterals [116]. For surfaces, the subdomains are often referred to as patches. The term *element* is used to denote a general type of subdomain, such as a wire segment, a surface patch, or a volumetric cell. RWG and rooftop functions provide a piecewise linear expansion of the surface current, thus the current is expanded in terms of 1st order polynomials. Higher-order basis functions are subsectional basis functions that provide a piecewise 2nd, 3rd, or even higher-order polynomial expansion. The high-order expansion allows the size of element to be increased and the overall number of basis functions to be decreased in comparison with a 1st order expansion [117].

For expansion of the surface current in a MoM solution, normal continuity of a vector quantity between neighboring elements is required to avoid buildup of line charges at the boundary between adjacent patches. The information embedded in the continuity equation also provides an important reduction in the number of unknowns.

For surfaces, the expansion order is often taken to be one order higher along the direction of current flow than along the transverse direction. For example, a rooftop function provides a 1st-order expansion of the surface current along the direction of current flow but is constant along the transverse direction. This implicitly results in a surface charge that is constant along both directions. Adding an additional unknown to obtain a linear current expansion also in the transverse direction would not increase the overall accuracy of the solution since the surface charge would still be constant along the direction of current flow.

The choice of basis functions is always a tradeoff among different properties. Four factors, proposed in [88], may affect the choice of basis functions:

(1) the accuracy of the solution desired, (2) the ease of evaluation of the matrix elements, (3) the size of the matrix that can be inverted, and (4) the realization of a well-conditioned matrix.

These factors are still valid today. Low-order basis functions are appropriate when considering (2) and (4) but not (1) and (3). The existing higher-order basis functions are appropriate when considering (1) and (3) but not (2) and (4).

2.4 Discussion

This chapter has presented the basic theory of integral equation technique. Integral equations for electromagnetic problems are derived by establishing a source-field relationship, employing an equivalence principle, and enforcing a boundary condition. The concept of DGFs is presented in both spatial and spectral spaces in the condition of homogeneous medium and multilayered media. The MoM was introduced as a discretization scheme for integral equations and the choice of basis functions and their properties were discussed.

Generally, the surface integral equation method is rather popular in a number of applications, because it employs a homogeneous medium Green's function which is simple in form, and the unknowns are on a surface rather than in a volume. However, sometimes the volume integral equations are more useful not only because its ability for bounded inhomogeneities but also for some special cases of waveguides. We will mainly use volume integral equations to model the dielectric for the NRD based circuits in this thesis and will show how the volume integral equation can be reduced to a surface integral equation problem be carrying out one dimensional integral analytically. The reduced volume integral equation technique is much simpler than its surface counterpart. Of course, the microstrips and slots will be described by surface integral equations and form the surface-volume integral equation method for hybrid planar/NRD integrated structures.

One of the crucial points of the MoM lies in effective and accurate evaluation of the system matrix entries in (2.52). These elements can either be carried out in space domain or in spectral domain. In the space domain, the type of the subdomain of basis functions is flexible and is suitable for objects with irregular shapes. However, the DGF in the integral equations does not have a closed form and has to be obtained from a Sommerfeld-type integral. Since the kernel is highly singular, the evaluation of the integrals in the moment method procedure is difficult when the observation point is within the integration range. The mixed potential integral equation (MPIE), which is a modification of the EFIE, is usually solved in the space domain. In comparison with the EFIE in the space domain, the kernel in the MPIE is less singular, which makes the evaluation of integrals more numerically simple and stable for two nearby elements.

In the spectral domain, a closed-form expression for the DGF can be obtained after satisfying the boundary conditions at the interface of multi-layer stratified dielectric medium as in section 2.2.2. The space domain electromagnetic fields can be expressed as the inverse Fourier transform of the vector product of this spectral-domain dyadic Green's function and Fourier transform of the microstrip currents. This method has the limitation on the shape of subdomain of the basis functions because Fourier transform of the basis function is needed. Since most structures we encounter in practice have a regular shape, we will carry out entries of matrix in spectral domain in this thesis. The formulation in the spectral domain has several advantages over the space domain analyses. One advantage is that the integration path may be chosen to avoid singularities, thus yielding a smoothly varying integrand. A second advantage is the opportunity to independently determine both radiation and surface-wave losses in planar circuits. One can compute the impedance matrix in the MoM very accurately using the spectral domain formulation such that the circuit parameters in a microstrip junction can be rigorously determined.

CHAPTER 3

GUIDED WAVE PROPERTIES OF THE STANDARD NRD-GUIDE AND H-GUIDE

3.1 Introduction

Guided wave properties of the standard NRD-guide are very important in the understanding of design rules for NRD-guide circuits. Since H-guides share the same structure with NRD-guides except that the distance between the two plates is larger than half the wavelength, they have similar guide wave properties to NRD-guides [118]. The emphasis in the case of the H-guide is on achieving low-loss propagation rather than the non-radiative property by virtue of having a large plate separation. The integral equation techniques developed in the following chapters are also suitable for H-guides. In this chapter, we will discuss them together and use a unified name "Dielectric strip loaded parallel-plate guide" for them.

The guided wave properties of the dielectric strip loaded parallel-plate guide also play a critical role in the integral equation techniques developed in this thesis. The analytical field expressions of hybrid modes are used in entire modes in integral equation approaches and make the port treatment extremely simple. The mode spectrum of the dielectric strip loaded parallel-plate guide provides a basis for multiple-mode analysis in the surface-volume integral equation approach. The cutoff frequencies of continuous modes correspond to the poles in the Green's functions and provide an explanation on the leakage loss on modified NRD-guides and the radiation loss on H-guide circuits and the hybrid planar/NRD-guide integrated circuits. Characteristics of the coupled standard-NRD-guide are also discussed in this chapter for the comparison with a bridged NRD-guide coupler proposed in the next chapter. In a word, the analysis of modal properties of dielectric loaded parallel-plate guides will help us to easily understand the field concepts in the following chapters.

In this chapter, we first derive general field expressions for the hybrid-modes of a dielectric strip loaded parallel-plate guide. The mode spectrum of the guide is discussed as follows. Characteristics of the coupled NRD guide are presented in section 3.4.

3.2 Field Expressions of the Eigen-Modes in Dielectric Strip Loaded Parallel-Plate Guide

Referring to the structure and the coordinate system as shown in Fig. 3.1, the hybrid modes of the dielectric strip loaded parallel-plate guide are classified into a combination of longitudinal-section-magnetic (LSM) modes and longitudinal-section-electric (LSE) modes. The LSM are also referred to as TM modes to y (TM^{y}_{mn}) or E^{y}_{mn} modes to indicate that the magnetic field lines lie entirely in planes perpendicular to the y-axis (H_y=0) or E_y is the dominant electric field component. Similarly, the LSE modes are also referred to as TE modes to y (TE^{y}_{mn}) or E^{z}_{mn} modes to indicate that the electric field lines lie entirely in planes perpendicular to the y-axis (E_y=0) or E_z is the dominant electric field component. For ease of our analysis, we make use of the symmetry of the structure about the y=0 plane and identify LSM_{mn} modes as symmetric or antisymmetric depending on whether the E_y component is symmetric or antisymetric with reference to y=0. Similarly, we identify LSE_{mn} modes as symmetric or antisymmetric depending on whether the E_z component is symmetric or antisymmetric with reference to the same plane.

In a homogeneous lossless dielectric, the **E** and **H** fields can be expressed in the forms

$$\mathbf{E} = -\nabla\times\mathbf{F} - j\omega\mu\mathbf{A} + \frac{1}{j\omega\varepsilon}\nabla(\nabla\cdot\mathbf{A}) \tag{3.1}$$

$$\mathbf{H} = \nabla\times\mathbf{A} - j\omega\varepsilon\mathbf{F} + \frac{1}{j\omega\mu}\nabla(\nabla\cdot\mathbf{F}) \tag{3.2}$$

where **F** and **A** are called the electric vector potential and magnetic vector potential, respectively.

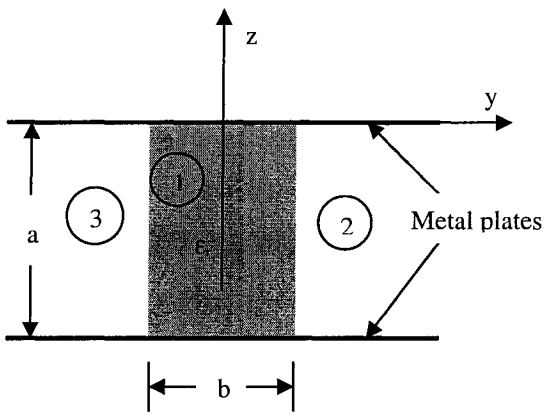

Figure 3.1. Cross-section of a dielectric strip loaded parallel-plate waveguide.

3.2.1 Field Expressions for LSM_{mn} Modes (H_y=0)

For the LSM (TM-to-y) solution we consider **F**=0 and $\mathbf{A} = \hat{\mathbf{y}} j\omega\varepsilon_0\phi^e$, where ϕ^e is a scalar potential function. Equations (3.1) and (3.2) are then reduced to

$$\mathbf{E} = -j\omega\mu_0\mathbf{A} + \frac{1}{j\omega\varepsilon}\nabla(\nabla\cdot\mathbf{A}) \tag{3.3}$$

$$\mathbf{H} = \nabla\times\mathbf{A} \tag{3.4}$$

The scalar potential ϕ^e satisfies the Helmholtz equation

$$(\nabla^2 + k^2)\phi^e = 0 \tag{3.5}$$

Referring to the coordinate system as shown in Figure 3.1, we assume wave propagation along the guide with fields varying according to $e^{j(\omega t-\beta x)}$, where β is the propagation constant for the LSM modes. We note that E_y is proportional to ϕ^e as given by the relation

$$E_y = \left(k_0^2 + \frac{1}{\varepsilon_r}\frac{\partial^2}{\partial y^2} \right)\phi^e \tag{3.6}$$

Thus the symmetric and antisymmetric LSM fields can be obtained from the expressions for ϕ^e, which are symmetric and antisymmetric at y=0. For symmetric modes, the plane y=0 represents an electric wall and for antisymmetric modes, it represents a magnetic wall.

LSM_{mn} Symmetric Modes. Referring to Figure 3.1, the expressions for ϕ^e in dielectric and air regions can be written as

$$\phi^e = \begin{cases} A\sin\left(m\pi\left(z+a\right)/a\right)\cos\left(\beta_y y\right) & |y| < b/2 \\ A\sin\left(m\pi\left(z+a\right)/a\right)\cos\left(\beta_y b/2\right)e^{\varsigma(b/2-|y|)} & |y| > b/2 \end{cases} \tag{3.7}$$

where A is an arbitrary constant, β_y is the y-directed propagation constant in the dielectric region, and ζ is the decay constant in the air region. The common factor $\exp^{[j(\omega t-\beta x)]}$ has been suppressed from (3.7). Parameters β, β_y, and ζ are related by

$$\beta^2 = k_0^2\varepsilon_r - \left(m\pi/a\right)^2 - \beta_y^2 = k_0^2 - \left(m\pi/a\right)^2 + \zeta^2 \tag{3.8}$$

Various field components of the LSM symmetric modes can now be obtained in terms of the single unknown constant A by substituting for ϕ^e from (3.7) in (3.3) and (3.4).

$$E_x = \begin{cases} -j\left(A/\varepsilon_r\right)\beta\beta_y \sin\left(m\pi\left(z+a\right)/a\right)\sin\left(\beta_y y\right) & |y| < b/2 \\ \pm jA\beta\varsigma \sin\left(m\pi\left(z+a\right)/a\right)\cos\left(\beta_y b/2\right)e^{\varsigma(b/2-|y|)} & |y| > b/2 \end{cases} \tag{3.9a}$$

$$E_y = \begin{cases} \left(A/\varepsilon_r\right)g^2 \sin\left(m\pi\left(z+a\right)/a\right)\cos\left(\beta_y y\right) & |y| < b/2 \\ Ag^2 \sin\left(m\pi\left(z+a\right)/a\right)\cos\left(\beta_y b/2\right)e^{\varsigma(b/2-|y|)} & |y| > b/2 \end{cases} \tag{3.9b}$$

$$E_z = \begin{cases} -A\left(\beta_y/\varepsilon_r\right)\left(m\pi/a\right)\cos\left(m\pi\left(z+a\right)/a\right)\sin\left(\beta_y y\right) & |y| < b/2 \\ \mp A\left(m\pi/a\right)\cos\left(m\pi\left(z+a\right)/a\right)\cos\left(\beta_y b/2\right)e^{\varsigma(b/2-|y|)} & |y| > b/2 \end{cases} \tag{3.9c}$$

$$H_x = \begin{cases} -jA\omega\varepsilon_0\left(m\pi/a\right)\cos\left(m\pi\left(z+a\right)/a\right)\cos\left(\beta_y y\right) & |y| < b/2 \\ jA\omega\varepsilon_0\left(m\pi/a\right)\cos\left(m\pi\left(z+a\right)/a\right)\cos\left(\beta_y b/2\right)e^{\varsigma(b/2-|y|)} & |y| > b/2 \end{cases} \tag{3.9d}$$

$$H_y = 0 \tag{3.9e}$$

$$H_z = \begin{cases} -A\omega\varepsilon_0\beta \sin\left(m\pi\left(z+a\right)/a\right)\cos\left(\beta_y y\right) & |y| < b/2 \\ -A\omega\varepsilon_0\beta \sin\left(m\pi\left(z+a\right)/a\right)\cos\left(\beta_y b/2\right)e^{\varsigma(b/2-|y|)} & |y| > b/2 \end{cases} \tag{3.9f}$$

where the upper and lower signs in (3.9) apply to air regions 2 and 3, respectively, and g is given by

$$g^2 = \beta^2 + \left(m\pi/a\right)^2 = k_0^2\varepsilon_r - \beta_y^2 = k_0^2 + \varsigma^2 \tag{3.10}$$

LSM_{mn} Antisymmetric Modes. The expressions for ϕ^e in the dielectric and air regions are given by

$$\phi^e = \begin{cases} B\sin\left(m\pi\left(z+a\right)/a\right)\sin\left(\beta_y y\right) & |y| < b/2 \\ B\sin\left(m\pi\left(z+a\right)/a\right)\sin\left(\beta_y b/2\right)e^{\varsigma(b/2-|y|)} & |y| > b/2 \end{cases} \tag{3.11}$$

where the parameters β, β_y, and ζ are related as in (3.8). Various field components of the LSM antisymmetric modes can be obtained in terms of the single unknown constant B by substituting for ϕ^e from (3.11) in (3.3) and (3.4).

$$E_x = \begin{cases} j\left(B/\varepsilon_r\right)\beta\beta_y \sin\left(m\pi\left(z+a\right)/a\right)\cos\left(\beta_y y\right) & |y| < b/2 \\ jB\beta\varsigma \sin\left(m\pi\left(z+a\right)/a\right)\sin\left(\beta_y b/2\right)e^{\varsigma(b/2-|y|)} & |y| > b/2 \end{cases} \tag{3.12a}$$

$$E_y = \begin{cases} \left(B/\varepsilon_r\right)g^2 \sin\left(m\pi\left(z+a\right)/a\right)\sin\left(\beta_y y\right) & |y| < b/2 \\ \pm Bg^2 \sin\left(m\pi\left(z+a\right)/a\right)\sin\left(\beta_y b/2\right)e^{\varsigma(b/2-|y|)} & |y| > b/2 \end{cases} \tag{3.12b}$$

$$E_z = \begin{cases} B\left(\beta_y/\varepsilon_r\right)\left(m\pi/a\right)\cos\left(m\pi\left(z+a\right)/a\right)\cos\left(\beta_y y\right) & |y| < b/2 \\ -B\left(m\pi/a\right)\cos\left(m\pi\left(z+a\right)/a\right)\sin\left(\beta_y b/2\right)e^{\varsigma(b/2-|y|)} & |y| > b/2 \end{cases} \tag{3.12c}$$

$$H_x = \begin{cases} -jB\omega\varepsilon_0\left(m\pi/a\right)\cos\left(m\pi\left(z+a\right)/a\right)\sin\left(\beta_y y\right) & |y| < b/2 \\ \pm jB\omega\varepsilon_0\left(m\pi/a\right)\cos\left(m\pi\left(z+a\right)/a\right)\sin\left(\beta_y b/2\right)e^{\varsigma(b/2-|y|)} & |y| > b/2 \end{cases} \tag{3.12d}$$

$$H_y = 0 \tag{3.12e}$$

$$H_z = \begin{cases} -B\omega\varepsilon_0\beta \sin\left(m\pi\left(z+a\right)/a\right)\sin\left(\beta_y y\right) & |y| < b/2 \\ \mp B\omega\varepsilon_0\beta \sin\left(m\pi\left(z+a\right)/a\right)\sin\left(\beta_y b/2\right)e^{\zeta(b/2-|y|)} & |y| > b/2 \end{cases} \tag{3.12f}$$

where the upper and lower signs in (3.12) apply to air regions 2 and 3, respectively, and g is given by (3.10).

3.2.2 Field Expressions for LSE_{mn} Modes (E_y=0)

For the LSE (TE-to-y) solution, we consider **A**=0 and $\mathbf{F} = \hat{\mathbf{y}} j\omega\mu_0\phi^h$, where ϕ^h is a scalar potential function. Equations (3.1) and (3.2) are then reduced to

$$\mathbf{E} = -\nabla\times\mathbf{F} \tag{3.13}$$

$$\mathbf{H} = -j\omega\varepsilon\mathbf{F} + \frac{1}{j\omega\mu_0}\nabla\left(\nabla\cdot\mathbf{F}\right) \tag{3.14}$$

The scalar potential function ϕ^h satisfies the Helmholtz equation

$$\left(\nabla^2 + k^2\right)\phi^h = 0 \tag{3.15}$$

Let us consider propagation of LSE modes along the guide with fields varying according to $e^{j(\omega t-\beta x)}$, where β is the propagation constant in the x-direction. Similarly, E_z is proportional to ϕ^h and given by

$$E_z = -\omega\mu_0\beta\phi^h \tag{3.16}$$

Thus the symmetric and antisymmetric LSE fields can be obtained from the expressions for ϕ^h, which are symmetric and antisymmetric at y=0. For symmetric modes, the plane y=0 represents a magnetic wall, and for antisymmetric modes, it represents an electric wall.

LSE_{mn} Symmetric Modes. Referring to Figure 3.1, the expressions for ϕ^h in the dielectric and air regions can be written as

$$\phi^h = \begin{cases} C\cos\left(m\pi\left(z+a\right)/a\right)\cos\left(\beta_y y\right) & |y| < b/2 \\ C\cos\left(m\pi\left(z+a\right)/a\right)\cos\left(\beta_y b/2\right)e^{\varsigma(b/2-|y|)} & |y| > b/2 \end{cases} \tag{3.17}$$

where parameters β_y and ζ are related to β through (3.8)

Substituting for ϕ^h from (3.17) in (2.13 and (3.14) and replacing $\partial/\partial x$ by -jβ, we obtain various field expressions in terms of a single unknown constant C.

$$E_x = \begin{cases} -jC\omega\mu_0\left(m\pi/a\right)\sin\left(m\pi\left(z+a\right)/a\right)\cos\left(\beta_y y\right) & |y| < b/2 \\ -jC\omega\mu_0\left(m\pi/a\right)\sin\left(m\pi\left(z+a\right)/a\right)\cos\left(\beta_y b/2\right)e^{\varsigma(b/2-|y|)} & |y| > b/2 \end{cases} \tag{3.18a}$$

$$E_y = 0 \tag{3.18b}$$

$$E_z = \begin{cases} C\omega\mu_0\beta\cos\left(m\pi\left(z+a\right)/a\right)\cos\left(\beta_y y\right) & |y| < b/2 \\ C\omega\mu_0\beta\cos\left(m\pi\left(z+a\right)/a\right)\cos\left(\beta_y b/2\right)e^{\varsigma(b/2-|y|)} & |y| > b/2 \end{cases} \tag{3.18c}$$

$$H_x = \begin{cases} -jC\beta\beta_y\cos\left(m\pi\left(z+a\right)/a\right)\sin\left(\beta_y y\right) & |y| < b/2 \\ \pm jC\beta\varsigma\cos\left(m\pi\left(z+a\right)/a\right)\cos\left(\beta_y b/2\right)e^{\varsigma(b/2-|y|)} & |y| > b/2 \end{cases} \tag{3.18d}$$

$$H_y = \begin{cases} Cg^2\cos\left(m\pi\left(z+a\right)/a\right)\cos\left(\beta_y y\right) & |y| < b/2 \\ Cg^2\cos\left(m\pi\left(z+a\right)/a\right)\cos\left(\beta_y b/2\right)e^{\zeta(b/2-|y|)} & |y| > b/2 \end{cases} \tag{3.18e}$$

$$H_z = \begin{cases} C\beta_y\left(m\pi/a\right)\sin\left(m\pi z/a\right)\sin\left(\beta_y y\right) & |y| < b/2 \\ \pm C\zeta\left(m\pi/a\right)\sin\left(m\pi z/a\right)\cos\left(\beta_y b/2\right)e^{\varsigma(b/2-|y|)} & |y| > b/2 \end{cases} \tag{3.18f}$$

where the upper and lower signs in (3.18) apply to air regions 2 and 3, respectively,

LSE_{mn} Antisymmetric Modes. For this set of modes, E_z is antisymmetric at y=0 plane and the scalar potential ϕ^h takes the form as follows

$$\phi^h = \begin{cases} D\cos\left(m\pi\left(z+a\right)/a\right)\sin\left(\beta_y y\right) & |y| < b/2 \\ D\cos\left(m\pi\left(z+a\right)/a\right)\sin\left(\beta_y b/2\right)e^{\varsigma(b/2-|y|)} & |y| > b/2 \end{cases} \tag{3.19}$$

where the parameters β_y and ζ are related by (3.10). Substituting for ϕ^h from (3.19) in (3.13) and (3.14) and replacing $\partial/\partial x$ by -jβ, we obtain the following field expressions:

$$E_x = \begin{cases} -jD\omega\mu_0 (m\pi/a)\sin(m\pi(z+a)/a)\sin(\beta_y y) & |y| < b/2 \\ \mp jD\omega\mu_0 (m\pi/a)\sin(m\pi(z+a)/a)\sin(\beta_y b/2)e^{\varsigma(b/2-|y|)} & |y| > b/2 \end{cases} \quad (3.20a)$$

$$E_y = 0 \quad (3.20b)$$

$$E_z = \begin{cases} D\omega\mu_0\beta\cos(m\pi(z+a)/a)\sin(\beta_y y) & |y| < b/2 \\ \pm D\omega\mu_0\beta\cos(m\pi(z+a)/a)\sin(\beta_y b/2)e^{\varsigma(b/2-|y|)} & |y| > b/2 \end{cases} \quad (3.20c)$$

$$H_x = \begin{cases} jD\beta\beta_y\cos(m\pi(z+a)/a)\cos(\beta_y y) & |y| < b/2 \\ -jD\beta\zeta\cos(m\pi(z+a)/a)\sin(\beta_y b/2)e^{\varsigma(b/2-|y|)} & |y| > b/2 \end{cases} \quad (3.20d)$$

$$H_y = \begin{cases} Dg^2\cos(m\pi(z+a)/a)\sin(\beta_y y) & |y| < b/2 \\ \pm Dg^2\cos(m\pi(z+a)/a)\sin(\beta_y b/2)e^{\zeta(b/2-|y|)} & |y| > b/2 \end{cases} \quad (3.20e)$$

$$H_z = \begin{cases} -D\beta_y (m\pi/a)\sin(m\pi z/a)\cos(\beta_y y) & |y| < b/2 \\ D\zeta (m\pi/a)\sin(m\pi z/a)\sin(\beta_y b/2)e^{\varsigma(b/2-|y|)} & |y| > b/2 \end{cases} \quad (3.20f)$$

3.3 Mode Spectrum of Dielectric Strip Loaded Parallel-Plate Guide

The mode spectrum in the dielectric strip loaded parallel-plate guide can be divided into a discrete number of surface-waves, which are classified into LSE and LSM modes, and a continuous set of radiation modes. As far as the eigenvalue problem is concerned, the presence of the parallel metal plates implies a discretization of the vertical wave number (β_z=mπ/a, with null or integer m) while the horizontal wave numbers can be derived from transcendental equations related to the dielectric slab guide. The transcendental equations for the eigenvalues along y can be obtained by matching E_z and H_z at the air-dielectric interfaces as

$$\beta_y \cdot \begin{Bmatrix} \tan(\beta_y b/2) \\ \cot(\beta_y b/2) \end{Bmatrix} = \begin{Bmatrix} + \\ - \end{Bmatrix} p\varsigma \quad \begin{cases} \text{symmetric} & \text{modes} \\ \text{antisymmetric} & \text{modes} \end{cases} \quad (3.21)$$

where p=1 for LSE modes and p=ε_r for LSM modes. β_y, and ζ have an analytical relationship as follows:

$$\zeta^2 = k_0^2(\varepsilon_r - 1) - \beta_y^2 \tag{3.22}$$

Solving the transcendental equations gives rise to a system of eigenvalues with odd integers n (n=1,3,5,..) in symmetrical modes and even integers n (n=2,4,6,..) in anti-symmetric modes. The propagation constants are then obtained by

$$\beta_{nm}^2 = k_0^2\varepsilon_r - (m\pi/a)^2 - \beta_{yn}^2 \quad \text{m=1,2,3,...;} \quad \text{n=1,2,3,...} \tag{3.23}$$

Surface-wave modes occur at $\zeta^2>0$ where β satisfies $k_0^2 < \beta^2 + (m\pi/a)^2 < \varepsilon_r k_0^2$. Radiation modes appear while $\zeta^2 < 0$ where β satisfies $\beta^2 + (m\pi/a)^2 < k_0^2$. In this case, the waves can propagate away at an angle from the dielectric strip on both sides.

The space of the mode spectrum can be divided into surface wave modes, continuous radiation modes, and prohibited regions as depicted in Fig. 3.2 by simply defining two boundary lines $\gamma_1 = (\alpha_1, \beta_1)$ and $\gamma_2 = (\alpha_2, \beta_2)$ in $(\alpha, \beta) - \lambda_0$ diagram where α is decay constant, β is propagation constant, and

$$\alpha_1 = \sqrt{\left(\frac{m\pi}{a}\right)^2 - \varepsilon_r k_0^2} \qquad \varepsilon_r k_0 < m\pi/a$$

$$\beta_1 = \sqrt{\varepsilon_r k_0^2 - \left(\frac{m\pi}{a}\right)^2} \qquad \varepsilon_r k_0 > m\pi/a$$

$$\alpha_2 = \sqrt{\left(\frac{m\pi}{a}\right)^2 - k_0^2} \qquad k_0 < m\pi/a$$

$$\beta_2 = \sqrt{k_0^2 - \left(\frac{m\pi}{a}\right)^2} \qquad k_0 > m\pi/a$$

A full spectrum for m=0, 1, 2 was generated (with a=5.0 mm, b=3.556 mm and ε_r=2.56) as shown in Fig. 3.2. In the case of m=0 as described in Fig. 3.2(a), the LSE modes reduce to TE_{n0} modes and no TM_{n0} modes exist. The fundamental guided TE mode, TE_{10} mode, and the propagating radiation mode exist over all frequency ranges. The

propagating radiation mode may cause the leakage loss in modified NRD-guides and radiation loss in hybrid planar/NRD-guide integrated circuits. The higher-order TE modes, namely, TE_{20} and TE_{30} modes, merge to a continuous radiation mode at low frequency range where $\zeta^2<0$. The boundaries γ_1, γ_2 shift to a high frequency region in the

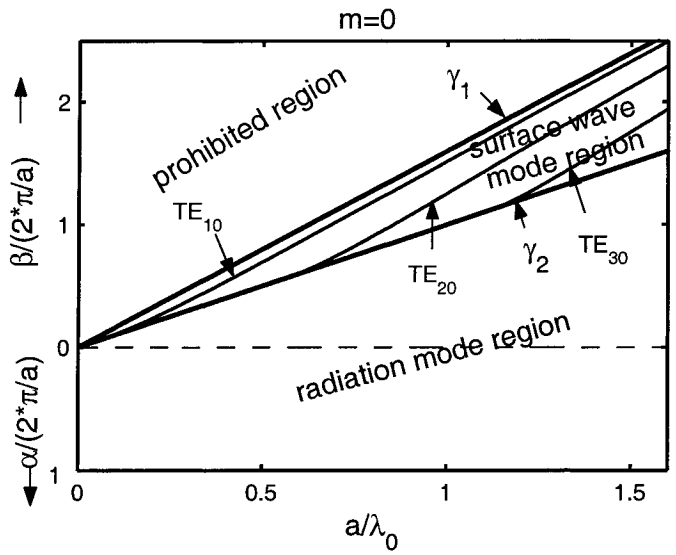

(a)

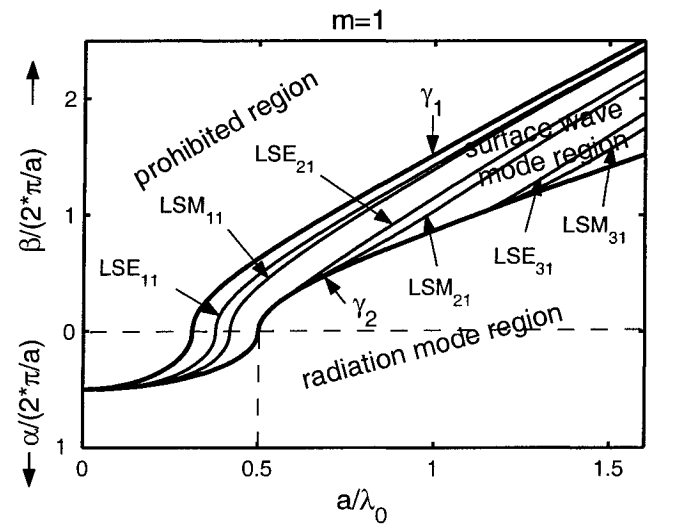

(b)

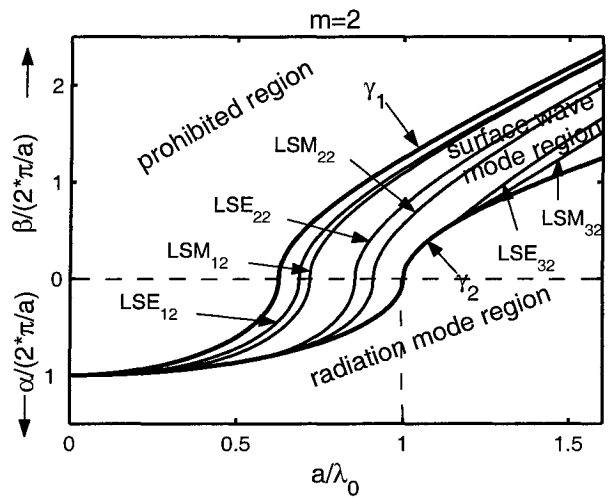

(c)

Fig.3.2. Mode spectrum of NRD-guide and H-guide. (a) m=0 spectral condition. (b) m=1 spectral condition, (c) m=2 spectral condition.

case of m=1 as shown in Fig. 3.2(b). The continuous radiation mode becomes completely evanescent in the $a/\lambda_0<0.5$ region where the structure works as an NRD guide. The radiation mode is partly evanescent and partly propagating in the $a/\lambda_0>0.5$ region where the structure works as an H-guide. Only the propagating radiation mode can cause radiation loss and this is why the NRD-guide can suppress radiation loss at bends and discontinuities with the operating mode LSM_{11}. The case of m=2 is similar to that of m=1 where the boundaries γ_1, γ_2 shift to a higher frequency range and the radiation mode cuts off at $a/\lambda_0 = 1$ as shown in Fig. 3.2(c). We will see in Chapters 4 and 5 that the cutoff points of radiation modes correspond to the poles in the Green's functions and play an important role in the integral equation techniques.

3.4 Characteristics of Coupled NRD Guide

Characteristics of coupled NRD guides made of edge-coupled dielectric strips are important in the design of directional couplers and filters. For a symmetrically coupled NRD guide as shown in Figure 3.3, the LSM fields may be considered as a superposition of even and odd modes propagating longitudinally with different propagation constants β_e and β_o, respectively. The symmetry plane y=0 is assumed to be an electric wall for the even modes and a magnetic wall for the odd mode. For the LSM-type fields, the scalar potentials ϕ^e satisfying the helmholtz equation in the three regions marked in Fig. 3.3 can be expressed as

$$\begin{aligned}\phi^e &= A\sin\left(m\pi\left(z+a\right)/a\right)e^{-\varsigma y} && |y| > b+d/2 \\ &= \sin\left(m\pi\left(z+a\right)/a\right)\left[B\cos\left(\beta_y y\right)+C\sin\left(\beta_y y\right)\right] && d/2<|y|<b+d/2 \quad (3.24) \\ &= D\sin\left(m\pi\left(z+a\right)/a\right)\begin{cases}\sinh\left(\varsigma y\right), \text{evenmode} \\ \cosh\left(\varsigma y\right), \text{oddmode}\end{cases} && 0<|y|<d/2\end{aligned}$$

Substituting for ϕ^e in (3.3) and setting $\partial/\partial x = -j\beta$, we can obtain expressions for all the field components. The E_x and E_y components are given by

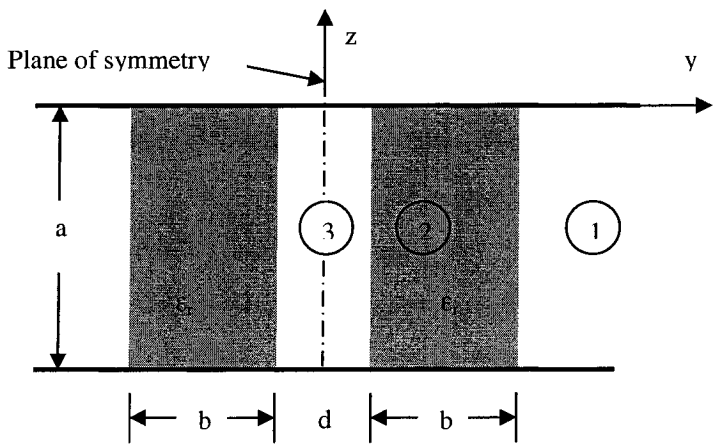

Fig. 3.3. Parallel-coupled NRD guide.

$$
\begin{aligned}
E_x &= jA\beta\varsigma \sin\left(m\pi\left(z+a\right)/a\right)e^{-\varsigma y} && |y| > b+d/2 \\
&= -j\left(1/\varepsilon_r\right)\beta\beta_y \sin\left(m\pi\left(z+a\right)/a\right) \\
&\qquad \left[-B\sin\left(\beta_y y\right)+C\cos\left(\beta_y y\right)\right] && d/2 < |y| < b+d/2 \qquad (3.25a) \\
&= -jD\beta\varsigma \sin\left(m\pi\left(z+a\right)/a\right)\begin{cases}\cosh\left(\varsigma y\right), & \text{evenmode} \\ \sinh\left(\varsigma y\right), & \text{oddmode}\end{cases} && 0 < |y| < d/2
\end{aligned}
$$

$$
\begin{aligned}
E_y &= Ag^2 \sin\left(m\pi\left(z+a\right)/a\right)e^{-\varsigma y} && |y| > b+d/2 \\
&= \left(g^2/\varepsilon_r\right)\cos\left(m\pi\left(z+a\right)/a\right)\left[B\cos\left(\beta_y y\right)+C\sin\left(\beta_y y\right)\right] && d/2 < |y| < b+d/2 \qquad (3.25b) \\
&= Dg^2 \sin\left(m\pi\left(z+a\right)/a\right)\begin{cases}\sinh\left(\varsigma y\right), & \text{evenmode} \\ \cosh\left(\varsigma y\right), & \text{oddmode}\end{cases} && 0 < |y| < d/2
\end{aligned}
$$

where

$$g^2 = \beta^2 + \left(m\pi/a\right)^2 = k_0^2\varepsilon_r - \beta_y^2 = k_0^2 + \varsigma^2 \qquad (3.26)$$

Applying the boundary conditions at the air-dielectric interfaces y=d/2 and y=b+d/2, we obtain the following characteristic equation:

$$\frac{\beta_y\left[\beta_y \tan\left(\beta_y b\right)-\varepsilon_r\varsigma\right]}{\varepsilon_r\varsigma\left[\varepsilon_r\varsigma \tan\left(\beta_y b\right)+\beta_y\right]} = \begin{cases}\coth\left(\varsigma d/2\right), \text{evenmode} \\ \tanh\left(\varsigma d/2\right), \text{oddmode}\end{cases} \qquad (3.27)$$

The solution of (3.27) in conjunction with (3.26) yields the even- and odd-mode propagation constants β_e and β_o of the dominant LSM mode.

Fig. 3.4 shows the coupled guide characteristics in terms of the coupling coefficient as a function of the strip spacing normalized with respect to the free-space wavelength λ_0. The coupling coefficient is defined as

$$C = 0.5\left(\beta_e - \beta_o\right) \qquad (3.28)$$

And the 0-dB coupling length L_c required for complete power transfer from one guide to the other is given by

$$L_c = \frac{\pi}{2C} = \frac{\pi}{\beta_e - \beta_o} \qquad (3.29)$$

It can be seen from Figure 3.4 that for all the three dielectric chosen (ε_r=2.04, 2.56, 9.5),

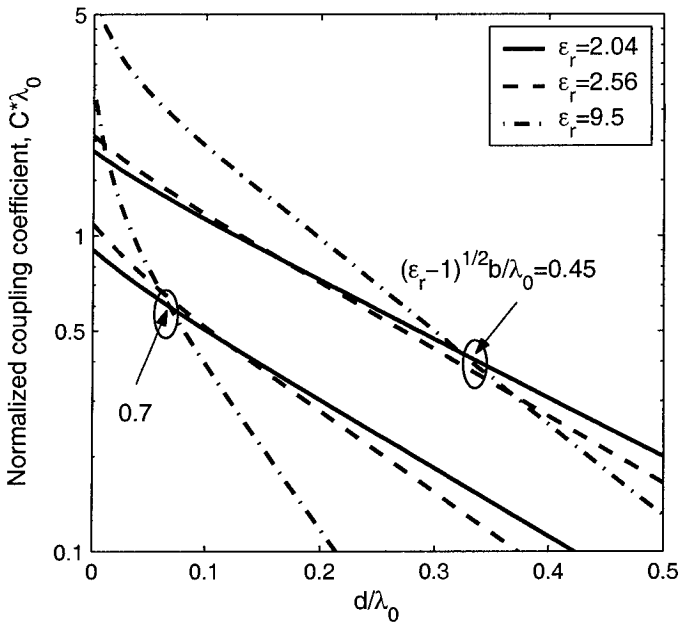

Fig. 3.4. Normalized coupling coefficient for coupled strips of Teflon (ε_r=2.04), Polystyrene (ε_r=2.56), and Alumina (ε_r=9.5).

a smaller value of $b\sqrt{(\varepsilon_r - 1)}/a$ gives a large coupling coefficient. This is an expected result since, for strips of smaller width b and lower dielectric constant ε_r, fields extend over larger distances in the transverse direction, thereby enhancing the coupling.

3.5 Summary

The eigen modes in the standard NRD-guide and H-guide can be divided into a discrete number of surface-waves, which are classified into LSE and LSM modes, and a continuous set of radiation modes. The field expressions of the LSM and LSE modes, including symmetric mode and anti-symmetric modes, have been obtained analytically. The space of the mode spectrum can be divided into surface wave modes, continuous radiation modes, and prohibited regions. The propagating radiation mode exist over all frequency range in the m=0 case, and thus may cause leakage loss in modified NRD-

guides and radiation loss in hybrid planar/NRD-guide integrated circuits. In the m=1 case, the continuous radiation mode becomes completely evanescent in the $a/\lambda_0<0.5$ region where the structure works as an NRD guide while it is partly evanescent and partly propagating in the $a/\lambda_0>0.5$ region where the structure works as an H-guide. The coupling properties of the coupled NRD-guide were discussed and indicate that a smaller value of $b\sqrt{(\varepsilon_r - 1)}/a$ gives a larger coupling coefficient.

CHAPTER 4

INTEGRAL EQUATION SOLUTION TO THE GUIDED WAVE PROPERTIES OF MODIFIED NRD-GUIDES

4.1 Introduction

Propagation constants and field distributions of the standard NRD-guide and H-guide can be obtained analytically as in Chapter 3. Unfortunately, most of the modified NRD-guides in section 1.2.2 have no analytical solution and the guided wave properties have to be obtained through numerical methods. In [91], an EFIE method, which is based on volume integral equation techniques, has been proposed for the analysis of dielectric waveguides in multilayered media. Because of its rigorous full wave formulation, the EFIE techniques are capable of handling both open and closed structures and also describing physical effects such as leakage. Due to these advantages, this method has been used for many dielectric waveguides, such as an integral optical channel and ridge waveguides [92], coupled dielectric strip waveguides [93].

In this chapter, the EFIE method will be used for modeling the guided wave properties of modified NRD-guides. The integral equation solution to the propagation constants of modified NRD-guide is obtained and the condition of guidance and leakage modes for a simple modified NRD-guide is discussed. As an important application, a new NRD-guide directional coupler using two NRD waveguides interconnected with a bridge is proposed and analyzed base on the EFIE method. The coupler has several useful features as a passive component for millimeter-wave integrated circuits such as compact, broadband, and mechanical stable.

In what follows, the integral equation solution to the guidance and leakage properties of a modified NRD-guide will be presented first. Then the method will be used for the analysis and design of a bridged NRD-guide coupler for millimeter-wave applications. Finally, a short summary will be presented in section 4.4.

4.2 Integral Equation Solution to the Guidance and Leakage Properties of Modified NRD-Guides

In this section, the EFIE for dielectric waveguides in multilayered media is formulated first. The solutions to the propagation constants of a general modified NRD-guide are given next. The guidance and leakage properties of modified NRD-guides are discussed and the asymptotic technique for numerical integration is presented.

4.2.1 Electric Field Integral Equations for dielectric waveguides in multilayered media

The geometrical configuration and coordinate system of the proposed waveguide in the analysis are depicted in Fig. 4.1 with its cross-section view. The whole structure is assumed to be uniform along the propagation direction x. Assuming that the permittivity of the dielectric strips is ε(ρ) ($\boldsymbol{\rho} = \hat{\mathbf{y}}y + \hat{\mathbf{z}}z$), the volume integral equation for the dielectric strips embedded in multilayered media is as follows:

$$\mathbf{E}(\mathbf{r}) = \omega^2 \mu_0 \iiint_V dV' \overline{\mathbf{G}}(\mathbf{r},\mathbf{r}') \cdot \delta\varepsilon(\mathbf{r}') \mathbf{E}(\mathbf{r}') \tag{4.1}$$

where $\delta\varepsilon(\mathbf{r}) = \varepsilon(\mathbf{r}) - \varepsilon_n$, and V is the space occupied by the dielectric strips.

The DGF $\overline{\mathbf{G}}(\mathbf{r},\mathbf{r}')$ in the spectral domain as:

$$\overline{\mathbf{G}}(\mathbf{r},\mathbf{r}) = \frac{j}{8\pi^2} \int\int_{-\infty}^{\infty} d\mathbf{k}_s e^{j\mathbf{k}_s \cdot (\mathbf{r}_s - \mathbf{r}_s')} \tilde{\tilde{\mathbf{G}}}_p(\mathbf{k}_s, z, z') - \frac{\hat{\mathbf{z}}\hat{\mathbf{z}}}{k^2} \delta(\mathbf{r} - \mathbf{r}') \tag{4.2}$$

where $\mathbf{k}_s = \hat{\mathbf{x}}k_x + \hat{\mathbf{y}}k_y$, $\mathbf{r}_s = \hat{\mathbf{x}}x + \hat{\mathbf{y}}y$, $\mathbf{r}_s' = \hat{\mathbf{x}}x' + \hat{\mathbf{y}}y'$ and $\tilde{\tilde{\mathbf{G}}}_p(\mathbf{k}_s, z, z')$ is the Fourier transform of the principal value part of $\overline{\mathbf{G}}(\mathbf{r},\mathbf{r}')$ with respect to $\mathbf{r}_s$. The second term in (4.2) is the source dyadic.

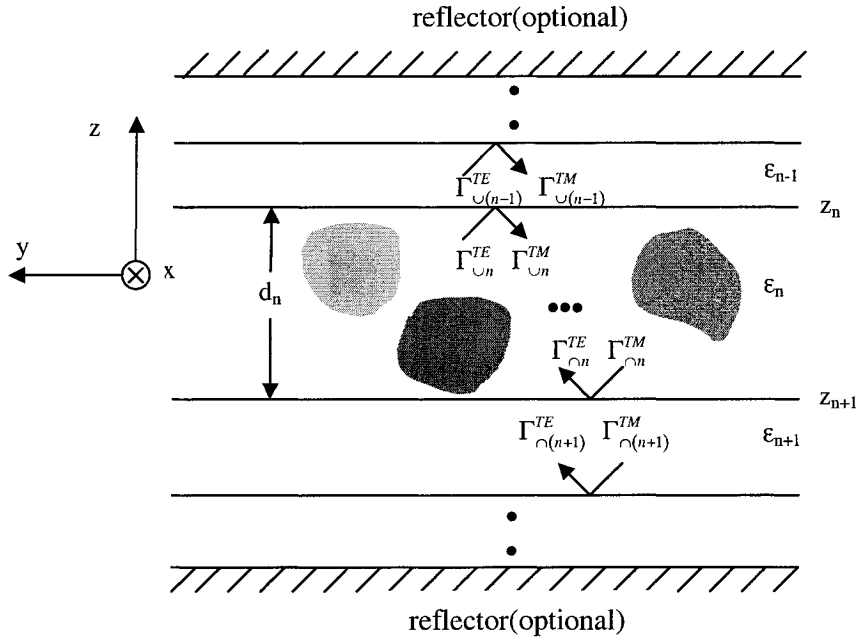

Fig. 4.1. The cross-section of N dielectric strips embedded in layer (n) of a multilayered medium.

The explicit form of $\bar{\bar{\mathbf{G}}}_p(\mathbf{k}_s, z, z')$ can be obtained from section 2.2. For $z > z'$, we have

$$\bar{\bar{\mathbf{G}}}_p(\mathbf{k}_s, z_>, z'_<) =$$
$$\frac{\left[\hat{\mathbf{h}}(k_{zn})e^{jk_{zn}(z-z_n)} + \Gamma^{TE}_{\cup n}\hat{\mathbf{h}}(-k_{zn})e^{jk_{zn}(2d_n-z+z_n)}\right]\left[\hat{\mathbf{h}}(k_{zn})e^{-jk_{zn}(z'-z_n)} + \Gamma^{TE}_{\cap n}\hat{\mathbf{h}}(-k_{zn})e^{jk_{zn}(z'-z_n)}\right]}{k_{zn}\left(1-\Gamma^{TE}_{\cup n}\Gamma^{TE}_{\cap n}e^{2jk_{zn}d_n}\right)}$$
$$+\frac{\left[\hat{\mathbf{v}}(k_{zn})e^{jk_{zn}(z-z_n)} + \Gamma^{TM}_{\cup n}\hat{\mathbf{v}}(-k_{zn})e^{jk_{zn}(2d_n-z+z_n)}\right]\left[\hat{\mathbf{v}}(k_{zn})e^{-jk_{zn}(z'-z_n)} + \Gamma^{TM}_{\cap n}\hat{\mathbf{v}}(-k_{zn})e^{jk_{zn}(z'-z_n)}\right]}{k_{zn}\left(1-\Gamma^{TM}_{\cup n}\Gamma^{TM}_{\cap n}e^{2jk_{zn}d_n}\right)} \tag{4.3a}$$

and for $z < z'$, we have

$$\bar{\bar{\mathbf{G}}}(\mathbf{k}_s, z_<, z_>') = \frac{\left[\hat{\mathbf{h}}(-k_{zn})e^{-jk_{zn}(z-z_n)} + \Gamma_{\cap n}^{TE}\hat{\mathbf{h}}(k_{zn})e^{jk_{zn}(z-z_n)}\right]\left[\hat{\mathbf{h}}(-k_{zn})e^{jk_{zn}(z'-z_n)} + \Gamma_{\cup n}^{TE}\hat{\mathbf{h}}(k_{zn})e^{jk_{zz}(2d_n-z'+z_n)}\right]}{k_{zn}\left(1-\Gamma_{\cup n}^{TE}\Gamma_{\cap n}^{TE}e^{2jk_{zn}d_n}\right)}$$
$$+\frac{\left[\hat{\mathbf{v}}(-k_{zn})e^{-jk_{zn}(z-z_n)} + \Gamma_{\cap n}^{TM}\hat{\mathbf{v}}(k_{zn})e^{jk_{zn}(z-z_n)}\right]\left[\hat{\mathbf{v}}(-k_{zn})e^{jk_{zn}(z'-z_n)} + \Gamma_{\cup n}^{TM}\hat{\mathbf{v}}(k_{zn})e^{jk_{zn}(2d_n-z'+z_n)}\right]}{k_{zn}\left(1-\Gamma_{\cup n}^{TM}\Gamma_{\cap n}^{TM}e^{2jk_{zn}d_n}\right)} \tag{4.3b}$$

and

$$\hat{\mathbf{h}}(\pm k_z) = \frac{\hat{\mathbf{x}}k_y \pm \hat{\mathbf{y}}k_x}{k_s} \qquad \hat{\mathbf{v}}(\pm k_z) = \mp\frac{k_z\mathbf{k}_s}{kk_s} + \hat{\mathbf{z}}\frac{k_s}{k} \tag{4.4}$$

where $k_s = |\mathbf{k}_s|$ and $k_{zn} = k_n^2 - k_s^2$ with $\mathrm{Im}(k_{zn}) \geq 0$. $\Gamma_{\cup n}^{TM}$ and $\Gamma_{\cup n}^{TE}$ are the reflection coefficients of TM and the TE modes at the upper boundary of layer (n), while $\Gamma_{\cap n}^{TM}$ and $\Gamma_{\cap n}^{TE}$ are the reflection coefficients of TM and the TE modes at the lower boundary of layer (n). These coefficients can be obtained through (2.43).

Substituting the DGF in (4.2) into (4.1), we obtain

$$\mathbf{E}(\mathbf{r}) + \frac{\delta\varepsilon(\boldsymbol{\rho})}{\varepsilon_n}\hat{\mathbf{z}}E_z(\mathbf{r}) = \frac{j\omega^2\mu_0}{8\pi^2}\iiint_V dV' \cdot\int\int_{-\infty}^{\infty} d\mathbf{k}_s e^{j\mathbf{k}_s\cdot(\mathbf{r}_s-\mathbf{r}_s')}\delta\varepsilon(\boldsymbol{\rho}')\bar{\bar{\mathbf{G}}}_p(\mathbf{k}_s, z, z')\cdot\mathbf{E}(\mathbf{r}') \tag{4.5}$$

where the source dyadic contribution has been collected to be the second term on the left hand side. If the observation point is outside of the source region, this term vanishes automatically.

We assume that the p$^{\text{th}}$ eigenmode can be represented by $\mathbf{E}_p(\boldsymbol{\rho})e^{j\beta x}$, where β is the propagation constant along the x direction. Equation (4.5) can thus be reduced to

$$\mathbf{E}_p(\boldsymbol{\rho}) + \frac{\delta\varepsilon(\boldsymbol{\rho})}{\varepsilon_n}\hat{\mathbf{z}}E_{pz}(\boldsymbol{\rho}) = \frac{j\omega^2\mu_0}{4\pi}\iint_S d\boldsymbol{\rho}'\delta\varepsilon(\boldsymbol{\rho}') \cdot\int_{-\infty}^{\infty} dk_y e^{jk_y(y-y')}\bar{\bar{\mathbf{G}}}_p(\beta, k_y, z, z')\cdot\mathbf{E}_p(\boldsymbol{\rho}') \tag{4.6}$$

where S is the cross section of the guiding regions.

Consider several dielectric strips embedded in the layer (n), the coupled integral equation can be written as

$$\mathbf{E}_p(\boldsymbol{\rho})+\frac{\delta\varepsilon(\boldsymbol{\rho})}{\varepsilon_n}\hat{\mathbf{z}}E_{pz}(\boldsymbol{\rho}) = \frac{j\omega^2\mu_0}{4\pi}\sum_{l=1}^{L}\iint_{S_l} d\boldsymbol{\rho}'\delta\varepsilon(\boldsymbol{\rho}')\int_{-\infty}^{\infty} dk_y e^{jk_y(y-y')}\tilde{\tilde{\mathbf{G}}}_p(\beta,k_y,z,z')\cdot\mathbf{E}_p(\boldsymbol{\rho}') \qquad \boldsymbol{\rho} \text{ on } S_l \quad (4.7)$$

where S_l is the cross section of the ℓ^{th} dielectric strip. The source dyadic contribution has been collected as the second term on the left-hand side of (4.7). The ℓ^{th} integral represents the contribution by the equivalent polarization current in the ℓ^{th} dielectric strip.

The integral equations (4.6) and (4.7) can be solved with MoM described in section 2.3. By using appropriate basis functions, a matrix can be obtained and the eigenvalue β can be obtained by setting the determinant of the matrix to be zero.

4.2.2 **EFIE solution to the propagation constants of modified NRD-guides**

Apparently, the guided wave properties of the modified NRD guides in section 1.2.2 are governed by the EFIEs (4.6), (4.7) with a specific DGF. Generally, there are two aspects of modification from the standard NRD-guide which includes the layers coated inside the metal plates and the shape of the cross section of the dielectric strip. Fig. 4.2 shows the cross section of a general modified NRD-guide in which an arbitrarily shaped high-dielectric strip is sandwiched between low-dielectric overlays on conducting plates.

The DGF for a general modified NRD-guide can be obtained in (4.3) by getting the reflecting coefficients at up and lower surfaces as

$$\Gamma^{\alpha}_{\cup 2}=\frac{\Gamma^{\alpha}_{21}-e^{-2jk_{z1}d_1}}{1-\Gamma^{\alpha}_{21}e^{-2jk_{z1}d_1}}, \quad \alpha=(TE,TM) \qquad (4.8a)$$

$$\Gamma^{\alpha}_{\cap 2}=\frac{\Gamma^{\alpha}_{23}-e^{2jk_{z3}d_3}}{1-\Gamma^{\alpha}_{23}e^{2jk_{z3}d_3}}, \quad \alpha=(TE,TM) \qquad (4.8b)$$

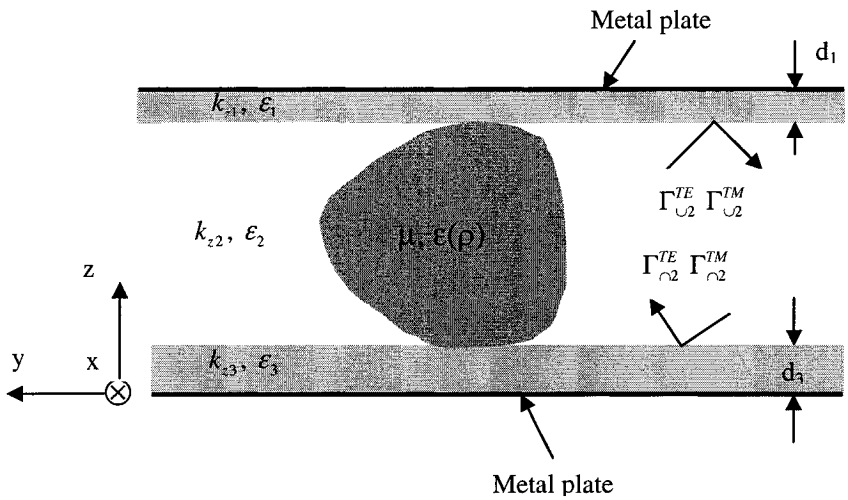

Fig. 4.2. The cross-section of a general modified NRD-guide.

In (4.8), the reflecting coefficients of both TM and TE mode being -1 are used. Γ^{α}_{21} and Γ^{α}_{23} are the Fresnel reflection coefficients of the α mode across the interfaces at $z=z_1$ and $z=z_2$, respectively. The explicit forms are

$$\Gamma^{TE}_{21(3)} = \frac{k_{z2} - k_{z1(3)}}{k_{z2} + k_{z1(3)}} \qquad \Gamma^{TM}_{21(3)} = \frac{\varepsilon_{1(3)} k_{z2} - \varepsilon_2 k_{z1(3)}}{\varepsilon_{1(3)} k_{z2} + \varepsilon_2 k_{z1(3)}} \tag{4.9}$$

where $k^e_{zn} = k^h_{zn} = k_{zn} = \sqrt{k_n^2 - k_\rho^2}$.

For practical applications, the cross section of the dielectric strips can be assumed to have a rectangular shape or can be divided into several sub-domains with rectangular shapes. For a single dielectric strip of width w and thickness d, we divide the cross section S into N by M cells of equal area. The length of each cell is $D_y=w/N$ along the y direction, and $D_z=d/M$ along with z direction. The center coordinate of the (n,m) cell, S_{nm}, is denoted by (y_n, z_m) with $1 \le n \le N$ and $1 \le m \le M$. The electric field of the pth eigenmode on the cross section S can thus be represented by a set of pulse basis functions as

$$\mathbf{E}_p(\boldsymbol{\rho}) = \sum_{\eta=x,y,z} \sum_{n=1}^{N} \sum_{m=1}^{M} a_{nm}^{\eta} \hat{\boldsymbol{\eta}} P_n(y) R_m(z) \tag{4.10}$$

where

$$P_n(y) = \begin{cases} 1, & y_n - D_y/2 \le y \le y_n + D_y/2 \\ 0, & elsewhere \end{cases}$$

$$R_m(z) = \begin{cases} 1, & z_m - D_z/2 \le z \le z_m + D_z/2 \\ 0, & elsewhere \end{cases} \tag{4.11}$$

Substituting (4.10) into (4.5), we have

$$\begin{aligned} &\sum_{\eta=x,y,z} \sum_{n=1}^{N} \sum_{m=1}^{M} a_{nm}^{\eta} \hat{\boldsymbol{\eta}} P_n(y) R_m(z) \left[1 + \frac{\varepsilon_{nm} - \varepsilon_2}{\varepsilon_2} \delta_{\eta z} \right] \\ &= \frac{j}{4\pi} \omega^2 \mu_0 \sum_{\eta=x,y,z} \sum_{n=1}^{N} \sum_{m=1}^{M} a_{nm}^{\eta} (\varepsilon_{nm} - \varepsilon_2) \cdot \iint_{S_{nm}} d\rho' P_n(y') R_m(z') \\ &\quad \cdot \int_{-\infty}^{\infty} dk_y e^{jk_y(y-y')} \tilde{\tilde{\mathbf{G}}}(\beta, k_y, z, z') \cdot \hat{\boldsymbol{\eta}}, \qquad \rho \quad on \quad S \end{aligned} \tag{4.12}$$

where $\delta_{\kappa\eta}$ is the Kronecker delta function, which is equal to 1 when $\kappa=\eta$ and is equal to 0 when $\kappa\neq\eta$, and ε_{nm} is the dielectric constant evaluated at (y_n, z_m).

Next, we choose the same set of basis functions as the testing functions and apply Galerkin's method to (4.12). Taking the inner product of $\hat{\boldsymbol{\kappa}} P_r(y) R_q(z)$ with (4.12), we obtain

$$\begin{aligned} &\pi j \omega^2 \mu_0 \sum_{\eta=x,y,z} \sum_{n=1}^{N} \sum_{m=1}^{M} a_{nm}^{\eta} (\varepsilon_{nm} - \varepsilon_2) \cdot \int_{-\infty}^{\infty} dk_y e^{jk_y(y_r - y_n)} \tilde{P}_r(-k_y) \tilde{P}_n(k_y) \tilde{g}_{\kappa\eta}^{qm}(\beta, k_y) \\ &= A_{rq} \left[1 + \frac{\varepsilon_{rq} - \varepsilon_2}{\varepsilon_2} \delta_{\kappa z} \right] a_{rq}^{\kappa} \end{aligned} \tag{4.13}$$

Here κ=x,y,z; $1\le r\le N$ and $1\le q\le M$; A_{rq} is the area of S_{rq}; $\tilde{P}_n(k_y)$ is the Fourier transform of $P_n(y)$ with

$$\tilde{P}_n(k_y) = \frac{1}{2\pi} \int_{-D_y/2}^{D_y/2} e^{-jk_y y} P_n(y) dy = \frac{\sin(k_y D_y/2)}{\pi k_y} \tag{4.14}$$

and $\tilde{g}_{\kappa\eta}^{qm}(\beta, k_y)$ is the $\kappa\eta$ component of the dyadic $\tilde{\mathbf{g}}^{qm}(\beta, k_y)$ with

$$\tilde{\mathbf{g}}^{qm}(\beta,k_y)=\int_{l_q} dz R_q(z)\int_{l_m} dz' R_m(z')\tilde{\mathbf{G}}(\beta,k_y,z,z') \tag{4.15}$$

where l_q is the domain of $R_q(z)$.

By utilizing the symmetry properties of $\tilde{P}_n(k_y)$ and $\tilde{g}_{\kappa\eta}^{qm}(\beta,k_y)$ with respect to k_y, (4.13) can be further reduced to

$$\begin{aligned} &2\pi j\omega^2\mu_0 \sum_{\eta=x,y,z}\sum_{n=1}^{N}\sum_{m=1}^{M} a_{nm}^{\eta}(\varepsilon_{nm}-\varepsilon_2)\cdot\int_0^{\infty} dk_y \tilde{P}_r(k_y)\tilde{P}_n(k_y)W_{rq,nm}^{\kappa\eta}(\beta,k_y) \\ &= \sum_{\eta=x,y,z}\sum_{n=1}^{N}\sum_{m=1}^{M}\delta_{\kappa\eta}\delta_{rn}\delta_{qm}A_{nm}\left[1+\frac{\varepsilon_{nm}-\varepsilon_2}{\varepsilon_2}\delta_{\eta z}\right]a_{nm}^{\eta} \end{aligned} \tag{4.16}$$

where

$$W_{rq,nm}^{\kappa\eta}(\beta,k_y)=\begin{cases} \cos k_y(y_r-y_n)\hat{g}_{\kappa\eta}^{qm}(\beta,k_y), \\ (\kappa,\eta)=(x,x),(x,z),(y,y),(z,x),(z,z) \\ j\sin k_y(y_r-y_n)\hat{g}_{\kappa\eta}^{qm}(\beta,k_y), \\ (\kappa,\eta)=(x,y),(y,x),(y,z),(z,y) \end{cases} \tag{4.17}$$

Equation (4.16) is a matrix equation of the form

$$\sum_{\eta=x,y,z}\sum_{n=1}^{N}\sum_{m=1}^{M} Z_{rq,nm}^{\eta}a_{nm}^{\eta}=0 \tag{4.18}$$

The propagation constants β can thus be obtained by setting the determinant of the Z matrix in (4.18) to zero. Hence we have

$$\det[Z(\omega,\beta)]=0 \tag{4.19}$$

4.2.3 The guidance and leakage properties of the modified NRD-guide

The solution of the β value in (4.19) can be either a real number for bounded modes, or complex number for leakage modes. Which mode will appear in a modified NRD-guide depends on the overlayers and the shape of the dielectric strip. Here, for simplicity, we will only discuss the case without overlayers (d_1=d_3=0). In this case, the Green's function can be reduced as:

$$\tilde{\tilde{\mathbf{G}}}(\beta,k_y,z,z')=\frac{1}{2\omega\varepsilon_s}\cdot\begin{bmatrix} j(k_s^2-\beta^2)g_1 & -j\beta k_y g_1 & \beta g_2 \\ -j\beta k_y g_1 & j(k_s^2-k_y^2)g_1 & k_y g_2 \\ -\beta g_3 & -k_y g_3 & j(\beta^2+k_y^2)g_4 \end{bmatrix} \tag{4.20}$$

where $g_1=\begin{cases}\sin(k_z z)\cdot\sin(k_z(z'-d_2))/(k_z\sin(k_z d_2)) & z<z' \\ \sin(k_z(z-d_2))\sin(k_z z')/(k_z\sin(k_z d_2)) & z>z'\end{cases}$,

$g_2=\begin{cases}\sin(k_z z)\cos(k_z(z'-d_2))/\sin(k_2 d_2) & z<z' \\ \sin(k_z(z-d_2))\cos(k_z z')/\sin(k_z d_2) & z>z'\end{cases}$,

$g_3=\begin{cases}\cos(k_z z)\sin(k_z(z'-d_2))/\sin(k_z d_2) & z<z' \\ \cos(k_z(z-d_2))\sin(k_z z')/\sin(k_z d_2) & z>z'\end{cases}$,

$g_4=\begin{cases}\cos(k_z z)\cos(k_z(z'-d_2))/(k_z\sin(k_z d_2)) & z<z' \\ \cos(k_z(z-d_2))\cos(k_z z')/(k_z\sin(k_z d_2)) & z>z'\end{cases}$,

and $k_z^2=k_s^2-\beta^2-k_y^2$.

As can be seen from (4.16), the terms in matrix are defined through infinite spectral integrals. The integrands $W_{rq,nm}^{\kappa\eta}$ in (4.16) may have a number of poles that are associated with the roots of the denominators. These poles correspond to the TM and TE modes supported by the two parallel metal plates. In the NRD-guide condition, only the fundamental parallel plate mode with propagation constant k_s can exist in the waveguide. Its associated poles k_{ys} in the complex k_y-plane are given by

$$k_z=0\Rightarrow k_{ys}^2=k_s^2-\beta^2\Rightarrow k_{ys}=\pm\sqrt{k_y^2-\beta^2} \tag{4.21}$$

The poles correspond to TEM mode and only appears in the $(\kappa,\eta)=(z,z)$ term in (4.20).

It is obvious from (4.11) that propagation constants β of the transmission line are real if $\beta>k_s$. Otherwise leakage may occur, resulting in complex wave numbers β with negative imaginary parts. More rigorously, a transmission line mode is leaky if the following conditions are satisfied

$$\mathrm{Re}(k_{ys}^2)>0,\quad \mathrm{Im}(k_{ys}^2\geq 0) \tag{4.22}$$

The symbol of '=' in the last inequality defines the point where leakage effects turn on. This can be seen as the crossing of the real k_y axis by the poles k_{ys}. In this case, the integration path must be deformed in the complex k_y-plane in order to circumvent the radiation wave poles as in Fig. 4.3.

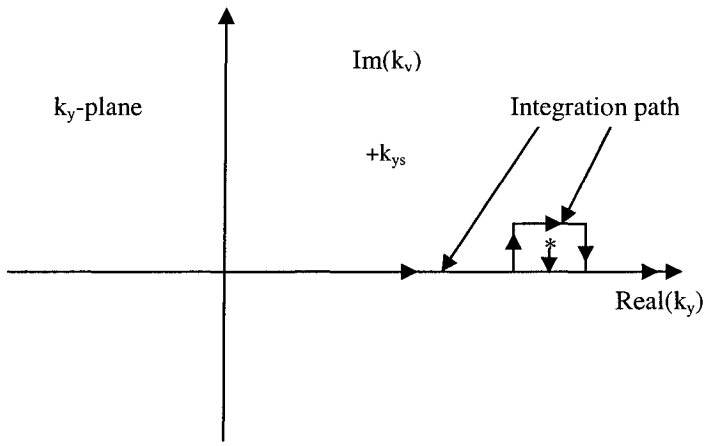

Fig. 4.3. Integration contour in the complex $\pm k_y$-plane and migration path from leaky to bound regimes of the poles k_{ys}.

Another method to avoid numerical difficulties in the poles is to extract the poles with the residue theory. The integration from $k_{y0}-\delta$ to $k_{y0}+\delta$, where $\delta \cong 0.001 k_{y0}$, is carried out analytically as

$$I_\delta = \int_{k_{x0}-\delta}^{k_{x0}+\delta} \frac{f(k_x)}{T_{em}(k_x)} dk_x = \frac{jf(k_{y0}-j\gamma)}{T_{em}'(k_{y0}-j\gamma)} \tan^{-1} \frac{-2\delta\gamma}{\gamma^2-\delta^2} \tag{4.23}$$

where $T_{em}(k_y)$ has a pole at $k_y=k_{y0}-j\gamma$. $f(k_y)$ represents the remaining nonsingular portion of the integrand. For the guidance case $\gamma=0$, I_δ can be obtained as

$$I_\delta = \frac{-j\pi f(k_{y0})}{T_{em}'(k_{y0})} \tag{4.24}$$

The residue value in (4.23) has been proved to be independent of z. When the structure is symmetrical in vertical direction (z), the poles contribution to the integration from the

upper half region is opposite to that from the lower half region. So they will cancel out each other in the final element expressions at last and no leakage occurs in this vertical symmetric structure. For example, the standard NRD-guide and the proposed bridged NRD-guide coupler in the next section have no leakage because of the vertical symmetric property of the structures. The NRD-guide with a gap [30], and the NRD-guide with trapezoidal cross-section [81] have leakage because the vertical symmetry disappears in these structures.

4.2.4 Asymptotic technique in the numerical integration

The integral in (4.16) can be evaluated numerically by restricting the unbounded integration interval [0,∞] to the finite region [0, K_y], where K_y is a sufficiently large number. The integrands $\tilde{P}_r(k_y)\tilde{P}_n(k_y)W^{\kappa\eta}_{rq,nm}(\beta,k_y)$ exhibit a rapidly oscillating behavior, whose amplitude decreases as $1/k_y^{\nu}$. For the integer number ν it is found that ν≥2, and thus the convergence of the integrals is ensured. The weakest convergence, ν=2, occurs at $z_q=z_m$, which only appears in the second term (k_y^2 term) at (κ, η) = (y, y), (z, z) case. At this point, it would be beneficial to search for the asymptotic behavior of the integrands prior to performing the numerical computations. So, we can represent the integral as

$$V_{nm}=\int_0^{K_y}\tilde{P}_r(k_y)\cdot\tilde{P}_n(k_y)\left(W^{\kappa\eta}_{rq,nm}-W^{\kappa\eta\ A}_{rq,nm}\right)dk_y+\int_0^{\infty}\tilde{P}_r(k_y)\cdot\tilde{P}_n(k_y)W^{\kappa\eta\ A}_{rq,nm}\,dk_y \qquad (4.25)$$

The $W^{\kappa\eta\ A}_{rq,nm}$ are asymptotic representations of $W^{\kappa\eta}_{rq,nm}$, which is obtained for $k_y>>k_0$. Thus the first integral in (4.25) becomes well suited for numerical integration due to the quickly decaying integrand. The second integral in (4.25) can be carried out analytically.

In order to demonstrate the applicability of the asymptotic extraction technique, as well as its numerical efficiency, we give an example concerning the behavior of integrands in the case of standard NRD-guide in which r=1 and n=5, q=m=1.(N=M=10).

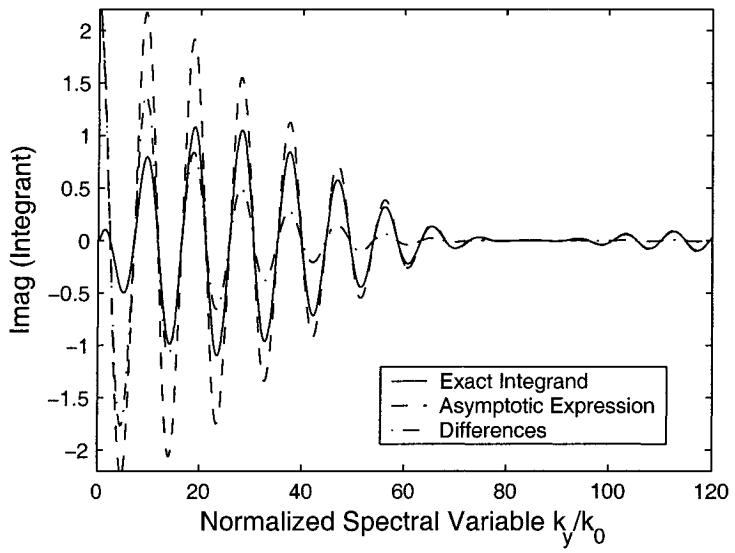

Fig. 4.4. Plots of the real parts of the integrand, its asymptotic expression and their difference versus the normalized spectral variable k_y.

Fig. 4.4 plots the real part of the primary integrand of (4.16) for (κ, η) = (y, y) varying with the normalized k_y. The dominant asymptotic expression of (4.25) is also depicted and it is clear that $W_{rq,nm}^{\kappa\eta\ A}$ very closely approximates the exact function $W_{rq,nm}^{\kappa\eta}$ as $k_y/k_0>60$. Consequently, it is anticipated that their difference would be a strongly convergent integral. The remaining integrands decrease faster than $1/k_y^3$ and their numerical integrations need no special treatment.

4.2.5 An example-NRD-guide with air gap

To demonstrate the efficiency of the proposed method, the guidance and leakage properties of NRD-guide with air gap as shown in Fig. 1.1 (d) is calculated in this section. This structure was first proposed and modeled with mode-matching method in [30]. The presence of the gap may introduce several effects in the guided wave properties. First, there is a small shift in the phase constant β. The effect of the gap is to

speed up the wave since more of the wave is now in the air region. The values of β/k_0 are therefore lowered somewhat by the air gap. Second, leakage is produced in the form of a TEM wave that propagates away at an angle from the dielectric strip on both sides. The presence of the gap breaks the vertical symmetry of the NRD-guide. As a result, a net vertical electric field is produced and leakage occurs in the form of a TEM wave in the parallel-plate's region. The leakage of energy makes the propagation constant complex, with an attenuation constant α being a measure of the leakage, and with a change $\Delta\beta$ in the phase constant.

The curves of β/k_0 and α/k_0 in Fig. 4.5 (a) and (b) are plotted as a function of b/λ_0, where b is the width of the dielectric strip, with the air gap thickness of t/λ_0 as a parameter. The results from mode-matching method are also plotted for comparison. In Fig. 4.5 (a), the β/k_0 with our method is a little up shift comparing with that in [30] with mode-matching method. Our results approach the analytical value of β/k_0 when t=0 more closely. The values of α/k_0 with our method agree very well with that in [30].

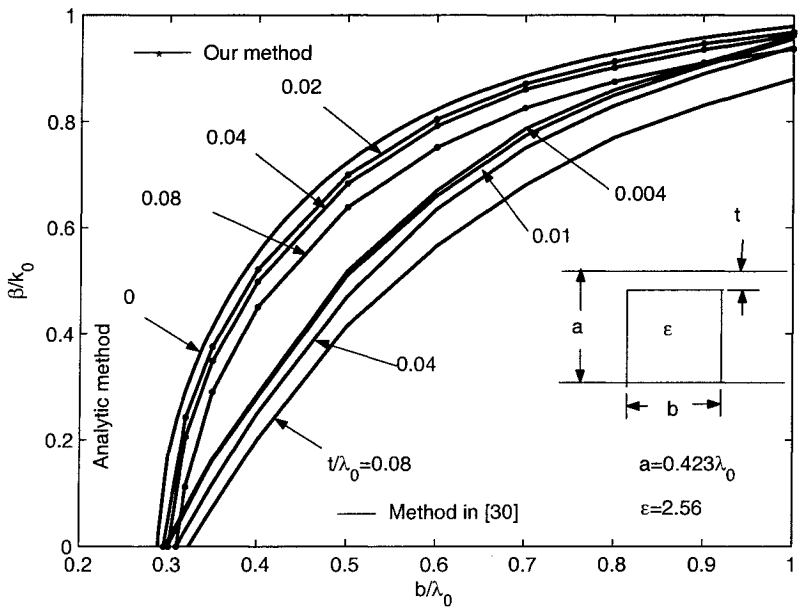

Fig. 4.5. Curves of β/k_0 as a function of b/λ_0, with t/λ_0 as a parameter. Quantities b and t are the dielectric strip width and air gap thickness, respectively, as shown in the inset.

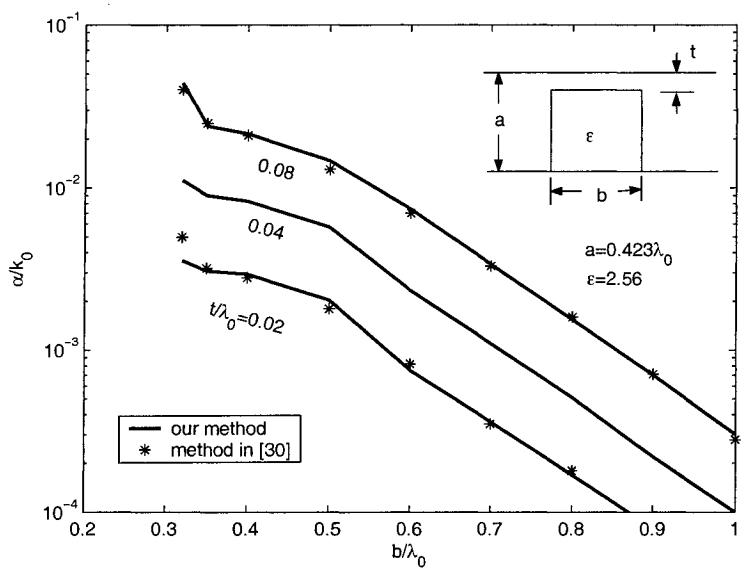

Fig. 4.6. Curves of α/k_0 as a function of b/λ_0, with t/λ_0 as a parameter. Quantities b and t are the dielectric strip width and air gap thickness, respectively, as shown in the inset.

4.3 Analysis and Design of Bridged NRD-Guide Coupler

In the NRD-guide circuits, the coupling mechanism of a conventional proximity coupler is due to the interaction of exponentially decaying fields between the two waveguides as in section 3.4. Hence, the coupling is sensitive to the spacing and the length of the coupler. The spacing for a strong coupler is not easily controlled in this kind of coupler design, making it very difficult to reproduce the coupler performances. The size is also large for this conventional coupler.

A new NRD-guide coupler is proposed in this section to overcome the drawbacks of the conventional coupler. In this structure, a thin dielectric strip is used to connect the coupled parallel NRD-guides to form a bridge between them as shown in Fig. 4.7. By optimizing the thickness of the bridge, the coupling coefficient is largely enhanced, which results in an extremely compact coupler compared to the conventional topology. The existence of such a bridge yields a monolithic structure. This makes it easy to control the spacing of the coupler and also makes the coupler performance reproducible.

The degree of coupling can be changed not only by controlling the spacing of coupled guides but also by adjusting the thickness of the bridge. Furthermore, this type of coupler is very broadband. A similar coupler was realized with image guide in [119]. However, the geometric connection is symmetric in our coupler design and the advantages can be maximized by optimizing the thickness of the bridge.

In this section, the EFIE solution to propagation constants of the structure is given in section 4.3.1. A bridged (or bridge-connected) NRD-guide 3dB directional coupler is designed in section 4.3.2 based on the guided wave properties. Experimental prototypes are fabricated and frequency dependent characteristics are measured and compared to those of the conventional parallel-line couplers in section 4.3.3.

4.3.1 Integral equation solution to the propagation constants of bridged NRD-guide coupler

The cross-section and top view of the proposed bridged NRD-guide coupler is shown in Fig. 4.7 with the coordinate system. In this section, we only consider the two-dimensional problem and assume that the whole structure is uniform along the propagation direction x. Assuming that the permittivity of the dielectric strips is $\varepsilon(\rho)$, the propagation constant of this structure is also governed by the integral equation (4.5) and the Green's functions for parallel metal plates in spectral domain is expressed in (4.20).

In several strips case as shown in Fig. 4.7(a), the strips are symmetrical in the y and z directions. For this symmetrical configuration, both the even and odd modes exist. We denote the even (odd) mode as a mode with E_y an even (odd) function, and H_x an odd (even) function of y. An electric (magnetic) wall can be put at y=0 and a magnetic wall can be put at z=0 without affecting the field distributions. So the coupled NRD guides can be divided into four regions I, II, III and IV according the electric and magnetic walls. Each region includes two sub-regions labeled as 1 and 2.

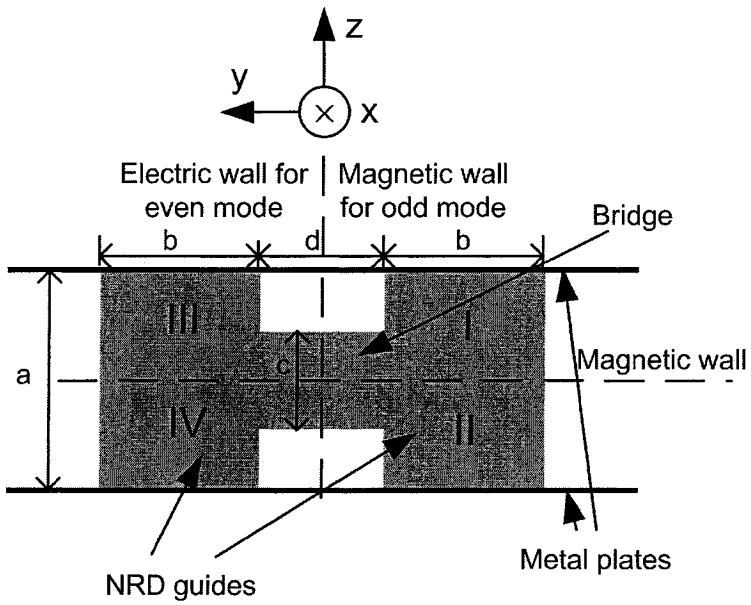

(a)

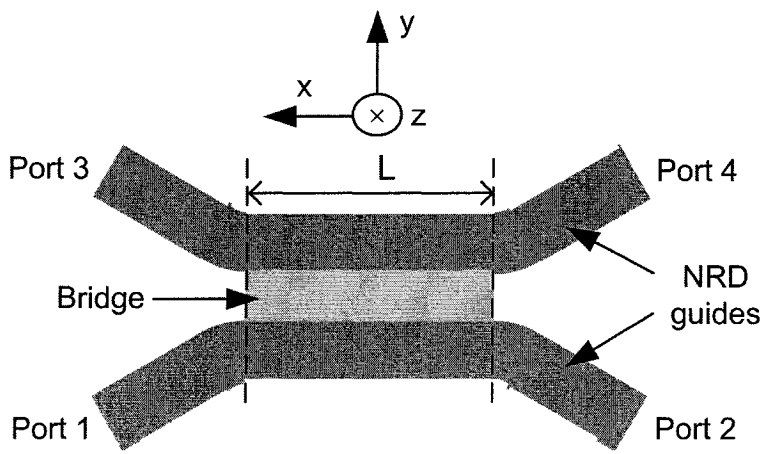

(b)

Fig. 4.7. (a) Cross-section of the bridge-connected (or bridged) NRD guides. (b) Bridged NRD-guide coupler

To solve the integral equation (4.5) for symmetrical dielectric strip waveguides, we choose two sets of pulse basis functions as in (4.11) to represent the electric field on the cross-section S_I as

$$\mathbf{E}_p(\boldsymbol{\rho})=\sum_{l=1}^{2}\sum_{\eta=x,y,z}\sum_{n=1}^{N}\sum_{m=1}^{M}a_{\ln m}^{\eta}\hat{\boldsymbol{\eta}}P_{\ln}(y)R_{lm}(z), \qquad \rho \quad on \quad S_I \tag{4.26}$$

By symmetry, the electric field on the cross section S_{II} ,S_{III} and S_{IV} can be represented as

$$\mathbf{E}_p(\boldsymbol{\rho})=\sum_{l=1}^{2}\sum_{\eta=x,y,z}\sum_{n=1}^{N}\sum_{m=1}^{M}I_{II\xi}^{\eta}a_{\ln m}^{\eta}\hat{\boldsymbol{\eta}}P_{\ln}(y)R_{lm}(-z), \qquad \rho \quad on \quad S_{II} \tag{4.27a}$$

$$\mathbf{E}_p(\boldsymbol{\rho})=\sum_{l=1}^{2}\sum_{\eta=x,y,z}\sum_{n=1}^{N}\sum_{m=1}^{M}I_{III\xi}^{\eta}a_{\ln m}^{\eta}\hat{\boldsymbol{\eta}}P_{\ln}(-y)R_{lm}(z), \qquad \rho \quad on \quad S_{III} \tag{4.27b}$$

$$\mathbf{E}_p(\boldsymbol{\rho})=\sum_{l=1}^{2}\sum_{\eta=x,y,z}\sum_{n=1}^{N}\sum_{m=1}^{M}I_{IV\xi}^{\eta}a_{\ln m}^{\eta}\hat{\boldsymbol{\eta}}P_{\ln}(-y)R_{lm}(-z), \qquad \rho \quad on \quad S_{IV} \tag{4.27c}$$

where the subscript ξ in I_{ξ}^{η} designates the even mode when ξ=e and the odd mode when ξ=o. The definition of I_{ξ}^{η} is

$$I_{II\xi}^{\eta}=\begin{cases}1, & (\xi,\eta)=(o,x),(e,y),(e,x),(e,y)\\ -1, & (\xi,\eta)=(e,z),(o,z)\end{cases} \tag{4.28a}$$

$$I_{III\xi}^{\eta}=\begin{cases}1, & (\xi,\eta)=(e,x),(o,y),(o,z)\\ -1, & (\xi,\eta)=(o,x),(e,y),(e,z)\end{cases} \tag{4.28b}$$

$$I_{IV\xi}^{\eta}=\begin{cases}1, & (\xi,\eta)=(e,x),(o,y),(e,z)\\ -1, & (\xi,\eta)=(o,x),(e,y),(o,z)\end{cases} \tag{4.28c}$$

Substituting (4.26) and (4.27) into (4.5) for ρ on S_1, we have

$$\begin{aligned}&\sum_{l=1}^{2}\sum_{\eta=x,y,z}\sum_{n=1}^{N}\sum_{m=1}^{M}a_{\ln m}^{\eta}\hat{\boldsymbol{\eta}}P_{\ln}(y)R_{lm}(z)\left[1+\frac{\varepsilon_{\ln m}-\varepsilon_l}{\varepsilon_l}\delta_{\eta z}\right]\\ &=\frac{j}{4\pi}\omega^2\mu_0\sum_{l=1}^{2}\sum_{\eta=x,y,z}\sum_{n=1}^{N}\sum_{m=1}^{M}a_{\ln m}^{\eta}(\varepsilon_{\ln m}-\varepsilon_l)\\ &\iint_{S_{nm}}d\rho'\left[P_{\ln}(y')R_{lm}(z')+I_{II\xi}^{\eta}P_{\ln}(y')R_{lm}(-z')+I_{III\xi}^{\eta}P_{\ln}(-y')R_{lm}(z')+I_{IV\xi}^{\eta}P_{\ln}(-y')R_{lm}(-z')\right]\\ &\cdot\int_{-\infty}^{\infty}dk_y e^{jk_y(y-y')}\tilde{\tilde{\mathbf{G}}}(\beta,k_y,z,z')\cdot\hat{\boldsymbol{\eta}}, \qquad \rho \quad on \quad S_I\end{aligned} \tag{4.29}$$

Due to the symmetry of the structure, only the electric fields on S_1 need to be tested when applying Galerkin's method. Taking the inner product of $\hat{\kappa}P_{l'r}(y)R_{l'q}(z)$ with (4.29) and utilizing the symmetry properties with respect to k_y, we have

$$\begin{aligned} &2\pi j\omega^2\mu_0\sum_{l=1}^{2}\sum_{\eta=x,y,z}\sum_{n=1}^{N}\sum_{m=1}^{M}a_{\ln m}^{\eta}(\varepsilon_{\ln m}-\varepsilon_l)\cdot\int_0^{\infty}dk_y\tilde{P}_r(k_y)\tilde{P}_n(k_y)W_{l'rq,\ln m}^{\kappa\eta(\xi)}(\beta,k_y) \\ &=\sum_{l=1}^{2}\sum_{\eta=x,y,z}\sum_{n=1}^{N}\sum_{m=1}^{M}a_{\ln m}^{\eta}\cdot\delta_{\kappa\eta}\delta_{lrn}\delta_{qlm}A_{\ln m}\left[1+\frac{\varepsilon_{\ln m}-\varepsilon_l}{\varepsilon_l}\delta_{\eta z}\right]a_{\ln m}^{\eta} \end{aligned} \tag{4.30}$$

where κ=x,y,z; $1\le r\le N$ and $1\le q\le M$; and

$$W_{rq,nm}^{\kappa\eta(\xi)}(\beta,k_y)=\begin{cases}\left[\cos k_y(y_r-y_n)+I_{III\xi}^{\eta}\cos k_y(y_r+y_n)\right]\hat{g}_{\kappa\eta}^{qm}(\beta,k_y) \\ +\left[I_{II\xi}^{\eta}\cos k_y(y_r-y_n)+I_{IV\xi}^{\eta}\cos k_y(y_r+y_n)\right]\hat{g}_{-\kappa\eta}^{qm}(\beta,k_y), \\ (\kappa,\eta)=(x,x),(x,z),(y,y),(z,x),(z,z) \\ j\left[\sin k_y(y_r-y_n)+I_{III\xi}^{\eta}\sin k_y(y_r+y_n)\right]\hat{g}_{\kappa\eta}^{qm}(\beta,k_y) \\ +\left[I_{II\xi}^{\eta}\sin k_y(y_r-y_n)+I_{IV\xi}^{\eta}\sin k_y(y_r+y_n)\right]\hat{g}_{-\kappa\eta}^{qm}(\beta,k_y), \\ (\kappa,\eta)=(x,y),(y,x),(y,z),(z,y)\end{cases} \tag{4.31}$$

where $g_{-}^{qm}(k_x,\eta)=\int_{l_q}dzR_q(z)\int_{l_m}dz'R_m(-z')g(\beta,k_y,z,z')$

Equation (4.30) is a matrix equation, and the eigenvalue β can be obtained by setting the determinant of the matrix to zero. Due to the vertical symmetrical properties, the solution of the propagation constant is a real number. Therefore no leakage mode exists in this structure.

4.3.2 The design rules of the bridged NRD-guide coupler

Using the above method, the propagation constants of the even (β_e) and odd (β_o) modes of the bridged NRD guides can be calculated. In this symmetric structure, the low-loss LSM mode fields may be considered as a superposition of even and odd modes propagating longitudinally with different propagation constants β_e and β_o, respectively. Assuming that the coupled NRD guides are lossless and matched at all ports, the

coupling coefficient is defined in (3.28) and the coupling length for a 3-dB directional coupler is

$$L_{3dB} = \frac{\pi}{2(\beta_e - \beta_o)} \tag{4.32}$$

Then, the scattering coefficients for the coupler are expressed as follows:

$$|S_{21}| = \left|\cos\frac{\beta_e - \beta_o}{2} l_{eff}\right| \tag{4.33}$$

$$|S_{41}| = \left|\sin\frac{\beta_e - \beta_o}{2} l_{eff}\right| \tag{4.34}$$

where l_{eff} is the effective coupling length of a coupler.

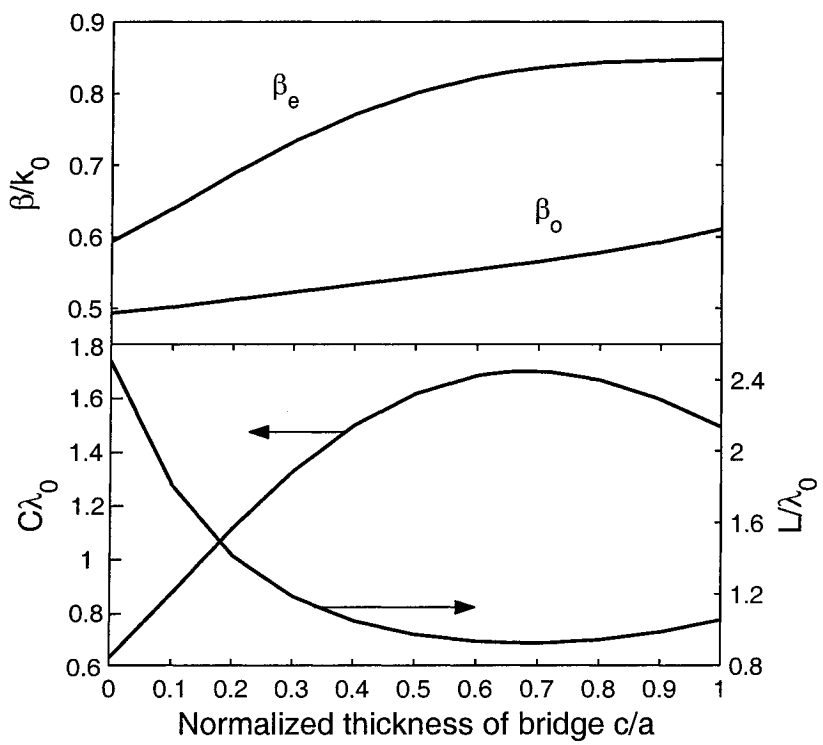

Fig. 4.8. Propagation constants, coupling coefficient and coupling length for the proposed bridged NRD-guides (a=1.78mm, b=1.85mm, d=1.27mm, f=77GHz and ε_r=2.04).

Fig. 4.8 shows the propagation constants β_e, β_o, the normalized coupling coefficient $C\lambda_0$ and normalized 3dB coupling length L/λ_0 as a function of the thickness of the bridge, which is also normalized with respect to the plate separation (c/a). A very interesting point in this figure is that the coupling coefficient C becomes maximum at c/a=0.68. At this point, the coupling length can be reduced by 60% compared to the conventional coupler (c/a=0). In the view of propagation constants, the increase of β_e is larger than the increase of β_o in the region of c/a<0.68 and less than the increase of β_o in the region of c/a>0.68 as the thickness of the bridge increases. This leads to the maximum point of the coupling coefficient C at c/a=0.68.

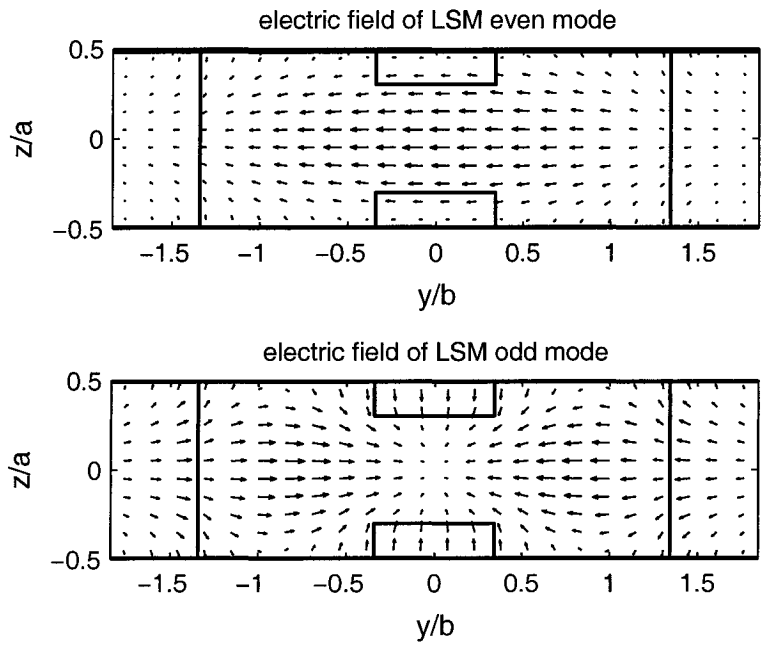

Fig. 4.9. Field distribution of even and odd modes for the bridged-guides at c/a=0.68 (a=1.78mm, b=1.85mm, d=1.27mm, f=77GHz and εr=2.04).

The phenomenon that the coupling coefficient does not increase (near-) linearly as c/a increases can be explained from the field distribution of the even and odd modes as shown in Fig. 4.9. In the dielectric waveguide, the propagation constant increases as

more fields are confined within the dielectric strips. As shown in Fig. 4.9, the fields in the middle of bridge change approximately as a function of cosine for the even mode and sine for the odd mode in z-direction. The increase rate of the fields confined in the dielectric strip for the even mode is larger than its odd mode counterpart as c/a increases from 0 to 0.68. So the increasing of β_e is larger than the increasing of β_o, which leads to a larger coupling coefficient C. However, this is just the opposite case as c/a increases from 0.68 to 1. Therefore, the coupling coefficient C is reduced in this case.

Fig. 4.10 shows the dispersion curves as c/a are equal to 0, 0.68 and 1, respectively, while other parameters are identical to those of Fig. 4.8. The results indicate that the second even mode may appear inside the operating bandwidth of the lowest even and odd modes of the coupled NRD-guides. So for the bridged directional NRD-guide coupler, the operational bandwidth of only the low order modes is reduced as the ratio c/a increase. This is an important factor in designing such couplers when a large single-mode band is required.

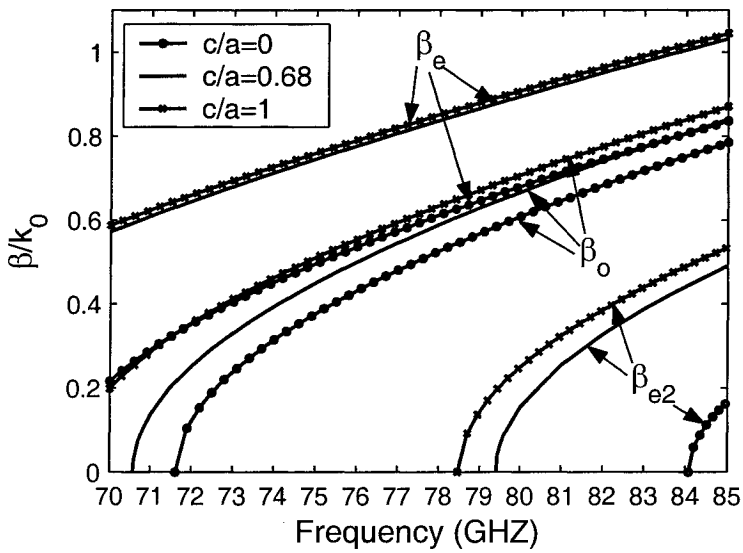

Fig. 4.10. Dispersion curves of the bridged NRD guides as c/a is 0, 0.68 and 1, respectively (a=1.78, b=1.85, d=1.27mm and ε_r=2.04).

Fig. 4.11 shows the scattering parameters for the coupler at a center frequency of 77GHz with the same dimensions as in Fig.4.10. These results suggest that the bandwidth of bridged NRD-guide coupler with c/a=0.68 extends to 3.6% for a tolerance limitation of ±0.5dB of deviation in coupling from 3dB, while that of the coupler with c/a=1 is 4.2%. On the other hand, the coupler with c/a=0 has a bandwidth of only 1.8%. Therefore, the higher the value of c/a takes, the broader the bandwidth. However, higher-order modes may propagate within the operating bandwidth if c/a is too high, as indicated by the results of Fig. 4.10 for a center frequency of 77GHz. Considering the coupling length, bandwidth and the single mode operation band altogether, the optimum value of c/a is around 0.4-0.68. The thin bridge also helps reduce the reflection at the junctions between the feeding arms of the coupler and the bridged coupled-line section.

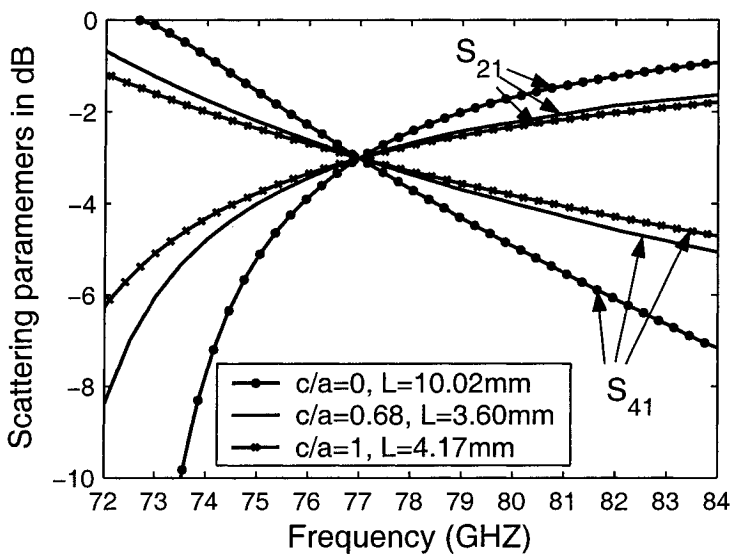

Fig. 4.11. Calculated frequency characteristics of the bridged NRD-guide 3dB coupler with c/a=0 (the conventional coupler), c/a=0.68 and c/a=1(a=1.78, b=1.85, d=1.27mm and εr=2.04).

4.3.3 Experimental verification of the designed NRD-guide couplers

Based on the above analysis, a bridged NRD-guide 3dB directional coupler is designed and fabricated with c/a=0.5. At this point, the single mode operation region is extended beyond 77GHz while the bandwidth and the coupling length suffers little sacrifice compared to the optimized point c/a=0.68. To illustrate the advantages of the new coupler, we have also fabricated a conventional coupler. Both couplers were fabricated of Teflon with $\varepsilon_r = 2.04$. Both couplers have a=1.78, b=1.85, and d=1.27 mm.

In practice, the design of a parallel guide coupler should incorporate bend sections on either side of the parallel-coupled section in order to achieve decoupling of the four ports. Generally, symmetric straight bends or symmetric curved bends are used. However, the bends in NRD-guide suffer serious mode conversion problem [34]. To avoid this problem, two 90° elbow bends are used for the arms as illustrated in Fig. 4.12. In this configuration, the input operating LSM_{11} mode is converted to LSE_{11} mode at the first elbow. Then the LSE_{11} mode is converted back to LSM_{11} mode at the second elbow. The mode conversion at this type of elbow is almost complete [41]. This inefficiency of the mode conversion causes resonance problem in the circuit when waveguide-to-NRD-guide transitions are added to the coupler for measurement purpose [35] because the LSE_{11} mode is blocked by the transitions. To eliminate the resonance problem, LSE_{11} mode-based microstrip line to NRD guide transitions are added before each waveguide transitions [68], and absorbing materials are placed on each microstrip lines. The dielectric substrate used in the realization of these LSE_{11} mode loads is the Duroid/RT6002 from Rogers Corp. The loss level added by these LSE_{11} mode loads is equal to the amount of power coupled to the LSE_{11} mode in the coupler circuit, which is less then 0.25dB.

Another problem caused by the elbows is the non-uniformly coupled regions at the beginning and the end of the coupling section. This parasitic coupling effect must be taken into account in determining the overall coupling. So the overall length of the coupling section is reduced so to obtain the desired coupling level. Furthermore, a direct connection of the elbows with the bridged coupler section produces a high reflection

problem. To reduce the reflection level, the bridge-connected coupler section is terminated at both ends by tapered half-circle sections. Based on the above effects, the length of the straight coupled section is reduced from 3.63 mm to 3.42 mm in the design of the bridged coupler and from 10.02 mm to 7.87 mm in the design of the conventional coupler.

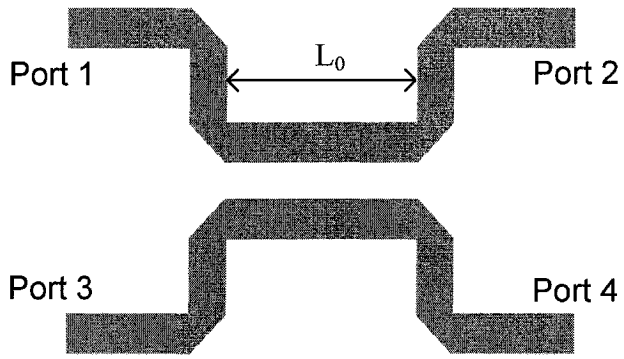

(a)

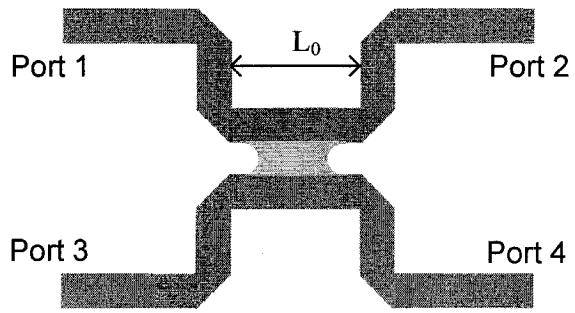

(b)

Fig. 4.12. Configurations of the bridged NRD-guide coupler and the conventional NRD-guide coupler with the 90° elbow arms

Finally, a calibration procedure is used to remove the effects of the mismatch between the NRD-guide and rectangular waveguide in measured results. In this procedure, two NRD guides of different length are measured. Then S-parameters of the transition of

NRD-guide to waveguide are obtained. The pure S-parameters of the couplers can be obtained by calibrating the measured S-parameters of the couplers with the S-parameters of the transition. In Fig. 4.13, photographs of the fabricated directional couplers and NRD-guides for calibration are shown.

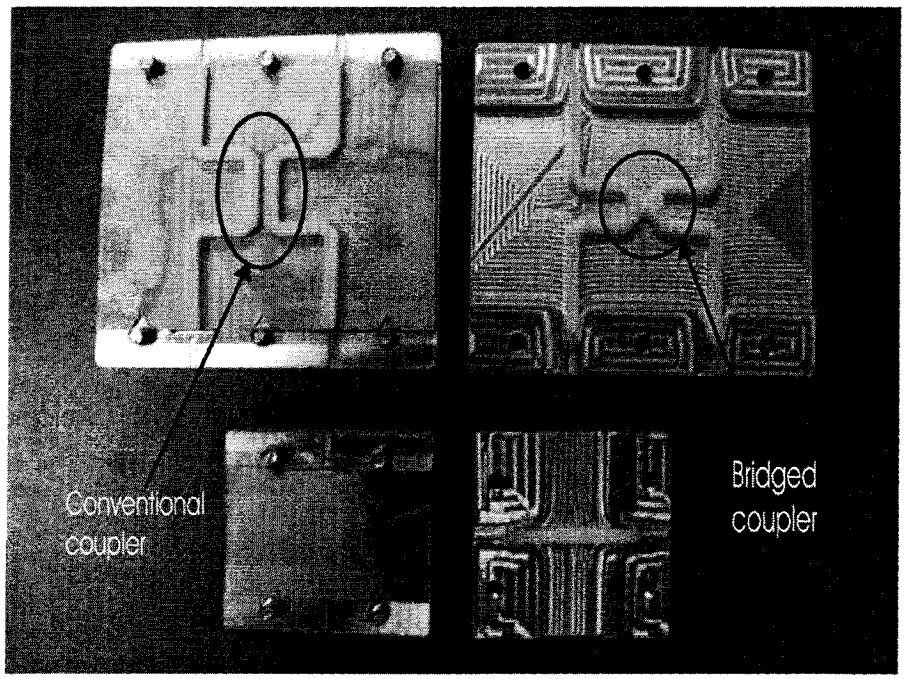

Fig. 4.13. Photographs of the Teflon NRD-guide coupler and transmission line prototype with back-to-back rectangular waveguide transitions.

Fig.4.14 shows measured results for the bridged NRD-guide coupler and its conventional counterpart while its theoretical results are also presented for comparison. It can be seen that the bandwidth of the bridged coupler is broader while its coupling length is shorter than the conventional one. Compared to the conventional coupler, the return loss of the bridged coupler is a little bit high in the high frequency region. The isolation level is lower (S_{31} is higher) for the bridged coupler than for the conventional coupler because of the mismatch between the arms and the center bridge-connected coupling section. The mismatch may be reduced by optimizing the shape of taper in the

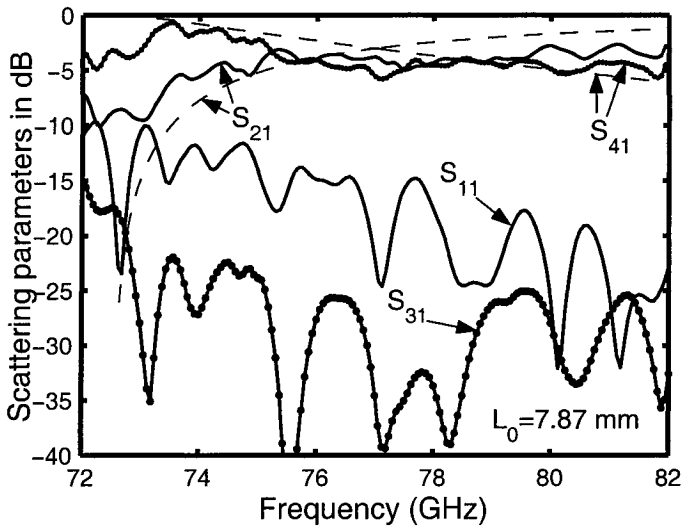

(a)

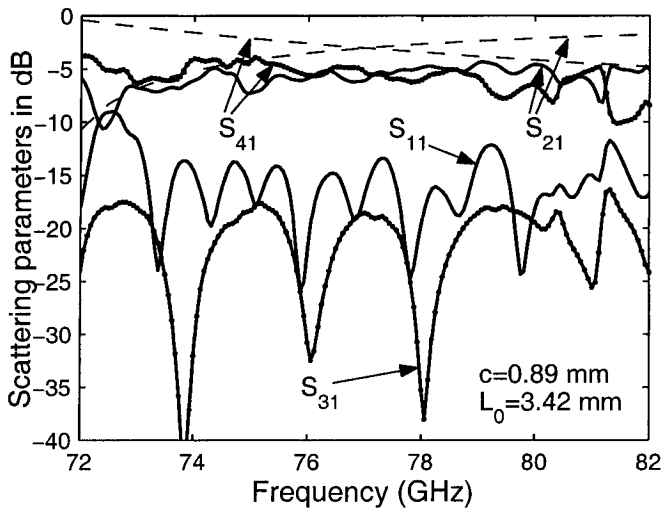

(b)

Fig.4.14. Measured and calculated (dashed lines) frequency characteristics for (a) the conventional NRD-guide coupler and (b) the bridged NRD-guide coupler. (a=1.78, b=1.85, d=1.27 mm and εr=2.04)

junction between the arms and coupling section. The overall insertion loss of the bridged NRD-guide couplers is about -1.5 dB, the same level as in the case of the conventional coupler. This loss level is equivalent to the insertion loss of a straight NRD-guide with a length equal to the total length of the coupler. The reason why the characteristics of the calculated frequency response only vaguely resemble the measured performance is because the calculated results do not include the transition effect between the arms and coupling section as well as inherent loss mechanism of the coupler.

4.4 Summary

This chapter has presented an integral equation solution to the guided wave properties of modified NRD-guides. The electric field integral equation was formulated for dielectric waveguides in multilayered media and the solution to the propagation constants of a general modified NRD-guide was obtained through the Garlerkin's MoM. The condition of bounded mode and leakage mode has been discussed and an asymptotic technique in the numerical integration was presented. A bridged NRD-guide coupler was proposed and the propagation constants and electrical characteristics have been obtained with the EFIE method. Compared to the conventional NRD guide coupler, the bridged NRD-guide coupler is much more compact and broadband, which are critical for millimeter-wave integrated circuits. Furthermore, the bridged NRD-guide directional couplers are able to improve mechanical stability and make electrical performances reproducible. The experimental results have confirmed the analysis and they have shown that this type of coupler is useful in millimeter-wave systems.

CHAPTER 5

AN ORDER-REDUCED VOLUME-INTEGRAL EQUATION APPROACH FOR ANALYSIS OF NRD-GUIDE AND H-GUIDE MILLIMETER-WAVE CIRCUITS

5.1 Introduction

The EFIE method was used to obtain the guided wave properties of modified NRD-guides in chapter 4. However, when this method is extended to three dimensional cases, referred to as volume integral-equation method, only a few simple problems with finite dielectric regions can be solved because of large memory and CPU time requirements [95], [96]. In this chapter, a special integral equation technique which can reduce the original 3-D problems to 2-D planar problems will be developed for modeling of NRD-guide discontinuities and components as discussed in section 1.2.3.

In the NRD-guide and H-guide structures, a half-sinusoidal vertical (z) variation of fields remains unchanged all over the circuit with the LSM_{11} or LSE_{11} mode excitation due to the vertical symmetry. Therefore, the current discretization in the volume integral equation can be implemented in the x-y plane just as in planar circuits. With such basis functions, the vertical integration in space-domain can be obtained analytically and an m=1 first-order Green's function can be constructed. So the element integrations are carried out in two dimensions in spectral domain. At last, the solution of NRD-guide and H-guide circuits are reduced to a 2-D planar problem. Therefore, this method is called order-reduced volume integral equation (ORVIE) approach. This technique largely reduces calculation effort and makes it possible to simulate NRD-guide circuits of any shaped planar-section and any varied dielectric permittivity in the planar section. In particular, it can accurately calculate radiation loss along bends and discontinuities of H-guide by extracting poles in the Green's function.

In the next section, the principle of the ORVEI technique is presented in detail. Then several examples including NRD-guide, H-guide open-ends, resonators, notched square

and rectangular sections with inhomogeneous dielectric variation, and 3-pole gap-coupled NRD filter are modeled to demonstrate the accurate and efficiency of the approach. Finally, a short summary is given in section 5.4.

5.2 Order Reduced Volume Integral Equation Approach

In this section, the formulation of the volume integral-equation with a spectral dyadic Green's function is given first, followed by the current discretization and system matrix structure. Afterwards, analytical evaluation in space-domain integration is carried out and m=1 Green's function is obtained in 5.2.3. Subsequently, techniques for the integration are briefly described.

5.2.1 Volume-integral equation formulation for the NRD-guide and H-guide circuits

Fig. 5.1 shows the top-view (planar-section) of a multiport NRD-guide or H-guide circuit that is sandwiched between two parallel infinitely extended metal plates. The core circuit relates to the external circuits through L physical ports attached to an equal number of intrinsic standard NRD-guide or H-guide feed lines. These feed-lines are assumed to be semi-infinite long with the same height a, different width b_l, and constant dielectric permittivity ε_l. The core circuit may be in the form of NRD-guide or H-guide with the dielectric permittivity ε varying in the x-y plane $\varepsilon(x,y)$. The whole circuit is surrounded by a medium with a constant dielectric permittivity ε_s.

Suppose that the total field is **E**, the polarized volume current can be expressed by the volume equivalent theorem in section 2.1.2 as

$$\mathbf{J}_v(\mathbf{r}) = j\omega(\varepsilon(x,y)-\varepsilon_s)\mathbf{E}(\mathbf{r}) \tag{5.1}$$

The electric field generated by the polarized volume current $\mathbf{J}_v$ is:

$$\mathbf{E}(\mathbf{r}) = j\omega\mu_0 \iiint_V dV' \overline{\mathbf{G}}(\mathbf{r},\mathbf{r}') \cdot \mathbf{J}_v(\mathbf{r}') \tag{5.2}$$

where V is the space occupied by the dielectric strips. The DGF $\bar{\mathbf{G}}(\mathbf{r},\mathbf{r}')$ in the spectral domain, $\tilde{\bar{\mathbf{G}}}(k_x,k_y,z,z')$, for the two parallel metal plates can be

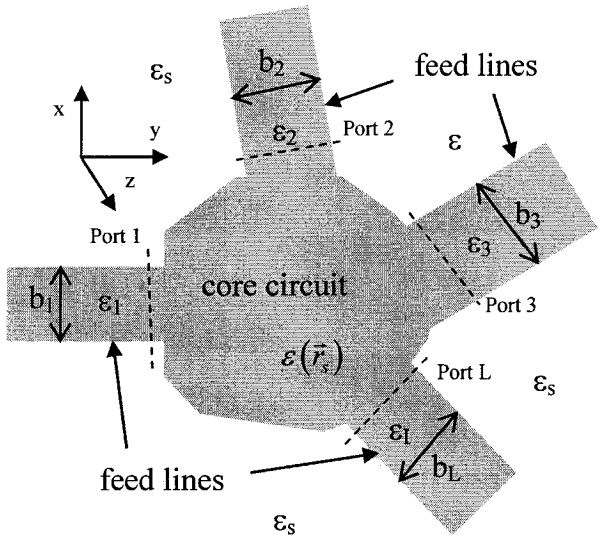

Fig.5.1. Top view of the dielectric circuits of NRD-guide and H-guide

obtained from (4.3) and can be expressed as:

$$\tilde{\bar{\mathbf{G}}}(k_x,k_y,z,z')=\frac{1}{2\omega\varepsilon_s}\cdot\begin{bmatrix} j(k_s^2-k_x^2)g_1 & -jk_xk_yg_1 & k_xg_2 \\ -jk_xk_yg_1 & j(k_s^2-k_x^2)g_1 & k_yg_2 \\ -k_xg_3 & -k_yg_3 & j(k_x^2+k_y^2)g_4+j\delta(z-z') \end{bmatrix} \quad (5.3)$$

where

$$g_1=\begin{cases} \dfrac{\sin k_z(z+a)\sin(k_zz')}{k_z\sin(k_za)} & z<z' \\ \dfrac{\sin(k_zz)\sin k_z(z'+a)}{k_z\sin(k_za)} & z>z' \end{cases}$$

$$g_2 = \begin{cases} \dfrac{\sin k_z (z+a)\cos k_z z'}{\sin k_2 a} & z < z' \\ \dfrac{\sin k_z z \cos k_z (z'+a)}{\sin k_z a} & z > z' \end{cases}$$

$$g_3 = \begin{cases} \dfrac{\cos k_2 (z+a)\sin k_2 z'}{\sin k_2 a} & z < z' \\ \dfrac{\cos k_2 z \sin k_2 (z'+a)}{\sin k_2 a} & z > z' \end{cases}$$

$$g_4 = \begin{cases} \dfrac{\cos k_2 (z+a)\cos k_2 z'}{k_2 \sin k_2 a} & z < z' \\ \dfrac{\cos k_2 z \cos k_2 (z'+a)}{k_2 \sin k_2 a} & z > z' \end{cases}$$

and $k_z^2 = \varepsilon_s k_0^2 - k_x^2 - k_y^2$, $k_s = \sqrt{\varepsilon_s / \varepsilon_0} k_0$

In this Green's function, the poles at which denominator equals to zero represent the parallel plate waveguide modes, which form the radiation loss mechanism in discontinuities in NRD-guide and H-guide circuits. These poles occur at $k_z a = m\pi, m = 0,1,2,3,\ldots$, where $k_\rho = \sqrt{k_s^2 - (m\pi/a)^2}$ ($k_\rho^2 = k_x^2 + k_y^2$) and correspond to the cutoff frequencies of continuous radiation modes as discussed in section 3.2. There is always at least one pole that represents the m=0 continuous radiation mode as shown in Fig. 3.2(a). Another pole, representing the m=1 propagating radiation mode as shown in Fig. 3.2(b), appears in the Green's function at $k_s > \pi/a$. With the increasing of frequency (k_0) or increasing of the distance between the two plates (a), more poles (m>1) will appear in this Green's function.

5.2.2 Current discretization and system matrix structure

The volume integral equation (5.1) can be solved with Garlerkin's MoM. Generally, the volume polarized current discretization should be made in three dimensions and this

would make the matrix too large and make this method inefficient because of large memory and CPU time requirement. However, the NRD-guide and H-guide circuits in Fig. 5.1 can be viewed as sections of dielectric waveguides that are short-circuited by two infinite parallel metal plates, placed perpendicularly to the longitudinal axis (z) at a certain distance apart. In this case, the propagating constant along z, namely, β_z is fixed by the presence of the plates ($\beta_z=m\pi/a$, with null or integer m). In this chapter, only the m=1 eigen mode excitation is considered. So, only m=1 modes, including surface wave modes and a continuous radiation wave mode, appear in this circuit due to the orthogonal properties between different m modes. The eigen mode excitation with other m value is similar to the m=1 case. With the m=1 eigen mode excitation, a half-sinusoidal vertical (z) variation of fields (sin ($\pi(z+a)/a$) in x,y components and $\cos(\pi(z+a)/a)$ in z component) remains unchanged over the entire circuits. The discretization can be made only in x-y plane just as planar circuits. In this case, the matrix is greatly reduced and becomes solvable for complicated circuits.

In Fig. 5.1, the volume current of polarization can be represented by combined local and propagating modes basis functions. Local mode means that the field is restricted in a finite region of the circuit while the propagating mode means that the field will propagate out of the circuit or propagate into the circuit from outside through the feed lines. The local mode can be either entire mode or sub-sectional mode and the propagating mode, of course, is the entire mode. The field in the core circuit can be represented by the local modes that either can be entire modes or sub-sectional modes with rectangular or triangular meshes to fit different planar sections. The field along the feed lines consists of a discrete number of surface-wave modes and a continuous radiation mode as shown in Fig. 3.2(b). The propagating surface-wave modes can be represented by propagating mode basis functions and the exponent terms in propagating modes are truncated after several cycles. The evanescent surface wave modes, if appear, can be represented by local modes, and the entire-domain basis functions are more efficient for them since they decay more slowly than the evanescent radiation modes. The radiation mode is totally evanescent in the frequency region of the NRD-guide, and

becomes partly evanescent, and partly propagating in the operating frequency of H-guide. The evanescent radiation mode can be represented by local modes for which the sub-sectional basis functions are more efficient. The propagating part of the radiation mode that will cause radiation loss in bends and discontinuities is represented by the m=1 pole in the Green's function (5.3).

With the introduced basis functions, the polarized volume current in the circuits and feed-lines can be written as:

$$\begin{aligned}\mathbf{J}_v = &\left(f_{x,inc}^{m(e)}(x,y) + \sum_{l=1}^{L}\sum_{e,m} T_l^{e,m} f_{x,l}^{e,m}(x,y) + \sum_{j=1}^{J} I_{x,j}\cdot f_{x,j}(x,y) \right)\cdot \sin\left\langle \frac{\pi(z+a)}{a} \right\rangle \hat{\mathbf{e}}_x \\ &+ \left(f_{y,inc}^{m(e)}(x,y) + \sum_{l=1}^{L}\sum_{e,m} T_l^{e,m} f_{y,l}^{e,m}(x,y) + \sum_{j=1}^{J} I_{y,j}\cdot f_{y,j}(x,y) \right)\cdot \sin\left\langle \frac{\pi(z+a)}{a} \right\rangle \hat{\mathbf{e}}_y \\ &+ \left(f_{z,inc}^{m(e)}(x,y) + \sum_{l=1}^{L}\sum_{e,m} T_l^{e,m} f_{z,l}^{e,m}(x,y) + \sum_{j=1}^{J} I_{z,j}\cdot f_{z,j}(x,y) \right)\cdot \cos\left\langle \frac{\pi(z+a)}{a} \right\rangle \hat{\mathbf{e}}_z\end{aligned} \quad (5.4)$$

where $f_{v,l}^{e,m}(x,y)$ (v=x,y,z) are planar parts of the propagating modes in lth feed-line including LSE or LSM modes, which have exact analytical expressions. $f_{v,j}(x,y)$ are planar parts of the local modes. $f_{v,inc}^{m(e)}(x,y)$are planar parts of the incident propagating mode that can be either LSM_{11} mode or LSE_{11} mode. We call $f_{v,j}(x,y)$, $f_{v,l}^{e,m}(x,y)$ and $f_{v,l}^{e,m}(x,y)$ planar basis functions. $T_l^{e,m}$ are the unknown transmission coefficients of propagating modes at port l. J is the number of the unknown planar local modes. $I_{v,j}$ is the coefficients of the unknown planar local modes.

Only the local modes, $f_{x,i}(x,y)\sin(\pi(z+a)/a)\hat{\mathbf{e}}_x$ $f_{y,i}(x,y)\sin(\pi(z+a)/a)\hat{\mathbf{e}}_y$ $f_{z,i}(x,y)\cos(\pi(z+a)/a)\hat{\mathbf{e}}_z$, are used as testing functions in this Galerkin's method of moments. The discretized integral-equation system is solved and a linear system of equations can be obtained as

$$\begin{bmatrix} [Z_{xt}] & [Z_{xx}] & [Z_{xy}] & [Z_{xz}] \\ [Z_{yt}] & [Z_{yx}] & [Z_{yy}] & [Z_{yz}] \\ [Z_{zt}] & [Z_{zx}] & [Z_{zy}] & [Z_{zz}] \end{bmatrix} \cdot \begin{bmatrix} [T] \\ [I_x] \\ [I_y] \\ [I_z] \end{bmatrix} = -\begin{bmatrix} [Z_{x,inc}] \\ [Z_{y,inc}] \\ [Z_{z,inc}] \end{bmatrix} \tag{5.5}$$

$[Z_{uv}]$ are impedance sub-matrices of self and mutual couplings between the two local modes of u (u=x, y, z) and v components. $[Z_{u,t}]$ and $[Z_{u,inc}]$ are impedance sub-matrices of mutual couplings between the local modes and propagating modes where $[Z_{u,t}] = \sum_{v=x,y,z} [Z_t^{uv}]$ and $[Z_{u,inc}] = \sum_{v=x,y,z} [Z_{inc}^{uv}]$. $[Z_t^{uv}]$ and $[Z_{inc}^{uv}]$ are the coupling between the local mode and v's component of the propagating mode.

One of the crucial points of the method of moments lies in effective and accurate evaluation of the system matrix entries. These entries can be obtained by a spectral-domain integration with the vertical part still in space-domain as follows,

$$z_{ij}^{uv} =$$

$$\frac{1}{4\pi^2}\int_{k_x}\int_{k_y}\int_z\int_{z'} \tilde{G}_{uv}(k_x,k_y,z,z')\cdot \tilde{f}_{u,i}^*(k_x,k_y)\cdot g_u(z)\cdot \tilde{f}_{v,j}(k_x,k_y)\cdot g_v(z')dk_xdk_ydzdz' \tag{5.6}$$

$$-\int_x\int_y\int_z \frac{f_{u,i}(x,y)\cdot g_u(z)\cdot f_{v,j}(x,y)\cdot g_v(z)}{j\omega(\varepsilon(x,y)-\varepsilon_s)}dxdydz\cdot\delta_{uv}$$

$$z_{i,p}^{uv} =$$

$$\frac{1}{4\pi^2}\int_{k_x}\int_{k_y}\int_z\int_{z'} \tilde{G}_{uv}(k_x,k_y,z,z')\cdot \tilde{f}_{u,i}^*(k_x,k_y)\cdot g_u(z)\cdot \tilde{f}_{v,p}(k_x,k_y)\cdot g_v(z')dk_xdk_ydzdz' \tag{5.7}$$

$$-\int_x\int_y\int_z \frac{f_{u,i}(x,y)\cdot g_u(z)\cdot f_{v,p}(x,y)\cdot g_v(z)}{j\omega(\varepsilon(x,y)-\varepsilon_s)}dxdydz\cdot\delta_{uv}$$

Here we merge the incidental terms with the transmission terms in (5.7) and use the subscript p to represent I and inc. $\tilde{f}_{v,i}(k_x,k_y)$ and $\tilde{f}_{v,p}(k_x,k_y)$ are Fourier transforms of the planar basis functions $f_{v,i}(x,y)$ and $f_{v,p}(x,y)$. The functions of $g_u(z)$ and $g_v(z)$ are $g_x(z)=g_y(z)=\sin\langle\pi(z+a)/a\rangle$ and $g_z(z)=\cos\langle\pi(z+a)/a\rangle$.

The power flow at ports is formulated by

$$P = \frac{1}{2}\mathrm{Re}\int_S \left(\mathbf{E}\times\mathbf{H}^*\right)\cdot d\mathbf{s} \tag{5.8}$$

Since the electromagnetic field of the surface waves have exact analytic expressions as in section 3.2, the power of the propagating modes at port l can be obtained analytically as:

$$P_l^m = \frac{1}{2}A^2\frac{\omega\varepsilon_0\beta_l^m}{\varepsilon_l}\cdot\left(k_0^2\varepsilon_l - \beta_{w,l}^{m\,2}\right)\cdot\frac{a}{2}\cdot\left[\frac{b_l}{2}+\frac{\sin\left(\beta_{w,l}^m b_l\right)}{2\beta_{w,l}^m}+\frac{\cos^2\left(\beta_{w,l}^m b_l/2\right)}{\varsigma_l^m}\right] \tag{5.9}$$

for LSM_{11} mode, and

$$P_l^e = \frac{1}{2}B^2\omega\mu_0\beta_l^e\left(k_0^2\varepsilon_l - \beta_{w,l}^{m\,2}\right)\cdot\frac{a}{2}\cdot\left[\frac{b_l}{2}+\frac{\sin\left(\beta_{w,l}^e b_l\right)}{2\beta_{w,l}^e}+\frac{\cos^2\left(\beta_{w,l}^e b_l/2\right)}{\varsigma_l^e}\right] \tag{5.10}$$

for LSE_{11} mode. $\beta_l^{m(e)}$ is the propagating constant of the $LSM_{11}(LSE_{11})$ mode, $\beta_{w,l}^{m(e)}$ is the transverse wave number inside the dielectric, and $\varsigma_l^{m(e)}$ is the transverse wave number outside the dielectric. A and B are coefficients in the analytical expressions of LSM_{11} and LSE_{11} modes.

Suppose that the circuit is excited by a LSM_{11} or LSE_{11} mode at port l, then the S-parameters can be obtained by

$$S_{l,l'}^{m(e),m(e)} = T_{l'}^{m(e)}\cdot\sqrt{P_{l'}^{m(e)}/p_l^{m(e)}} \tag{5.12}$$

where $T_{l'}^{m(e)}$ can be obtained in (5.6).

5.2.3 Analytical evaluation in space-domain integrations and m=1 Green's function

The space-domain integrals within (5.6)-(5.7) in connection with variables z and z' can be evaluated analytically. The vertical integration of (x,x), (x,y), (y,x) and (y,y) components that are concerned with g_1 function in (5.3) is

$$IVV_{ss} = \int_{-a}^{0} dz \cdot \sin\langle \pi(z+a)/a \rangle \cdot \left[\frac{\sin\langle k_z z \rangle}{k_z} \int_{-a}^{z} \frac{\sin\langle k_z (z'+a) \rangle}{\sin\langle k_z a \rangle} \sin\langle \pi(z'+a)/a \rangle dz' \right.$$
$$\left. + \frac{\sin\langle k_z (z+a) \rangle}{\sin\langle k_z a \rangle} \int_{z}^{0} \frac{\sin\langle k_z z' \rangle}{k_z} \sin\langle \pi(z'+a)/a \rangle dz' \right] \qquad (5.12)$$
$$= \frac{a}{2} \cdot \frac{1}{k_z^2 - (\pi/a)^2}$$

The results of the vertical integration of (x,z) and (y,z) components related to g_2 function in (5.3) can be obtained by

$$IVV_{sc} = \int_{-a}^{0} dz \sin\langle (z+a)\pi/a \rangle \cdot \left[\frac{\sin\langle k_z (z+a) \rangle}{\sin k_z a} \int_{z}^{0} \cos k_z z' \cdot \cos\langle (z'+a)\pi/a \rangle dz' \right.$$
$$\left. + \frac{\sin\langle k_z z \rangle}{\sin k_z a} \int_{-a}^{z} \cos k_z (z'+a) \cdot \cos\langle (z'+a)\pi/a \rangle dz' \right] \qquad (5.13)$$
$$= \frac{\pi}{2} \cdot \frac{1}{k_z^2 - (\pi/a)^2}$$

Similarly, results of the vertical integration of (z,x) and (z,y) components related to g_3 function in (5.3) can be obtained by

$$IVV_{cs} = \int_{-a}^{0} dz \cos\langle (z+a)\pi/a \rangle \cdot \left[\cos k_z (z+a) dz \int_{z}^{0} dz' \frac{\sin\langle k_z z' \rangle}{\sin k_z a} \cdot \sin\langle (z'+a)\pi/a \rangle \right.$$
$$\left. + \cos k_z z \int_{-a}^{z} \frac{\sin\langle k_z (z'+a) \rangle}{\sin k_z a} \cdot \sin\langle (z'+a)\pi/a \rangle dz' \right] \qquad (5.14)$$
$$= \frac{\pi}{2} \cdot \frac{1}{k_z^2 - (\pi/a)^2}$$

Once again, results of the vertical integration of (z,z) component dealing with g_4 function in (5.3) can be obtained by

$$IVV_{cc} = \int_{-a}^{0} dz \cos\langle (z+a)\pi/a \rangle \cdot \left[\frac{\cos\langle k_z (z+a) \rangle}{\sin k_z a} \int_{z}^{0} dz' \frac{\cos\langle k_z z' \rangle}{k_z} \cdot \cos\langle (z'+a)\pi/a \rangle \right.$$
$$\left. + \frac{\cos\langle k_z z \rangle}{k_z} \int_{-a}^{z} \frac{\cos\langle k_z (z'+a) \rangle}{\sin k_z a} \cdot \cos\langle (z'+a)\pi/a \rangle dz' \right] \qquad (5.15)$$
$$= \frac{a}{2} \cdot \frac{1}{k_z^2 - (\pi/a)^2}$$

And results of the vertical integration concerning with source in $\tilde{G}_{zz}$ in (5.3) can be obtained by

$$IVV_1 = \int_{-a}^{0} dz \cos\langle (z+a)\pi/a \rangle \int_{-a}^{0} \cos\langle (z'+a)\pi/a \rangle \cdot \delta(z-z') dz' = a/2 \qquad (5.16)$$

Then, the $\tilde{G}_{zz}$ component in the square brackets in (5.3) can be simplified by combining the source term (5.16) with the principle term (5.15), and using the separation condition $k_z^2 = k_s^2 - k_x^2 - k_y^2$ as

$$\left(k_x^2 + k_y^2\right) \cdot IVV_{cc} + IVV_1 = \frac{a}{2} \cdot \frac{\varepsilon_s k_0^2 - (\pi/a)^2}{\varepsilon_s k_0^2 - k_x^2 - k_y^2 - (\pi/a)^2} \qquad (5.17)$$

The vertical integration in connection with the second term in (5.6), (5.7) can be obtained by

$$IV_{ss} = \int_{-a}^{0} \sin\left(\pi(z+a)/a\right) \cdot \sin\left(\pi(z+a)/a\right) dz = a/2$$
$$IV_{cc} = \int_{-a}^{0} \cos\left(\pi(z+a)/a\right) \cdot \cos\left(\pi(z+a)/a\right) dz = a/2 \qquad (5.18)$$

With the help of (5.12)-(5.15), a new Green's function can be constructed as

$$\tilde{\tilde{\mathbf{G}}}_{m1}(k_x, k_y) = \frac{1}{2\omega\varepsilon_s} \cdot \frac{1}{T_{em}} \cdot \begin{bmatrix} j\frac{a}{2}\left(k_s^2 - k_x^2\right) & -j\frac{a}{2}k_x k_y & \frac{\pi}{2}k_x \\ -j\frac{a}{2}k_x k_y & j\frac{a}{2}\left(k_s^2 - k_y^2\right) & \frac{\pi}{2}k_y \\ -\frac{\pi}{2}k_x & -\frac{\pi}{2}k_y & j\frac{a}{2}\left(k_s^2 - (\pi/a)^2\right) \end{bmatrix} \qquad (5.19)$$

where $T_{em} = k_s^2 - k_x^2 - k_y^2 - (\pi/a)^2$. With this Green's function, the integration in (5.6) and (5.7) can be written as

$$z_{ij}^{uv} = \frac{1}{4\pi^2}\int_{k_x}\int_{k_y} \tilde{G}_{m1}^{uv}(k_x,k_y)\cdot \tilde{f}_{u,i}^{*}(k_x,k_y)\cdot \tilde{f}_{v,j}(k_x,k_y)dk_x dk_y + \frac{a}{2}\cdot\int_x\int_y \frac{f_{u,i}(x,y)\cdot f_{v,j}(x,y)}{j\omega(\varepsilon(x,y)-\varepsilon_s)}dxdy\cdot\delta_{uv} \tag{5.20}$$

$$z_{i,p}^{uv} = \frac{1}{4\pi^2}\int_{k_x}\int_{k_y} \tilde{G}_{m1}^{uv}(k_x,k_y)\cdot \tilde{f}_{u,i}^{*}(k_x,k_y)\cdot \tilde{f}_{v,p}(k_x,k_y)dk_x dk_y + \frac{a}{2}\cdot\int_x\int_y \frac{f_{u,i}(x,y)\cdot f_{v,p}(x,y)}{j\omega(\varepsilon(x,y)-\varepsilon_s)}dxdy\cdot\delta_{uv} \tag{5.21}$$

The Green's function in (5.19) is simpler than (5.3) without triangular functions in it. The $\hat{z}\hat{z}$ component in the square bracket is very much simplified as a constant. Only m=1 pole appears in this Green's function in the condition of $a/\lambda_0 > 0.5$. Other poles, especially the ever-existing m=0 pole, are eliminated through the vertical integrations in (5.16)-(5.19). Since this Green's function only governs the m=1 case for NRD-guide and H-guide circuits, we call it as the m=1 Green's function and refer to (5.3) as the full-scale Green's function. The integrations in (5.20) and (5.21) are two-dimensional in the spectral-domain with respect to k_x and k_y just same as in planar circuits. With the 2-D discretization technique, the solution of the volume integral equation for NRD-guide and H-guide circuits has been reduced to a completely 2-D planar problem.

5.2.4 Some technique for numerical integrations

The integrations in (5.20) and (5.21) are similar to those used in planar circuits but much simpler because of the simple m=1 Green's functions. Many kinds of planar basis function such as piecewise sinusoidal functions, pulse basis functions with rectangular or triangular mesh scheme or entire mode can be used for the local modes to fit different cross sections of circuits just as used in planar circuits.

When poles appear, the numerical integration must be carried out in polar coordinate with $k_\rho = \sqrt{k_x^2 + k_y^2}$ and $\varphi = \arctan(k_y / k_x)$ because the poles appear at

$k_\rho = \sqrt{(\pi/a)^2 - k_s^2}$. However, when there are no poles in the integration, they can be carried out either in polar coordinate or in rectangular coordinate. In the case of planar basis functions for NRD-guide circuit, integrands $\tilde{f}_i^*(k_x,k_y)\cdot\tilde{f}_j(k_x,k_y)$ and $\tilde{f}_i^*(k_x,k_y)\cdot\tilde{f}_p(k_x,k_y)$ can be rearranged as $g(k_x)\cdot h(k_y)$ and $g(k_x)$, $h(k_y)$ and oscillate with a sinusoidal behavior. So the integrations in rectangular coordinate are more efficient than in its polar counterpart.

The integrations in polar coordinate with poles were discussed in [120] and [97]. A general asymptotic subtraction technique was used in [97]. In this technique, the asymptotic behavior of integrands was searched prior to performing the numerical computations. Subtracting these representations leads to a fast decaying integrand, the integral thus becomes well suited for a numerical integration; the complete analytical solutions can be determined for the asymptotic part. This technique can be also applied in rectangular coordinate. The symmetric property and redundancy reduction techniques can also be used to reduce calculation effort in this method. Some of these properties will be shown in the following examples.

5.3 Numerical Results

Several examples are discussed in this section to demonstrate properties and efficiency of the ORVIE approach. The main emphasis focuses on NRD-guide circuits because of their important applications at millimeter wave frequencies. The following solution procedure of the NRD-guide open-end is presented to showcase the features of the ORVIE approach.

5.3.1 NRD-guide open-ends

The most difficult part of the ORVIE approach lies in dealing with feed lines in which both propagating mode and local mode basis functions are used. Here we will

discuss the calculation procedure of an NRD-guide open-end whose field distribution is similar to that along the feed lines. The NRD-guide open-end itself is also frequently encountered in the design of passive components and active devices. The effects of the open-end have been studied first in [37] with a mode-matching method.

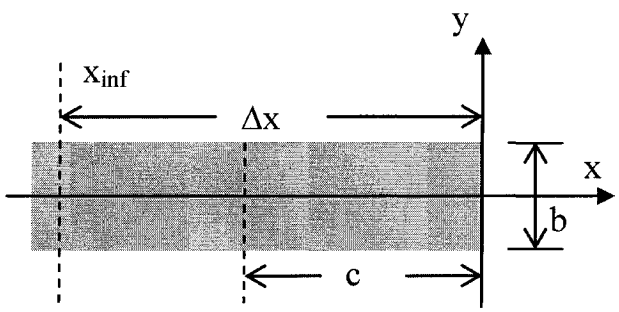

Fig.5.2. NRD-guide and H-guide open ends

The planar section of an NRD-guide open-end with width b=3.556 mm, thickness a=5.0 mm, and ε_r=2.56 is shown in Fig. 5.2. Only a reflected LSM_{11} mode and a continuous evanescent radiation mode are produced in this structure when an LSM_{11} mode is used as the incident mode with the above parameters. Fields of the radiation mode can be represented by sub-sectional basis functions over certain region of calculation. The length of region of calculation c as shown in Fig. 5.2 depends on the average decay constant of the radiation mode. By defining a weighting average decay constant $\alpha = \left(3\sqrt{(\pi/a)^2 - k_0^2} + \pi/a\right)/4$, generally $c = 2\pi/\alpha$ is enough. We divide the calculation region S into Q by R cells of equal area. The length of each cell is D_x=c/Q along the x direction, and D_y=b/R along with y direction. The center coordinate of the (q, r) cell, S_{qr}, is denoted by (x_q, y_r) with 1≤q≤Q and 1≤r≤R. Planar basis functions for the radiation mode can thus be represented by a set of pulse basis functions as follows

$$\mathbf{f}_j(x,y) = \sum_{v=x,y,z} \hat{\mathbf{v}} P_q(x) W_r(y) \tag{5.22}$$

where

$$P_q(x)=\begin{cases}1, & x_q - D_x/2 \le x \le x_q + D_x/2\\ 0, & elsewhere\end{cases}$$

$$W_r(y)=\begin{cases}1, & y_r - D_y/2 \le y \le y_r + D_y/2\\ 0, & elsewhere\end{cases} \tag{5.23}$$

and $j=(q-1)\cdot R+r$

The planar propagating mode basis functions are

$$\mathbf{f}_p(x,y)= j\omega(\varepsilon-\varepsilon_0)\mathbf{E}e^{\pm j\beta x} \tag{5.24}$$

where

$$E_x = \pm(j/\varepsilon_r)\beta\beta_y \sin(\beta_y y) \tag{5.25a}$$

$$E_y = (1/\varepsilon_r)(k_0^2\varepsilon_r - \beta_y^2)\cos(\beta_y y) \tag{5.25b}$$

$$E_z = -(\beta_y/\varepsilon_r)(\pi/a)\sin(\beta_y y) \tag{5.25c}$$

The upper sign in (5.24) and (5.25) represents the reflected wave and the lower sign represents the incident wave. Fourier transforms of $\mathbf{f}_j(x,y)$ and $\mathbf{f}_p(x,y)$ are given in Appendix B. Exponent terms in (5.24) are truncated after several cycles. It is found that choosing a length of the exponent as an integral number of wavelength speeds up the convergence of integrals. The length of the exponent Δx depends on the length of the calculation region c of the radiation mode. Typically the solution is insensitive to the wave exponent length for greater than three or four times c.

We choose the same set of sub-sectional basis functions $\hat{\mathbf{u}}P_s(x)W_t(y)$ as the testing functions. Also, the even and odd properties of the integrand can be used to reduce the integration range to the first quadrant in k_x-k_y coordinate, the integration of element in (5.20) and (5.21) can be written as

$$\begin{aligned} z_{ij}^{uv} = {} & \frac{1}{\pi^2}\int_0^\infty\int_0^\infty G_{m1}^{uv}(k_x,k_y)\cdot Int_{ij}^{uv}(k_x,k_y)dk_x dk_y \\ & + \frac{1}{j\omega(\varepsilon_j-\varepsilon_s)}\cdot\frac{a}{2}\cdot D_x\cdot D_y\cdot\delta_{uv}\cdot\delta_{sq}\cdot\delta_{tr} \end{aligned} \tag{5.26}$$

$$z_{i,p}^{uv} = \frac{1}{\pi^2}\int_0^{\infty}\int_0^{\infty} G_{m1}^{uv}\left(k_x,k_y\right)\cdot Int_{i,p}^{uv}\left(k_x,k_y\right)dk_x dk_y + \frac{1}{j\omega\left(\varepsilon_l-\varepsilon_s\right)}\cdot\frac{a}{2}\cdot w_{i,p}^{uv}\delta_{uv} \qquad (5.27)$$

The integrands Int_{ij}^{uv}, $Int_{i,p}^{uv}$ and $w_{i,p}^{uv}$ terms are given in Appendix.B

The integrations in (5.26) and (5.27) can be carried out in rectangular coordinate (k_x, k_y) since the integrands oscillate in coordinates k_x and k_y respectively as shown in Appendix B. The integrations are defined through infinite spectral integrals and they can be evaluated numerically by restricting the unbounded integration interval [0, ∞] to the finite region [0, K_x,] and [0, K_y] where K_x and K_y are sufficiently large numbers. The integrands exhibit a rapidly oscillating behavior, amplitude of the integrands decreases as $1/k_x^{\nu}$ and $1/k_y^{\nu}$. For the integer number ν, it is found that $\nu \geq 2$, and the convergence of the integrals is thus ensured. The weakest convergence ν=2 characterizes the second terms of G_{m1}^{xx} and G_{m1}^{yy}. At this point, it would be beneficial to search for asymptotic behavior of the integrands prior to performing the numerical computation. The integration term relating to G_{m1}^{xx} can be written as

$$Int = \int_0^{K_y} g^* g\left(k_y\right)\left\{\int_0^{K_x}\left[k_x^2 f^* f\left(k_x\right)/T_{em} + f^* f^A\left(k_x\right)\right]dk_x - \int_0^{\infty} f^* f^A\left(k_x\right)dk_x\right\}dk_y \qquad (5.28)$$

The asymptotic term T_{em}, T_{em}^A, is equal to $-k_x^2$. To make $T_{em}^A = -k_x^2$ valid for all k_y, K_y should be much greater than K_x. Since the integrand with large k_y contributes little to the total integration, $K_y \approx 2K_x$ is enough. Subtracting the asymptotic terms, $f^* f_{sq}^A\left(k_x\right)$ and $f^* f_{s,p}^A\left(k_x\right)$ which are given in Appendix, in the first integral of (5.28) leads to a fast decaying integrand. The integral thus becomes well suited for a numerical integration.

For the second integral, called the asymptotic part, complete analytical solutions can be determined as:

$$\int_0^{\infty} f^* f_{s,p}\left(k_x\right)_{even}^A dk_x = \pi D_x \qquad (5.29)$$

$$\int_0^{\infty} f^* f_{sq}\left(k_x\right)_{even} dk_x = -\pi D_x \delta_{sq} \qquad (5.30)$$

Integration terms concerning G_{m1}^{yy} have a similar solution for k_x that is changed to k_y.

In the case of a uniform mesh on rectangular structure with J basis functions, there are shifting terms Δx_{sq} and Δy_{tr} where $\Delta x_{sq} = \mathrm{sgn}(s-q)\cdot|s-q|\cdot D_x$ and $\Delta y_{tr} = \mathrm{sgn}(t-r)\cdot|t-r|\cdot D_y$ in (5.22), (5.23) and (5.28), (5.29). So only J different matrix elements of the J×J system matrix must be calculated. In this case, only several seconds of CPU time are needed for each frequency point.

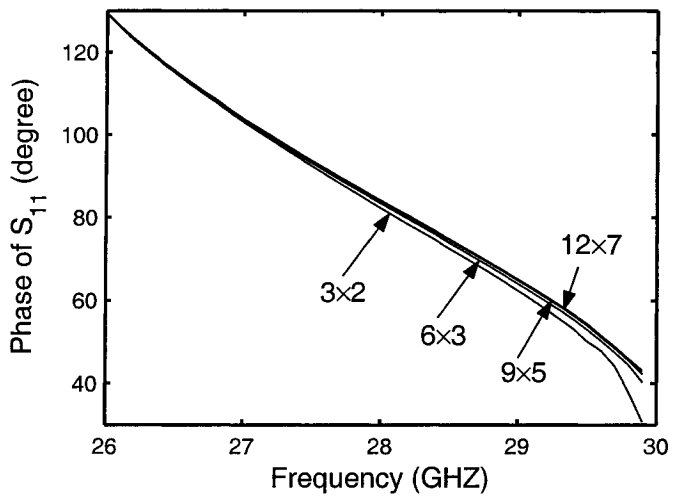

Fig.5.3. Frequency characteristics of the phase of S_{11} for the NRD-guide open-end structure with different mesh schemes

The NRD open-end is simulated with a frequency sweep between 26 GHz and 30 GHz. To estimate the error introduced by the discretization of the structure, the simulation was repeated on the basis of four different meshes with increasing cell density Q×R=3×2, 6×3, 9×5, 12×7. The calculated phases of S_{11} at the reference plane are plotted in Fig. 5.3 as a function of frequency while the magnitudes of S_{11} remains almost unit-constant in all the cases. The convergence is very satisfactory at low frequencies. However, more meshes should be used at high frequency since more fields due to the radiation mode are produced and decay slowly in the high frequencies region. In Fig. 5.4, our theoretical results are verified by comparing the amplitude and phase of

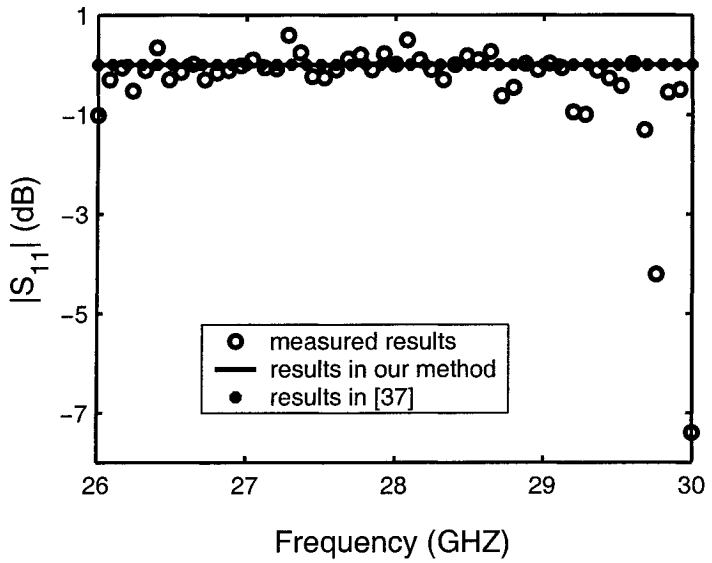

(a)

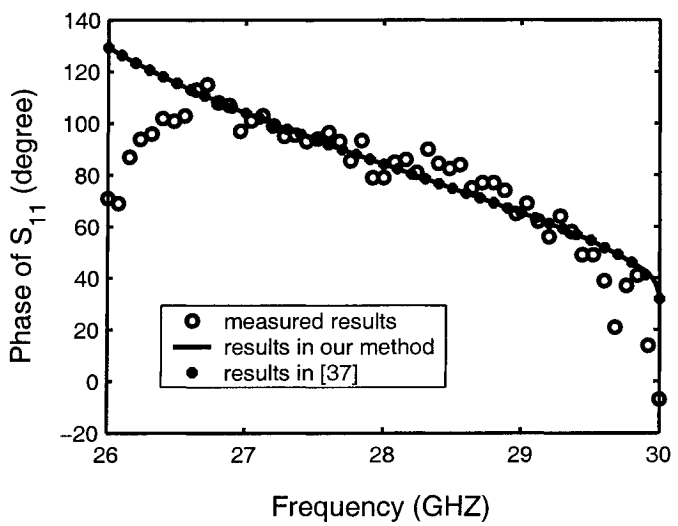

(b)

Fig.5.4. Calculated and measured results of S-parameters for the NRD-guide open-end discontinuity. (a) Amplitude of S_{11}; (b) Phase of S_{11}.

S_{11} with calculated and measured results in [37], showing a very good agreement. Measurement errors observed over the frequency range of interest were explained in [37], that is, the 26.5 GHz cutoff effect of the mode launcher from the rectangular waveguide causes to a large extent the phase deviation and the difference of results. Around the upper part of the frequency range, the errors may come from the fact that a is very close to the spacing limitation governed by the nonradiative condition of the guide, which is a half-wavelength in free space. Fig. 5.5 shows the field distribution of the radiation mode in x-y plane inside the dielectric medium. It can be seen that the field varies sinusoidally in the y direction and exponentially in the x-direction.

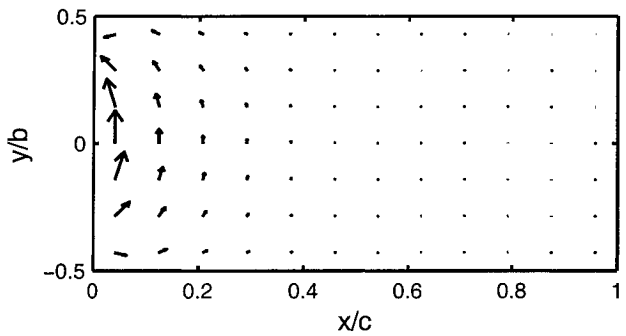

Fig.5.5. Field distribution of the m=1 radiation mode in the NRD-guide open end

5.3.2 H-guide open-end

As the frequency increases, the structure in Fig. 5.2 will become an H-guide. In this case, a pole at $k_\rho = \sqrt{k_s^2 - (\pi / a)^2}$ appears in the integrations, which must be carried out in polar coordinate. Fig. 5.6 shows the magnitude of S_{11} as a function of frequency. It can be seen that the magnitude decreases very rapidly just after the radiation loss appears, then slowly as the frequency continues to increase. This phenomenon can be well explained from the m=1 continuous radiation mode configuration in Fig. 3.2(b).

The level of radiation loss depends on the continuous spectrum width of the propagating radiation mode, $\Delta\beta = \beta_2 - 0$. The wider the spectrum is, the higher the radiation loss becomes. The slope rate of γ_2 is infinite at the start point of the propagating radiation mode $a/\lambda_0 = 0.5$, and this indicates that the increasing rate of the spectrum width is infinite. Therefore, the decreasing rate of radiation loss is infinite at the critical point f=30 GHz where $a/\lambda_0 = 0.5$ and the slope rate of the $|S_{11}|$ curve is also infinite at this critical point. As frequency increases, the slope rate of γ_2 becomes smaller and the increasing of the m=1 continuous spectrum width becomes slower. Therefore, the decreasing of the radiation loss becomes slower.

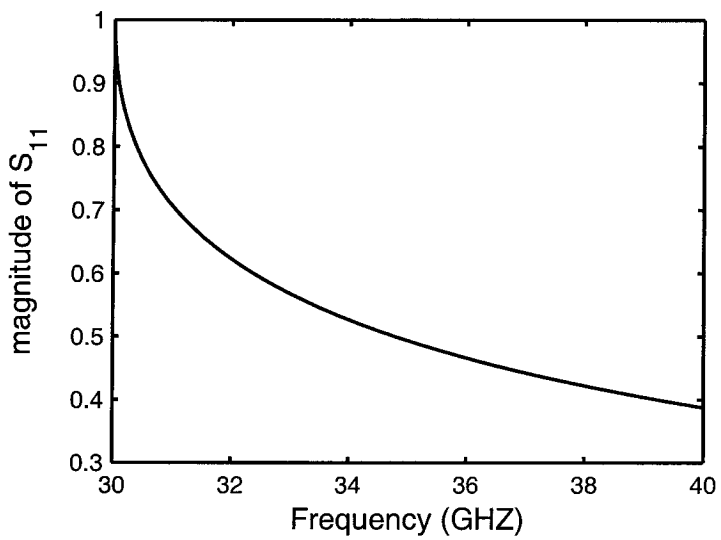

Fig.5.6. Calculated amplitude of S_{11} of H-guide open end.

5.3.3 NRD-guide resonators

The ORVIE approach can easily be used to solve the NRD guide resonators. A homogeneous linear system of equations can be obtained as follows for the core circuit in Fig. 5.1.

$$\begin{bmatrix} [Z_{xx}] & [Z_{xy}] & [Z_{xz}] \\ [Z_{yx}] & [Z_{yy}] & [Z_{yz}] \\ [Z_{zx}] & [Z_{zy}] & [Z_{zz}] \end{bmatrix} \begin{bmatrix} [I_x] \\ [I_y] \\ [I_z] \end{bmatrix} = 0 \tag{5.31}$$

Resonance frequencies can be obtained by letting the determinant of the coefficient matrix be zero.

$$\det[Z] = 0 \tag{5.32}$$

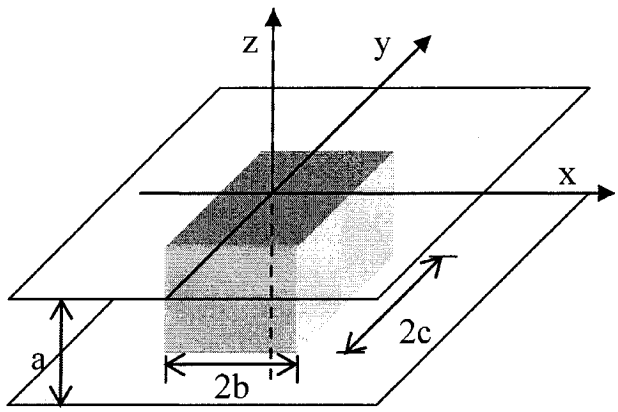

(a)

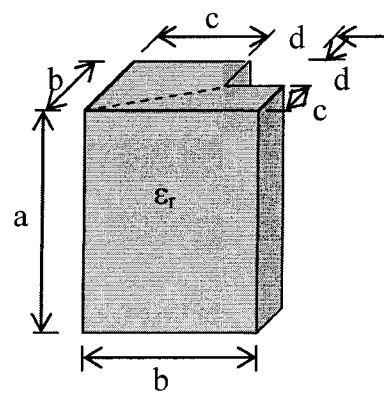

(b)

Fig.5.7. NRD-guide resonators. (a) Rectangular-section resonator. (b) Notched square-section resonator.

Table 5.1: Comparison of theoretical and experimental results for the resonant frequency (GHz) of different NRD resonators (ε_r=2.58).

dimensions a x 2b x 2c (mm^3)	LSM			LSE		
	measured values	method in [20]	this method	measured value	method in [20]	this method
13.57x9.85x5.90	10.79	10.81	10.78	10.97	10.97	10.93
13.57x9.85x8.97	10.51	10.47	10.46	10.56	10.53	10.52
13.55x9.85x11.96	10.23	10.22	10.22	10.09	10.06	10.06
13.59x9.87x14.90	10.05	10.00	10.00	9.75	10.67	9.66

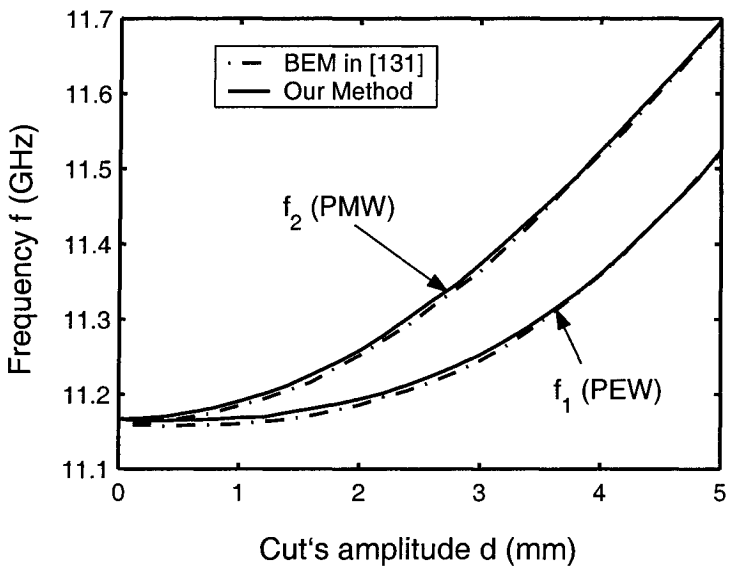

Fig.5.8. Variation of the quasi-dual resonant frequencies f_1 and f_2 for a square-section NRD-guide resonator (illustrated in Fig. 5.7(b)) as the corner's cut d varies with parameters: ε_r=2.53; a=12.3 mm; b=10 mm.

Four rectangular planar section resonators with different dimensions are calculated for comparison with measured results to validate the proposed method. Table 5.1 summarizes the measured and simulated resonant frequencies of the four different resonators. Theoretical results obtained with a numerical approach in [82] are also

presented in this table for comparison, and this approach effectively combines the method of lines with the mode-matching method. It is found that those results coincide well with each other for both LSE and LSM modes.

Then, a notched square-section resonator is modeled as shown in Fig. 5.7(b), which was first calculated precisely with a boundary element method (BEM) in [121]. A symmetric cut d is considered along a corner of the square-section (height a, unperturbed sides b, notched sides c, so that b=c+d). In this case, a pair of resonance is related to perfect electric and perfect magnetic symmetry walls placed along the notched-square minor diagonal, dashed in Fig. 5.7(b). Fig. 5.8 shows variation of the quasi-dual resonant frequencies f_1 and f_2 as a function of d in the notched square-section NRD resonator for the lowest pair of resonance. It is shown that results from BEM and ORVIE methods agree very well. The maximum difference between the two methods is less than 0.01GHz and it mainly comes from the finite discretization in these two methods.

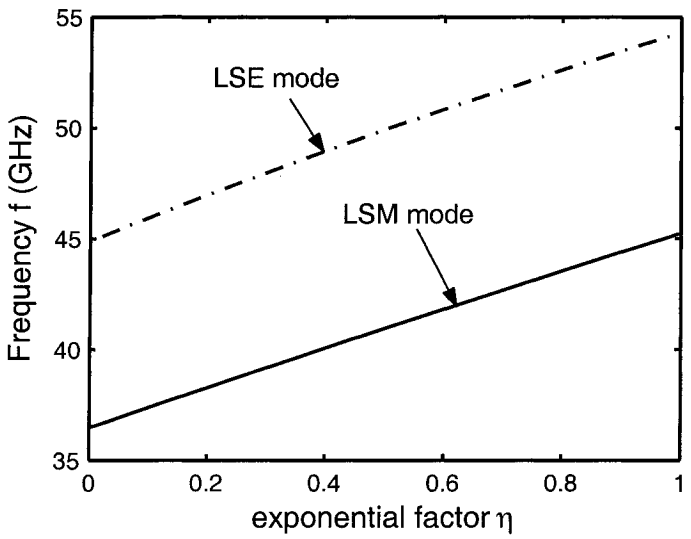

Fig.5.9. Resonant frequency characteristics of an inhomogeneous dielectric resonator against the exponential decaying factor η for both LSM and LSE fundamental modes (a=2.25 mm, b=0.6 mm, c=1.25 mm).

The BEM can solve resonators of arbitrary shape but with constant dielectric permittivity profile. The method in [82] can model inhomogeneous dielectric resonator problem but the permittivity can vary in one direction only. Our proposed ORVIE approach has no such limitation, and it can handle resonator with any shape of planar section and with dielectric permittivity varying in both x, y directions. Fig. 5.9 depicts resonant characteristics of an inhomogeneous resonator with a profile function of the dielectric permittivity in the following

$$\varepsilon_r(x,y) = \varepsilon_{r0} \cdot e^{-\eta\left[\left(\frac{c-x}{c}\right)^2 + \left(\frac{b-y}{b}\right)^2\right]} \tag{5.33}$$

in which η is an exponentially decaying factor and ε_{r0} (= 9.5 in this example) the maximum permittivity of the dielectric resonator. It indicates that both the LSE and LSM modes have a quasi-linear increase with exponential factor. This has also verified the analysis in [82], in which only LSM mode has this behavior while the LSE mode is not sensitive to high decaying factor of the inhomogeneous dielectric. This phenomenon was explained in [82] because the dielectric permittivity ε_r only varies in x-direction but remains constant in y-direction in that case.

5.3.4 NRD-Guide Filter

The last example is an air gap-coupled type, 3-pole, 0.1-dB Chebyshev ripple bandpass filter with a 2% bandwidth at a center frequency of 49.5 GHz, which was designed in [46] based on a variational technique and fabricated with Teflon dielectric. The ORVIE, of course, can be used to design this kind of NRD-guide filter. In this work, it was used to model the whole filter and to find its frequency characteristics. Fig. 5.10(a) shows the configuration of the gap-coupled NRD-guide filter with geometrical dimensions a=3.5 mm, $d_1=d_2=d_3$=2.7 mm, $l_1=l_4$=1.6 mm and $l_2=l_3$=3.5 mm. Simulated filter response is shown in Fig. 5.10(b), together with measured results [46] for comparison. Agreement between the modeling and measurement results of insertion loss is quite satisfactory. The excess insertion loss was measured and found to be 0.3 dB

whereas that is 0.06 dB in our method and it is more close to the designed value 0.1dB. The return loss in our method is a little shift to low frequency region.

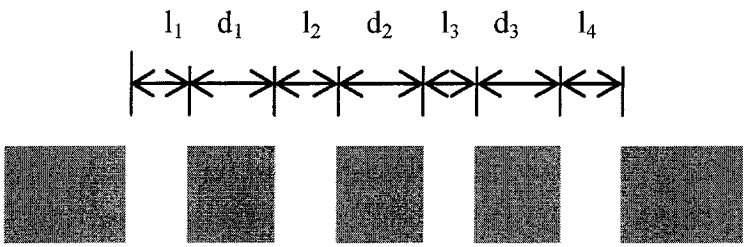

(a)

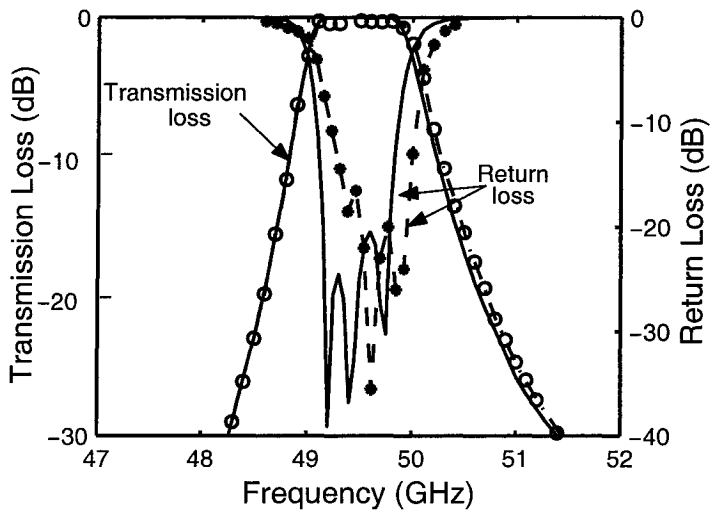

(b)

Fig.5.10. (a) Top view of a 3-pole gap-coupled NRD-guide filter (a=3.5 mm b= 2.7 mm $d_1=d_2=d_3=2.72$ mm. $L_1=l_4=1.60$ mm, $l_2=l_3=3.5$ mm $\varepsilon_r=2.04$). (b) Calculated and measured transmission loss and return loss of the air gap-coupled filter. ORVIE (——). Measured (o, --*--).

5.4 Summary

In this chapter, an order-reduced volume-integral equation approach has been proposed and presented for modeling and analysis of NRD-guide and H-guide millimeter-wave circuits having any shape of section and inhomogeneous dielectric media. By introducing a half-sinusoidal vertical variation of field, the discretization can be made only in the parallel plane. Combined propagating mode and local mode basis functions are used in the Garlerkin's MoM based on the analysis of the mode spectrum in the NRD-guide and H-guide. Vertical integration in space-domain can be carried out analytically and an m=1 Green's function can be constructed. The solution of the volume integral equation for NRD-guide and H-guide circuits has then been reduced to a 2-D planar modeling problem. This method can be applied to the calculation of both resonant frequency and scattering parameter for various dielectric circuits. The framework of the proposed technique was demonstrated through its application to NRD-guide open-end structure. A number of examples include H-guide open-end, resonators, and an air gap-coupled NRD-guide filter have been successfully modeled and also theoretical results compared with other available simulations and measurements.

CHAPTER 6

A GENERALIZED SURFACE-VOLUME INTEGRAL-EQUATION APPROACH FOR ANALYSIS OF HYBRID PLANAR/NRD-GUIDE INTEGRATED CIRCUITS

6.1 Introduction

An ORVIE approach for the modeling and analysis of NRD-guide and H-guide millimeter-wave circuits has been developed in chapter 5. By extending the ORVIE approach to multimode case, a generalized surface-volume integral-equation (SVIE) approach can be established for the analysis of hybrid planar/NRD-guide integrated circuits as discussed in 1.2.4.

In this hybrid structure, not only the m=1 operating mode, but also the m=0 radiation mode and m≥2 evanescent modes may simultaneously be excited in the NRD-guide circuits. The radiation loss can be obtained by extracting the m=0 poles in integrals. The fields in m≥2 evanescent modes are confined in the slot areas and their vicinities for which a reduced calculation region technique can be used. The vertical integrals in the coupling terms between slots and NRD-guide can also be obtained analytically. In most cases, only a few vertical modes are needed and particularly only the diagonal sub-matrices related to the volume integral equation should be calculated due to the orthogonal property between different m modes. These factors largely reduce the calculation effort and make the SVIE approach suitable for modeling and analysis of the hybrid planar/NRD-guide integrated structures with multi-ports NRD-guide circuits. Although this method is effective for parallel plate waveguide circuits, we only consider the NRD guide condition in which the distance between the two plates is less than the half wavelength in this thesis.

In the following, the generalized SVIE approach will be introduced. Then numerical results for several hybrid structures are presented and compared with other results to

demonstrate the effectiveness of this method. Finally, a short summary is given.

6.2 Generalized Surface/Volume Integral Equation Approach

In this section, the formulation of the SVIE system for the hybrid planar/NRD-guide integrated circuits is presented, followed by the current discretization and matrix structure. Afterwards, the analytical evaluation in vertical space-domain integration and first-order Green's functions is outlined in detail. Subsequently, some numerical integration techniques are briefly described.

6.2.1 Surface-volume integral equations for hybrid planar/NRD-guide integrated circuits

Fig. 6.1 shows a generic arrangement of hybrid planar/NRD waveguide circuits with a coordinate system. The space above the upper ground plane ($z>0$) is denoted as region a, the space between the two ground planes ($-d_b<z<0$) as region b, and the space below the downside ground plane ($z<-d_b$) as region c where d_b is the distance between the two ground planes. Three types of circuits, comprising microstrip, coplanar/slotline, and NRD-guide, in five layers are represented as f1, s1, v, s2, f2 from top to bottom. The middle part (v) is a multi-port NRD-guide circuit that is sandwiched between the two parallel infinitely extended metal plates. The feed lines are assumed to be semi-infinitely long with the same height d_b, different width b_l, and constant dielectric permittivity ε_l. The core circuit may be in any shape of NRD guide with the dielectric permittivity ε varies in the x-y plane $\varepsilon(x,y)$. The whole NRD guide circuit is surrounded by a medium with a constant dielectric permittivity ε_s.

By using electric surface currents description, $\mathbf{J}_{f1}$ and $\mathbf{J}_{f2}$, for the microstrip components in f1 and f2, magnetic surface currents, $\mathbf{M}_{s1}$ and $\mathbf{M}_{s2}$, for the slot areas in s1 and s2, and equivalent polarized volume current, $\mathbf{J}_V$, for the NRD guide, five coupled

integral equations are obtained for the five unknown currents $\mathbf{J}_{f1}$, $\mathbf{J}_{f2}$, $\mathbf{M}_{s1}$, $\mathbf{M}_{s2}$ and $\mathbf{J}_v$ by enforcing the boundary conditions: (1) $\mathbf{E}^{\tan}(x,y)=Z(x,y)\cdot\mathbf{J}(x,y)$ on the microstrip circuits f1 and f2, (2) $\mathbf{H}^{\tan}$ is continuous through the slot s1 and s2, and (3) volume equivalent theorem within the area of dielectric regions $\mathbf{J}_v(\mathbf{r})=j\omega(\varepsilon(x,y)-\varepsilon_s)\mathbf{E}(\mathbf{r})$.

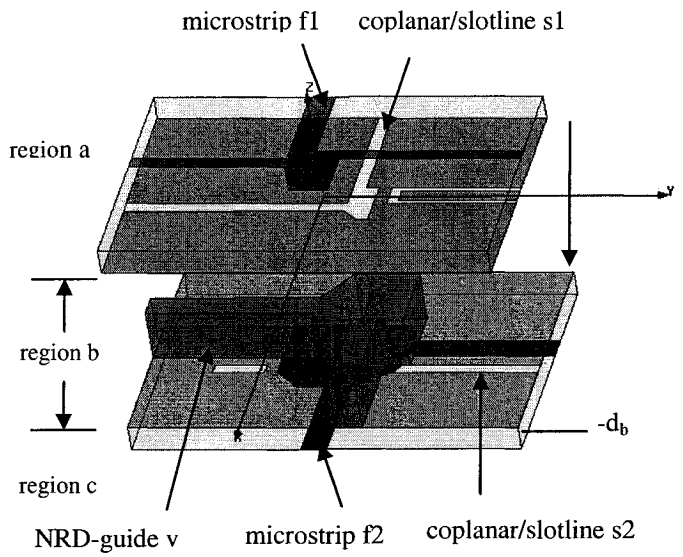

Fig. 6.1. A general arrangement of the hybrid planar/NRD integrated circuits.

$$\mathbf{E}_a^{\tan}(\mathbf{J}_{f1})+\mathbf{E}_a^{\tan}(\mathbf{M}_{s1})-Z(x,y,f1)\cdot\mathbf{J}_{f1}=\mathbf{E}_{a,imp}^{\tan}\quad \mathbf{r}\in f1 \tag{6.1}$$

$$\mathbf{H}_a^{\tan}(\mathbf{J}_{f1})+\mathbf{H}_a^{\tan}(\mathbf{M}_{s1})+\mathbf{H}_b^{\tan}(\mathbf{M}_{s1})-\mathbf{H}_b^{\tan}(\mathbf{J}_v)+\mathbf{H}_b^{\tan}(\mathbf{M}_{s2})=\mathbf{H}_{imp}^{\tan}\quad \mathbf{r}\in s1 \tag{6.2}$$

$$\mathbf{E}_b(\mathbf{J}_v)-\mathbf{E}_b(\mathbf{M}_{s1})-\mathbf{E}_b(\mathbf{M}_{s2})-\frac{1}{j\omega(\varepsilon-\varepsilon_0)}\mathbf{J}_v=\mathbf{E}_{imp}\qquad \mathbf{r}\in v \tag{6.3}$$

$$\mathbf{H}_c^{\tan}(\mathbf{J}_{f2})+\mathbf{H}_c^{\tan}(\mathbf{M}_{s2})+\mathbf{H}_b^{\tan}(\mathbf{M}_s)-\mathbf{H}_b^{\tan}(\mathbf{J}_v)+\mathbf{H}_b^{\tan}(\mathbf{M}_{s1})=\mathbf{H}_{imp}\quad \mathbf{r}\in s2 \tag{6.4}$$

$$\mathbf{E}_c^{\tan}(\mathbf{J}_{f2})+\mathbf{E}_c^{\tan}(\mathbf{M}_{s2})-Z(x,y,f2)\cdot\mathbf{J}_{f2}=\mathbf{E}_{c,imp}^{\tan}\qquad \mathbf{r}\in f2 \tag{6.5}$$

Z(x,y) is a space-varying surface impedance. The right sides are impressed terms and they would generally not appear at the same time. The coupled surface-volume

integral equation (6.1)-(6.5) can be solved with the Galerkin's MoM.

6.2.2 **Current discretization and system matrix structure**

Since the current discretization for electric and magnetic surface currents was discussed in many literatures [97], [122], we will not discuss them in detail in this chapter. Generally, the polarized volume current discretization for the NRD guide circuits should be made in three dimensions and this would make the matrix too large and this method becomes inefficient because of large memory and CPU time requirements. However, in the NRD guide circuits of Fig. 6.1, the presence of the metal plates implies a discretization of the vertical wave number ($\beta_z=m\pi/d_b$, with null or integer m). The total field between the two plates can be represented by the sum of fields in all vertical modes, and the field in each vertical mode varies as a sinusoidal behavior with the propagating constant $m\pi/d_b$ in the vertical direction. The mode spectrum of NRD guide was discussed in section 3.3 and indicates that each m mode spectrum can be divided into a discrete number of surface waves, which are classified into LSE and LSM modes, and a continuous set of radiation modes. The m=0 continuous radiation mode, also referred as parallel plate waveguide mode, will cause radiation loss in this hybrid structure. It is excited by the slots and corresponds to the m=0 pole in the Green's functions. The m=1 is the operating mode in which the continuous mode becomes evanescent at NRD-guide working condition while the LSM_{11} and LSE_{11} are propagating modes. The $m\geq 2$ high order modes are evanescent and confined in the slot areas and their vicinities. The higher order the vertical modes are, the smaller area the field will cover. A reduced calculation region technique can then be used for these higher modes. In this technique, the higher the m value, the smaller calculation region, thus less basis functions are needed. This technique is essential for these structures which need more vertical modes, thus more memory. The current discretization for each m mode can be made only in x-y plane just as planar circuits.

With appropriate basis functions, the overall current can be expressed as:

$$\mathbf{J}_{tot} = \sum_{i=1}^{I} I_i \mathbf{f}_i + \sum_{j=1}^{J} U_j \mathbf{f}_j + \sum_{m=0}^{M} \sum_{k=1}^{K} I_{m,k} \mathbf{f}_{m,k} + \sum_{l=1}^{L} U_l \mathbf{f}_l + \sum_{n=1}^{N} I_n \mathbf{f}_n \tag{6.6}$$

(f1) (s1) (v) (s2) (f2)

where

$$\begin{aligned} \mathbf{f}_{m,k} &= f_{x,k} \cdot \sin\left\langle m\pi \left(z + d_b\right)/d_b \right\rangle \hat{\mathbf{x}} \\ &+ f_{y,k} \cdot \sin\left\langle m\pi \left(z + d_b\right)/d_b \right\rangle \hat{\mathbf{y}} + f_{z,k} \cdot \cos\left\langle m\pi \left(z + d_b\right)/d_b \right\rangle \hat{\mathbf{z}} \end{aligned} \tag{6.7}$$

$\mathbf{f}_i$ and $\mathbf{f}_n$ are the basis functions for planar electric currents in f1 and f2. Similarly, $\mathbf{f}_j$ and $\mathbf{f}_l$ are the basis functions for planar magnetic currents in s1 and s2. $\mathbf{f}_{m,k}$ is the basis function of volume current and $\mathbf{f}_k$ is the planar part of these basis functions. I and N are the total number of planes with planar electric currents in f1 and f2, analogously, J and L for planar magnetic currents in s1 and s2. The total vertical modes is M+1 and K is the total number of planes with planar part of volume current for each m mode and $K = K(m)$.

The discretized integral-equation system is solved with the Galerkin's MoM and a linear system of equations can be obtained as:

$$\begin{bmatrix} [Z_{(f1/f1)}] & [ZY_{(f1/s1)}] & 0 & 0 & 0 \\ [ZY_{(s1/f1)}] & [Y_{s1/s1}] & [ZY_{(s1/v)}] & [Y_{(s1/s2)}] & 0 \\ 0 & [ZY_{(v/s1)}] & [Z_{(v/v)}] & [ZY_{(v/s2)}] & 0 \\ 0 & [Y_{(s2/s1)}] & [ZY_{(s2/v)}] & [Y_{(s2/s2)}] & [ZY_{(s2/f2)}] \\ 0 & 0 & 0 & [ZY_{(f2/s2)}] & [Z_{(f2/f2)}] \end{bmatrix} \cdot \begin{bmatrix} [I_i] \\ [U_j] \\ [I_{m,k}] \\ [U_l] \\ [I_n] \end{bmatrix} = \begin{bmatrix} [U]_{imp} \\ [I]_{imp} \\ [U]_{imp} \\ [I]_{imp} \\ [U]_{imp} \end{bmatrix} \tag{6.8}$$

where $[Z_{(f/f)}]$, $[Z_{(v/v)}]$ are impedance sub-matrices of planar electric currents and volume currents, $[Y_{(s/s)}]$ is an admittance sub-matrices of slot and [ZY] are sub-matrices related to the mutual couplings of magnetic surface currents with electric and volume currents. One of the crucial points of the method lies in the effective and accurate evaluation of the system matrix entries.

For the excitation of the structures, we mainly use traveling-wave excitation technique. This excitation mechanism was first proposed for the analysis of open microstrip gap discontinuities in which the current density flowing at each port is expanded into a superposition of incident and reflected semi-infinite traveling-wave functions and thus the relevant scattering parameters can be directly extracted from reinforcing the boundary condition over the conductor surface [123]. In these cases, the propagation constants and current distribution of different modes in the planar circuits can be obtained with the help of an one-dimensional eigenvalue/eigenvector analysis of the transmission line. This traveling-wave excitation technique was successfully applied in the analysis of multi-ports NRD guide circuits in chapter 5. Since the eigen modes in the NRD guide have exact analytical expressions, this technique is very simple. δ-gap voltage sources in the case of microstrip-like circuits, and δ-gap current sources in the case of coplanar/slotline structures can also be used in the planar circuits. The incident and reflected waves are extracted with the help of reference and test planes by using the prior-known values for the propagation constants from the eigenvalue analysis. Finally, the S-parameters can be determined by exciting an N-port circuit by N linear independent excitations, leading to a linear system of equations for the unknown S-parameters.

Since the couplings between planar electric and magnetic currents are well discussed in literature [97], [124], here we mainly discuss the entries which are related to region b. In the case of two magnetic basis functions in the same plane s1, the matrix entries are

$$Y_{j'j}^{uv}(s1/s1)=\int_{k_x}\int_{k_y}\tilde{G}_{buv}^{HM}(k_x,k_y,0,0)\cdot\tilde{f}_{u,j'}^{*}(k_x,k_y)\cdot\tilde{f}_{v,j}(k_x,k_y)dk_xdk_y \tag{6.9}$$

The other cases of two magnetic basis functions in the same plane s_2 or in different planes s_1 and s_2 are similar to (6.9) and thus omitted here.

The entries related to volume currents can be obtained by spectral-domain integration with the vertical part still in space-domain as follows. The coupling case of a planar magnetic basis function in s1 with a volume basis function in v leads to

$$ZY^{uv}_{j',mk}(s1/v)= \int_{k_x}\int_{k_y}\int_{z'} \tilde{G}^{HJ}_{buv}(k_x,k_y,0,z')\cdot \tilde{f}^{*}_{u,j'}(k_x,k_y)\cdot \tilde{f}_{v,k}(k_x,k_y)\cdot g_{vm}(z')dk_xdk_ydz' \tag{6.10}$$

$$ZY^{uv}_{mk',j}(v/s1)= \int_{k_x}\int_{k_y}\int_{z} \tilde{G}^{EM}_{buv}(k_x,k_y,z,0)\cdot \tilde{f}^{*}_{u,k'}(k_x,k_y)\cdot g_{um'}(z)\cdot \tilde{f}_{v,j}(k_x,k_y)dk_xdk_ydz \tag{6.11}$$

Similarly, the coupling case of a planar magnetic basis function in s2 with a volume basis function in v leads to:

$$ZY^{uv}_{l'mk}(s2/v)= \int_{k_x}\int_{k_y}\int_{z'} \tilde{G}^{HJ}_{buv}(k_x,k_y,-d_b,z')\cdot \tilde{f}^{*}_{u,l'}(k_x,k_y)\cdot \tilde{f}_{v,k}(k_x,k_y)\cdot g_{vm}(z')dk_xdk_ydz' \tag{6.12}$$

$$ZY^{uv}_{mk',l}(v/s2)= \int_{k_x}\int_{k_y}\int_{z} \tilde{G}^{EM}_{buv}(k_x,k_y,z,-d_b)\cdot \tilde{f}^{*}_{u,k'}(k_x,k_y)\cdot g_{um'}(z)\cdot \tilde{f}_{v,l}(k_x,k_y)dk_xdk_ydz \tag{6.13}$$

Finally, in the case of two volume current basis functions, the integral representation

$$Z^{uv}_{mk',mk}(v/v)= \int_{k_x}\int_{k_y}\int_{z}\int_{z'} \tilde{G}^{EJ}_{uv}(k_x,k_y,z,z')\cdot \tilde{f}^{*}_{u,k'}(k_x,k_y)\cdot g_{um'}(z)\cdot \tilde{f}_{v,k}(k_x,k_y)\cdot g_{vm}(z')dk_xdk_ydzdz' - \int_x\int_y\int_z \frac{f_{u,k}(x,y)\cdot g_{um'}(z)\cdot f_{v,k}(x,y)\cdot g_{vm}(z)}{j\omega(\varepsilon(x,y)-\varepsilon_s)}dxdydz\cdot\delta_{uv} \tag{14}$$

Here u or v=x, y, z. $\tilde{f}_v(k_x,k_y)$ is Fourier transforms of the planar basis functions $f_{v,k}(x,y)$. The functions of g_{um} and g_{vm} are $g_{xm}(z)=g_{ym}(z)=\sin\langle m\pi(z+d_b)/d_b\rangle$ and $g_{zm}(z)=\cos\langle m\pi(z+d_b)/d_b\rangle$. An overview of components of the different spectral-domain Green's functions is given in Appendix C. It should be noted that there is always at least one pole which represents the m=0 continuous radiation mode in these Green's functions. The existence of poles makes the integrals in (6.9)-(6.14) more complicated.

6.2.3 **Analytical evaluation in space-domain integration and first-order Green's functions**

The space-domain integrals within (6.10) – (6.14), concerning the variable z and z', can be evaluated analytically with the help of (C.10)-(C.14). The two types of vertical intergrals in (6.10) can be obtained as:

$$IV_s = \int_{-d_b}^{0} dz' \frac{\sin\langle k_2 (z'+d_b)\rangle}{\sin\langle k_2 d_b\rangle} \sin\left\langle \frac{m\pi (z'+d_b)}{d_b} \right\rangle = \frac{m\pi}{d_b} \cdot \frac{(-1)^m}{k_2^2 - (m\pi / d_b)^2} \tag{6.15}$$

$$IV_c = \int_{-d_b}^{0} dz' \frac{\cos\langle k_2 (z'+d_b)\rangle}{k_2 \sin\langle k_2 d_b\rangle} \cos\left\langle \frac{m\pi (z'+d_b)}{d_b} \right\rangle = \frac{(-1)^m}{k_2^2 - (m\pi / d_b)^2} \tag{6.16}$$

For (6.11), only z' has to be changed to z.

The two types of vertical integrals in (6.12) are

$$IV_s' = \int_{-d_b}^{0} dz' \frac{\sin\langle k_2 z'\rangle}{\sin\langle k_2 d_b\rangle} \sin\left\langle \frac{m\pi (z'+d_b)}{d_b} \right\rangle = \frac{m\pi}{d_b} \cdot \frac{1}{k_2^2 - (m\pi / d_b)^2} \tag{6.17}$$

$$IV_c' = \int_{-d_b}^{0} dz' \frac{\cos\langle k_2 z'\rangle}{k_2 \sin\langle k_2 d_b\rangle} \cos\left\langle \frac{m\pi (z'+d_b)}{d_b} \right\rangle = \frac{1}{k_2^2 - (m\pi / d_b)^2} \tag{6.18}$$

Similarly, for (6.13), only z' has to be changed to z.

The vertical integral of (x,x), (x,y), (y,x) and (y,y) components in (6.14) is

$$\begin{aligned} IVV_{ss} &= \int_{-d_b}^{0} dz \cdot \sin\left\langle \frac{m'\pi (z+d_b)}{d_b} \right\rangle \\ &\cdot \left[\frac{\sin\langle k_z z\rangle}{k_z} \int_{-d_b}^{z} \frac{\sin\langle k_z (z'+d_b)\rangle}{\sin\langle k_z d_b\rangle} \sin\left\langle \frac{m\pi (z'+d_b)}{d_b} \right\rangle dz' \right. \\ &\left. + \frac{\sin\langle k_z (z+d_b)\rangle}{\sin\langle k_z d_b\rangle} \int_{z}^{0} \frac{\sin\langle k_z z'\rangle}{k_z} \sin\left\langle \frac{m\pi (z'+d_b)}{d_b} \right\rangle dz' \right] \\ &= \frac{d_b}{2} \cdot \frac{1}{k_z^2 - (m\pi / d_b)^2} \delta(m'-m) \end{aligned} \tag{6.19}$$

The results of the vertical integral of (x,z) and (y,z) components in (6.14) can be obtained by

$$
\begin{aligned}
IVV_{sc} &= \int_{-d_b}^{0} dz \sin\left\langle \frac{m'\pi\left(z+d_b\right)}{d_b} \right\rangle \\
&\cdot\left[\frac{\sin\left\langle k_z\left(z+d_b\right)\right\rangle}{\sin k_z d_b} \int_z^0 \cos k_z z' \cdot \cos\left\langle \frac{m\pi\left(z'+d_b\right)}{d_b} \right\rangle dz' \right. \\
&\left. + \frac{\sin\left\langle k_z z\right\rangle}{\sin k_z d_b} \int_{-d_b}^{z} \cos k_z\left(z'+d_b\right) \cdot \cos\left\langle \frac{m\pi\left(z'+d_b\right)}{d_b} \right\rangle dz' \right] \\
&= \frac{m\pi}{2} \cdot \frac{1}{k_z^2 - \left(m\pi / d_b\right)^2} \delta\left(m'-m\right)
\end{aligned}
\tag{6.20}
$$

Similarly, the results of the vertical integral of (z,x) and (z,y) components in (6.14) can be obtained by

$$
\begin{aligned}
IVV_{cs} &= \int_{-d_b}^{0} dz \cos\left\langle \frac{m'\pi\left(z+d_b\right)}{d_b} \right\rangle \\
&\cdot\left[\cos k_z\left(z+d_b\right) dz \int_z^0 dz' \frac{\sin\left\langle k_z z'\right\rangle}{\sin k_z d_b} \cdot \sin\left\langle \frac{m\pi\left(z'+d_b\right)}{d_b} \right\rangle \right. \\
&\left. + \cos k_z z \int_{-d_b}^{z} \frac{\sin\left\langle k_z\left(z'+d_b\right)\right\rangle}{\sin k_z d_b} \cdot \sin\left\langle \frac{m\pi\left(z'+d_b\right)}{d_b} \right\rangle dz' \right] \\
&= \frac{m\pi}{2} \cdot \frac{1}{k_z^2 - \left(m\pi / d_b\right)^2} \delta\left(m'-m\right)
\end{aligned}
\tag{6.21}
$$

Once again, the results of the vertical integral of (z,z) component in (6.14) can be obtained by

$$
\begin{aligned}
IVV_{cc} &= \int_{-d_b}^{0} dz \cos\left\langle \frac{m'\pi\left(z+d_b\right)}{d_b} \right\rangle \\
&\cdot\left[\frac{\cos\left\langle k_z\left(z+d_b\right)\right\rangle}{\sin k_z d_b} \int_z^0 dz' \frac{\cos\left\langle k_z z'\right\rangle}{k_z} \cdot \cos\left\langle \frac{m\pi\left(z'+d_b\right)}{d_b} \right\rangle \right. \\
&\left. + \frac{\cos\left\langle k_z z\right\rangle}{k_z} \int_{-d_b}^{z} \frac{\cos\left\langle k_z\left(z'+d_b\right)\right\rangle}{\sin k_z d_b} \cdot \cos\left\langle \frac{m\pi\left(z'+d_b\right)}{d_b} \right\rangle dz' \right] \\
&= \frac{d_b}{2} \cdot \frac{1}{k_z^2 - \left(m\pi / d_b\right)^2} \delta\left(m'-m\right)
\end{aligned}
\tag{6.22}
$$

and the results of the vertical integral concerning with source in $\tilde{G}_{bzz}^{EJ}$ in (C-14) can be obtained by

$$\begin{aligned} IVV_1 &= \int_{-d_b}^{0} dz \cos\left\langle m'\pi\left(z+d_b\right)/d_b\right\rangle \cdot \int_{-d_b}^{0} \cos\left\langle m\pi\left(z'+d_b\right)/d_b\right\rangle \cdot \delta\left(z-z'\right)dz' \\ &= \left(d_b/2\right)\cdot\delta\left(m'-m\right) \end{aligned} \tag{6.23}$$

Then, the $\tilde{G}_{bzz}^{EJ}$ component can be simplified by combining the source term (6.23) with the principle term (6.22) and using the separation condition $k_z^2 = k_s^2 - k_x^2 - k_y^2$ as

$$\left(k_x^2+k_y^2\right)\cdot IVV_{cc} + IVV_1 = \frac{d_b}{2}\cdot\frac{\varepsilon_s k_0^2 - \left(m\pi/d_b\right)^2}{\varepsilon_s k_0^2 - k_x^2 - k_y^2 - \left(m\pi/d_b\right)^2}\delta\left(m'-m\right) \tag{6.24}$$

The vertical integral in connection with the second term in (6.14) can be obtained as

$$IV_{ss} = \int_{-a}^{0} \sin\left(m'\pi\left(z+d_b\right)/d_b\right)\cdot\sin\left(m\pi\left(z+d_b\right)/d_b\right)dz = \left(d_b/2\right)\cdot\delta\left(m'-m\right)$$

$$IV_{cc} = \int_{-d_b}^{0} \cos\left(m'\pi\left(z+d_b\right)/d_b\right)\cdot\cos\left(m\pi\left(z+d_b\right)/d_b\right)dz = \left(d_b/2\right)\cdot\delta\left(m'-m\right) \tag{6.25}$$

With the help of (6.15)-(6.24), a set of new Green's functions can be constructed as

$$\tilde{\tilde{\mathbf{G}}}_m^{EM}\left(k_x,k_y,0\right) = \frac{1}{4\pi^2}\cdot\frac{(-1)^m}{T_{em}}\begin{bmatrix} 0 & m\pi/d_b \\ -m\pi/d_b & 0 \\ -jk_y & jk_x \end{bmatrix} \tag{6.26}$$

where $T_{em} = k_s^2 - k_x^2 - k_y^2 - \left(m\pi/d_b\right)^2$. It denotes the m[th] vertical mode electric field contribution in v from the magnetic current in slot s1.

$$\tilde{\tilde{\mathbf{G}}}_m^{HJ}\left(k_x,k_y,0\right) = \frac{1}{4\pi^2}\cdot\frac{(-1)^m}{T_{em}}\begin{bmatrix} 0 & m\pi/d_b & -jk_y \\ -m\pi/d_b & 0 & jk_x \end{bmatrix} \tag{6.27}$$

denotes the magnetic field contribution in slot s1 from the m[th] vertical mode electric volume current in v.

$$\tilde{\tilde{\mathbf{G}}}_m^{EM}\left(k_x,k_y,-d_b\right) = \frac{1}{4\pi^2}\cdot\frac{1}{T_{em}}\begin{bmatrix} 0 & m\pi/d_b \\ -m\pi/d_b & 0 \\ -jk_y & jk_x \end{bmatrix} \tag{6.28}$$

denotes the m[th] vertical mode electric field contribution in v from the magnetic current in slot s2.

$$\tilde{\bar{\mathbf{G}}}_m^{HJ}\left(k_x,k_y,-d_b\right)=\frac{1}{4\pi^2}\cdot\frac{1}{T_{em}}\begin{bmatrix}0 & m\pi/d_b & -jk_y\\ -m\pi/d_b & 0 & jk_x\end{bmatrix} \tag{6.29}$$

denotes the magnetic field contribution in slot s2 from the m[th] vertical mode electric volume current in v.

$$\tilde{\bar{\mathbf{G}}}_{m'm}^{EJ}\left(k_x,k_y\right)=\frac{1}{4\pi^2}\cdot\frac{Z_0}{k_0}\cdot\frac{\delta(m'-m)}{T_{em}}\cdot\begin{bmatrix}j\frac{d_b}{2}\left(k_s^2-k_x^2\right) & -j\frac{d_b}{2}k_xk_y & \frac{m\pi}{2}k_x\\ -j\frac{d_b}{2}k_xk_y & j\frac{d_b}{2}\left(k_s^2-k_y^2\right) & \frac{m\pi}{2}k_y\\ -\frac{m\pi}{2}k_x & -\frac{m\pi}{2}k_y & j\frac{d_b}{2}\left(k_s^2-(m\pi/d_b)^2\right)\end{bmatrix} \tag{6.30}$$

denotes the m'th vertical mode electric field contribution in v from the mth vertical volume current in v.

With the help of Green's functions (6.26)-(6.30), the integrals in (6.10)-(6.14) can be written in planar form:

$$ZY_{j'mk}^{uv}\left(s1/v\right)=\int_{k_x}\int_{k_y}\tilde{G}_{m,uv}^{HJ}\left(k_x,k_y,0\right)\cdot\tilde{f}_{u,j'}^{*}\left(k_x,k_y\right)\cdot\tilde{f}_{v,k}\left(k_x,k_y\right)dk_xdk_y \tag{6.31}$$

$$ZY_{mk',j}^{uv}\left(v/s1\right)=\int_{k_x}\int_{k_y}\tilde{G}_{m,uv}^{EM}\left(k_x,k_y,0\right)\cdot\tilde{f}_{u,k'}^{*}\left(k_x,k_y\right)\cdot\tilde{f}_{v,j}\left(k_x,k_y\right)dk_xdk_y \tag{6.32}$$

$$ZY_{l'mk}^{uv}\left(s2/v\right)=\int_{k_x}\int_{k_y}\tilde{G}_{m,uv}^{HJ}\left(k_x,k_y,-d_b\right)\cdot\tilde{f}_{u,l'}^{*}\left(k_x,k_y\right)\cdot\tilde{f}_{v,k}\left(k_x,k_y\right)dk_xdk_y \tag{6.33}$$

$$ZY_{mk'l}^{uv}\left(v/s2\right)=\int_{k_x}\int_{k_y}\tilde{G}_{m,uv}^{EM}\left(k_x,k_y,-d_b\right)\cdot\tilde{f}_{u,k'}^{*}\left(k_x,k_y\right)\cdot\tilde{f}_{v,l}\left(k_x,k_y\right)dk_xdk_y \tag{6.34}$$

$$\begin{aligned}Z_{mk',mk}^{uv}\left(v/v\right)&=\int_{k_x}\int_{k_y}\tilde{G}_{m'm,uv}^{EJ}\left(k_x,k_y\right)\cdot\tilde{f}_{u,k'}^{*}\left(k_x,k_y\right)\cdot\tilde{f}_{v,k}\left(k_x,k_y\right)dk_xdk_y\\&+\frac{a}{2}\cdot\int_x\int_y\frac{f_{u,k'}(x,y)\cdot f_{v,k}(x,y)}{j\omega\left(\varepsilon(x,y)-\varepsilon_s\right)}dxdy\cdot\delta_{uv}\end{aligned} \tag{6.35}$$

The Green's functions in (6.26)-(6.30) are much simpler than those in (C.10)-(C.14) without triangular functions in them. The $\hat{z}\hat{z}$ component of G in the square bracket

(C.14) is greatly simplified as a constant. The ever-existing m=0 pole is eliminated through the vertical integrations (6.15)-(6.23) for m≥1 modes. The m=0 radiation loss is obtained only through extracting poles in m=0 integrals. Since each new Green's function only governs the m^{th} vertical mode case for NRD guide circuits, we call them as first-order Green's functions and refer to (C.10)-(C.14) as the full-scale Green's functions. Due to the orthogonal properties between different m modes as shown in (6.30), only the $m' = m$ elements in (6.35) need to be calculated and this largely reduces the computational effort. The integrals in (6.31)-(6.35) are two-dimensional (2-D) in the spectral-domain with respect to k_x and k_y just same as in planar circuits. With the 2-D discretization technique, the solution of each vertical mode for NRD guide circuits has been reduced to a completely 2-D planar problem. We call this method as the generalized surface-volume integral-equation (SVIE) method.

6.2.4 **Numerical integration**

The integrals in (6.31)-(6.35) are similar to those used in planar circuits but much simpler because of the simple first-order Green's functions. Many kinds of planar basis function such as piecewise sinusoidal functions, pulse basis functions with rectangular or triangular mesh scheme or entire domain mode can be used to fit different cross sections of the NRD guide circuits just as used in planar circuits.

Since there are no poles in these m≥1 integrals, they can be carried out either in polar coordinates or in rectangular coordinates. In most cases of planar basis functions in the NRD guide circuit, integrands $\tilde{f}_i^*\left(k_x,k_y\right)\cdot\tilde{f}_j\left(k_x,k_y\right)$ and $\tilde{f}_i^*\left(k_x,k_y\right)\cdot\tilde{f}_p\left(k_x,k_y\right)$ can be rearranged as $g\left(k_x\right)\cdot h\left(k_y\right)$ which oscillates with a sinusoidal behavior. So the integrals in rectangular coordinates are more efficient than their polar counterpart.

The m=0 integrals must be carried out in polar coordinates due to the existence of the poles. However, only $\hat{z}\hat{z}$ component needs to be calculated because only z-directed polarized volume current exists in m=0 mode.

The asymptotic subtraction technique can be used for these numerical integrations both in polar coordinate as in [97] and rectangular coordinates as in 5.3.1. The symmetric property and redundancy reduction techniques can also be used to reduce calculation effort in this method.

6.3 Numerical Results and Discussion

Several examples are discussed in this section to demonstrate properties and efficiency of the proposed method. The examples comprise different structures and field distributions starting from the simplest case in which only M=1 vertical modes are needed to the most complicated case in which up to M=12 vertical modes are required. The piecewise sinusoidal expansion functions are used to model the higher order modes in the vicinity of slots and open-circuited stub discontinuities for the surface electric current in the microstrip line. The incident, reflected, and transmitted waves are represented by traveling wave modes corresponding to the fundamental microstrip mode as in [123]. Entire domain sinusoidal expansions are used for the magnetic surface current in the slot as in [125].

6.3.1 Microstrip-Coupled NRD Resonators

The hybrid planar/NRD oscillator, which was proposed and studied in [60], [67], is an important active circuit with the hybrid integration technology. In this example, a microstrip-coupled NRD resonator as shown in Fig. 6.2 is studied. The microstrip circuits are made with a thickness of 15 mil substrate (RT/Duroid 5880 and ε_r=2.3). The dimensions of the NRD resonator are 7.12×12.88×13.55 mm^3 with ε_r=2.04. The two coupling apertures have dimensions of 5×0.5 mm^2 with a spacing of 15 mm. Pulse basis functions are used for the NRD resonator. The transmission loss and phase of S_{21} for the number of vertical modes with a frequency range of 16.9-17.1 GHz was calculated and shown in Fig. 6.3. It shows that M=1 is enough in this structure because the fields in

m≥2 modes are very small in dielectric region since the slots do not touch the dielectric. The field distribution at 16.98 GHz is shown in Fig. 6.4 in which the field magnitude in m=2 mode is over 40 times smaller than that in m=1 mode. The results from commercial software Ansoft-HFSS is also described in Fig. 6.3 for comparison and shows that they agree with each other.

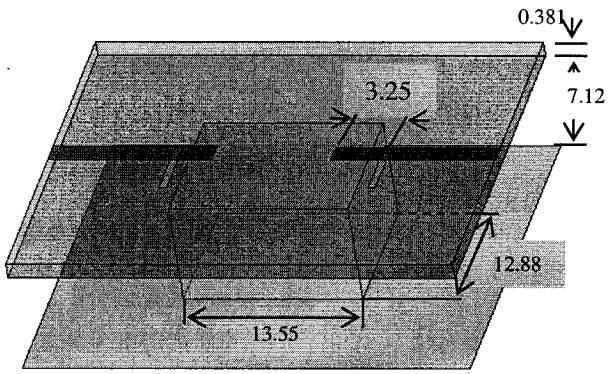

Fig. 6.2. Structure of microstrip-coupled NRD resonator.

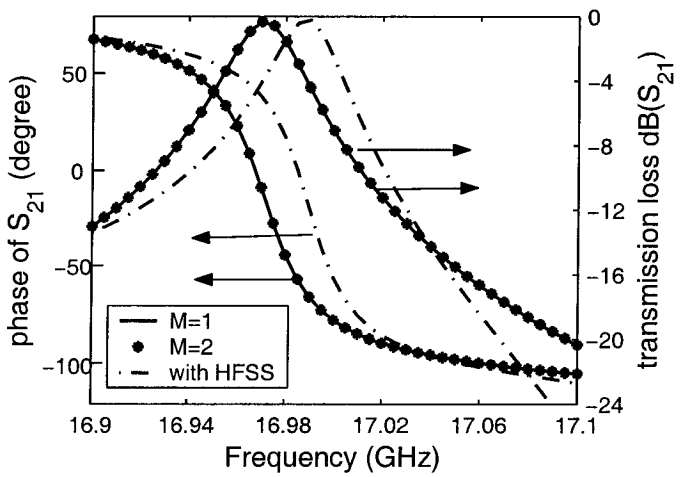

Fig. 6.3. The magnitude and phase of S_{21} with this method and HFSS.

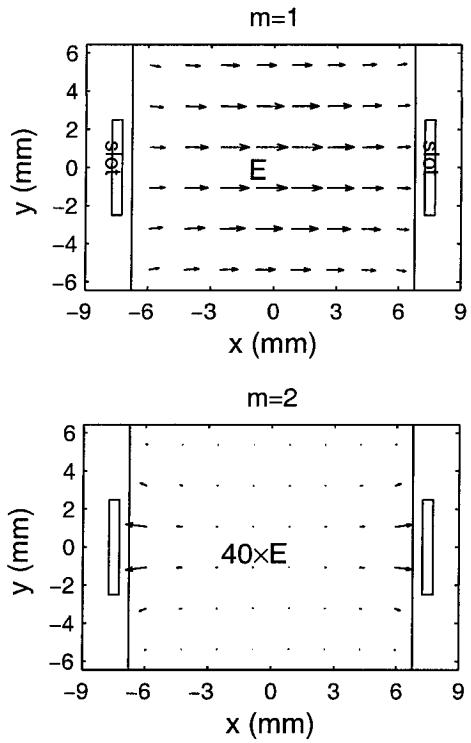

(b)

Fig. 6.4. Field distributions of microstrip-coupled NRD-guide resonator.

6.3.2 NRD interconnect between planar circuits

The second example is an NRD guide interconnect between microstrip lines which are located on the opposite sides of this hybrid structure, first investigated by a transmission line method in [126]. The geometry of this interconnect directly between two slots with dimensions of 1.5×8 mm^2 is shown in Fig. 6.5. The dimensions of the NRD guide are 12.7×12×12 mm^3 which has been realized using a substrate with a dielectric constant close to that of silicon (ε_r=12). The microstrip line has been implemented on Teflon substrate (ε_r=2.52) with an open stub of 8 mm. The convergence of coupling coefficient $|S_{21}|$ between the microstrip lines and NRD guide for vertical modes is shown in Fig. 6.6. Up to M=12 vertical modes are needed to make the

calculation convergent because the fields of high modes are concentrated between the two slots in this structure. The reduced calculation region technique is used and it is essential for modeling this structure with more vertical modes. The calculation regions

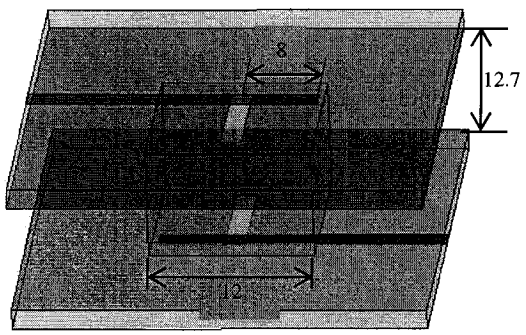

Fig. 6.5. Structure of an NRD interconnect between planar circuits.

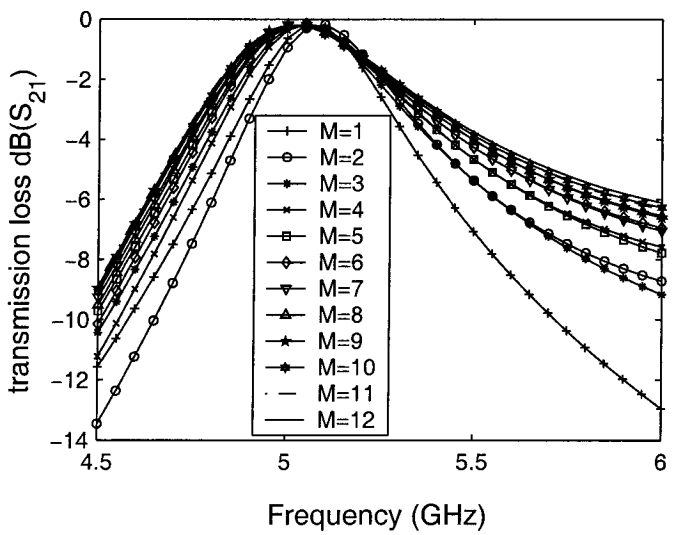

Fig. 6.6. Frequency characteristic of the NRD interconnect between planar circuits with the different number of vertical modes.

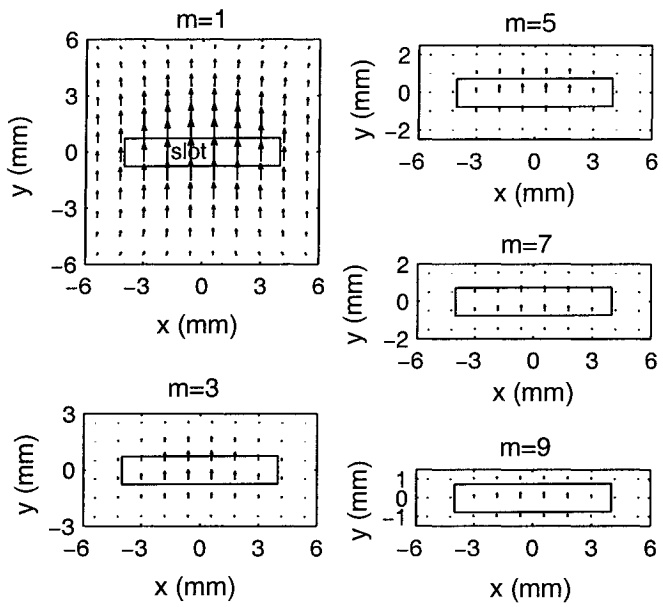

Fig. 6.7. Field distributions of the NRD interconnect between planar circuits in m = 1, 3, 5, 7, 9 vertical modes.

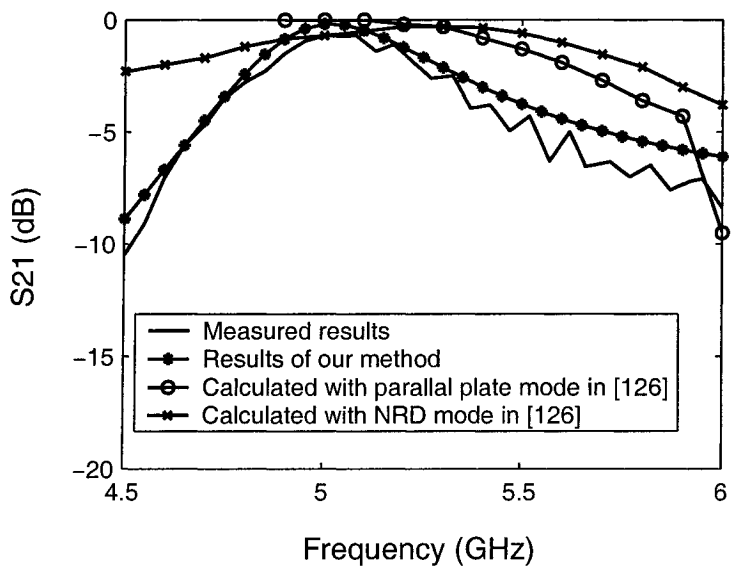

Fig. 6.8. S-parameters of the NRD interconnect between planar circuits.

and field distributions of m = 1, 3, 5, 7, 9 modes at 4.7 GHz are shown in Fig. 6.7 and indicates that the field magnitude of the higher m modes decreases slowly as m increases. The agreement of our approach with measurements is better than the results of transmission line method as shown in Fig. 6.8.

6.3.3 Integrated transition of microstrip-line-to NRD-guide structures

The last example is the microstrip-to-NRD transition structure, which was studied in [19], [20]. The microstrip line is placed in the perpendicular direction to the dielectric strip of the NRD-guide and the integrated transition is made through a magnetic aperture coupling. In the microstrip-line-to-NRD-guide transition as shown in Fig. 6.9, a microstrip line with width of 1.52 mm is fabricated on a substrate (RT/Duroid 5880, ε_r=2.3) with a thickness of 20 mil. The NRD guide is made of a rectangular dielectric strip (Rogers TMM-3, ε_r=3.27) with an open stub of 2.79 mm and designed to operate around 20 GHz with d_b=6.1 mm and W_v=6.5 mm. The coupling aperture on the common ground plane is a narrow rectangular slot with dimensions of 7.5×0.5 mm^2. Only LSM_{11} surface wave, which can be represented by propagating mode basis function, can be excited in this structure in the case of a microstrip excitation, or an NRD guide excitation

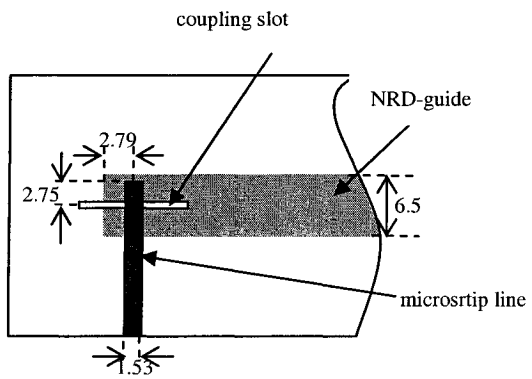

Fig. 6.9. Top view of the microstrip-line-to-NRD-guide transition.

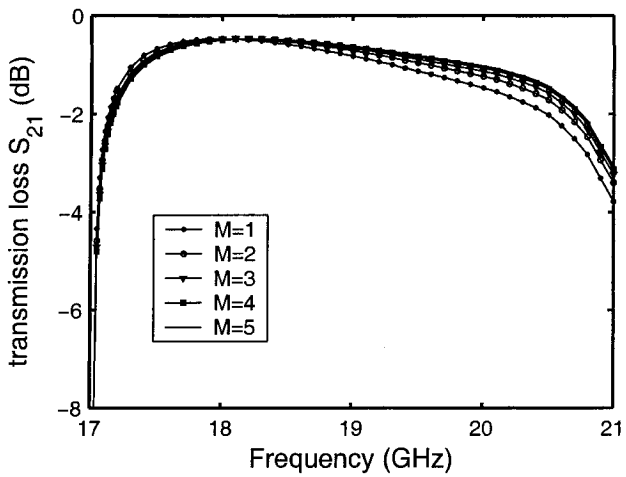

Fig. 6.10. Frequency characteristics of the microstrip-line-to-NRD-guide coupling structure with different number of vertical modes.

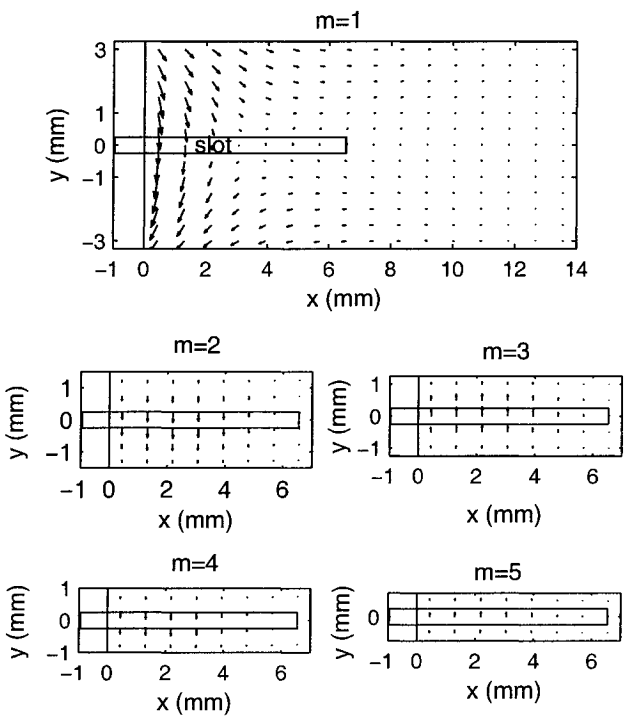

Fig. 6.11. Field distributions in m = 1, 2, 3, 4, 5 vertical modes.

with LSM_{11} mode and this has been strictly proven in Appendix D. The fields of evanescent modes are represented by pulse basis functions. The reduced calculation region technique is again used in this example.

The structure is simulated with a frequency sweep between 17.03 GHz (cutoff frequency of LSM_{11} mode in the NRD guide) and 21GHz. The convergence of transmission loss $|S_{21}|$ with the number of vertical modes is shown in Fig. 6.10. It can be seen that M=5 is accurate enough for the whole frequency band. The calculation regions and field distributions of m=1, 2, 3, 4, 5 modes at 20 GHz are shown in Fig. 6.11. In the experimental prototype, two identical microstrip-line-to-NRD-guide transitions are used as in Fig. 6.12, which are interconnected through an NRD-guide terminated with two open ends having a length of 82 mm. The distance between the two microstrip feed lines is 76.42 mm. Figure 6.13 shows the measured frequency response of $|S_{21}|$ with the modeling result for the whole structure. The higher loss in the measurement comes mainly from the dielectric loss in the NRD-guide and a mechanic-related matching problem in the slot. The ripples come from the resonator effect in the finite NRD guide because of mismatching. The agreement between simulated and measured results indicates that our approach is effective for modeling such complex transition structures.

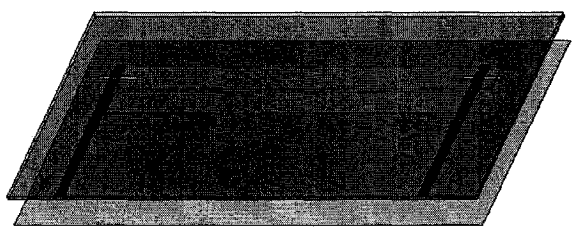

Fig. 6.12. Transparent view of two interconnected transitions of microstrip-line-to-NRD-guide through a length of NRD-guide.

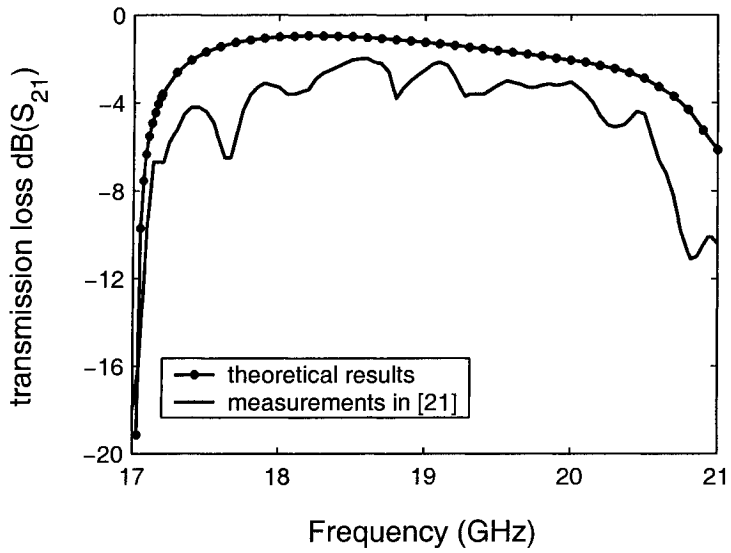

Fig. 6.13. Frequency response comparing with the theoretical and measured data in [21] for the two interconnected transitions.

Apparently, this method is attractive for structures in which a small number of vertical modes are required (M≤5). However, for structures that needs more vertical modes such as the second example, other methods such as FEM, FDTD and TLM, also need a dense discretization grid to model them accurately because the fields change abruptly in the structures. In our method, the use of reduced calculation region technique largely reduced the basis functions required in large vertical modes, thus it is also attractive for structures with more vertical modes. Compared to commercial software packages such as Ansoft-HFSS, this method not only needs less memory and short CPU time, but also can provide more information about the structures, such as field distribution with respect to each vertical mode.

6.4 Summary

A generalized SVIE approach was proposed and developed for accurate modeling and analysis of the hybrid planar/NRD integrated circuits. By using vertical modes in the

basis functions, vertical integration in space-domain can be carried out analytically and a set of first-order Green's function can be constructed. In each mode, the solution of volume integration concerning with the NRD guide circuits has been reduced to a 2-D planar problem.

There are several advantages with this method:

a. There are no poles in the $m \geq 1$ integrals under the NRD guide condition. The integrals may be carried out in rectangular coordinate with a fast convergence due to its sinusoidal oscillating behavior. The radiation loss can be obtained by extracting $m=0$ poles in $m=0$ integrals.

b. Only the diagonal sub-matrices related to the volume integral equation are needed and calculated due to the orthogonal property of different vertical modes.

c. Fields in $m \geq 2$ vertical modes are confined in the slot areas and their vicinities, and a reduced calculation region technique can effectively be used.

d. Different numbers of the vertical modes are needed in different structures. In most cases, only a few vertical modes are needed.

The overall computational effort could be drastically reduced due to the above advantages and this makes the proposed approach suitable for the planar/NRD-guide hybrid circuits. The usefulness and potential applications of the proposed method are demonstrated through three distinct circuits in the hybrid technology.

CHAPTER 7

CONCLUSIONS AND FUTURE WORK

7.1 Conclusions

NRD-guides play an important role in millimeter-wave circuits due to their low transmission loss and non-radiative properties in bends and discontinuities. Since their inception, the NRD based millimeter-wave circuits have experienced tremendous growth with reference to the modified NRD-guides, the NRD-guide circuits and the hybrid planar/NRD-guide integrated circuits areas. However, numerical techniques developed for NRD-guide based circuits are either too specific for some particular circuits or need more CPU time and memory. In this work, a set of integral equation techniques has been developed for the analysis of NRD-guide based millimeter-wave circuits.

Chapter 2 has presented the basic theory of integral equation technique. Integral equations, including surface integral equations and volume integral equations, are formulated by employing an equivalence principle and enforcing a boundary condition. The dyadic Green's functions of homogeneous medium and multilayered media were derived in both spatial and spectral space. The MoM was introduced as a discretization scheme for integral equations and the method of point matching, least squares, and Galerkin's method were considered as three special cases. Different categories of basis functions and their properties were discussed.

Chapter 3 has discussed the guided wave properties of the standard NRD-guide and H-guide. Eigen modes in the dielectric strip loaded parallel plate guide can be divided into a discrete number of surface-waves, which are classified into LSE and LSM modes, and a continuous set of radiation modes. The field expressions of the LSM and LSE modes, including symmetric mode and anti-symmetric modes, have been obtained analytically. The mode spectrum of dielectric strip loaded parallel-plate was described with a set of spectrum figures in which the space of the mode spectrum is divided into

surface wave modes, continuous radiation modes, and prohibited regions. The m=0 propagating radiation mode can exist over all frequency range and may cause leakage mode in modified NRD-guides and radiation loss in hybrid planar/NRD-guide circuits. The m=1 continuous radiation mode becomes completely evanescent in the $a/\lambda_0<0.5$ and partly evanescent and partly propagating in the $a/\lambda_0>0.5$ region. The coupling mechanism between two parallel NRD-guides is due to the interaction of exponentially decaying fields and thus the coupling is sensitive to the spacing and the length of the coupler.

Chapter 4 has investigated integral equation solution to the guidance and leakage properties of modified NRD-guides. The electric field integral equation for dielectric waveguides in multilayered media was formulated and solved with Garlerkin's method of moments for a general modified NRD-guide. The propagation constants were calculated by setting the determinant of the impedance matrix to zero. The condition of bounded mode and leakage mode has been discussed in a simplified modified NRD-guide without overlays and an asymptotic technique was use to speed up the numerical integration. A bridged NRD-guide coupler in which a thin dielectric strip is used to connect the coupled parallel NRD-guides was proposed and the propagation constants and electrical characteristics were calculated through the EFIE method. The coupling coefficient of the new coupler is largely enhanced by optimizing the thickness of the bridge. The existence of the bridge yields a monolithic structure and makes it easy to control the spacing of the coupler. Compared to the conventional NRD guide coupler, the bridged NRD-guide coupler is much more compact and broadband, which are critical for millimeter-wave integrated circuits. Experimental prototypes are fabricated with two 90° elbow bends that are used for arms and the bridge-connected coupler section is terminated at both ends by tapered half-circle sections. A calibration procedure is used to remove mismatch effects between the NRD-guide and the rectangular waveguide in the measured results. The experimental results have confirmed our analysis and they have shown that this type of coupler is useful in millimeter-wave systems.

Chapter 5 has developed an order-reduced volume-integral equation approach for the modeling and analysis of NRD-guide and H-guide circuits having any shape of section and inhomogeneous dielectric media. With m=1 vertical mode excitation, only m=1 modes, including surface wave modes and a continuous radiation wave mode, appear in the circuits due to the orthogonal properties between different m modes. Thus a half-sinusoidal vertical variation of fields ($\sin(\pi(z+a)/a)$ in x, y components and $\cos(\pi(z+a)/a)$ in z component) remains unchanged over the entire circuits and the current discretization can be made only in the parallel plane. The propagating surface-wave modes can be used as propagating mode basis functions in the feed lines and the remained field can be represented with local mode basis functions which can be either entire mode or sub-sectional mode. Combined propagating mode and local mode basis functions are used in the Garlerkin's method of moments while only local modes are used as test functions. The system matrix entries can be obtained by a spectral-domain integration with the vertical part still in space-domain. A new m=1 Green's function was constructed by carrying out the vertical integration in space-domain analytically. Finally, the solution of the volume integral equation for NRD-guide and H-guide circuits was reduced to a 2-D planar modeling problem. This approach can be applied for calculating the characteristics of various waveguide components and multiport circuits such as resonant frequencies and S-parameters. The framework of the proposed technique was demonstrated through its application to NRD-guide open-end structure. In addition, other examples including H-guide open-end, resonators, and an air gap-coupled NRD-guide filter were also successfully modeled and theoretical results were verified by comparing with other available simulations and measurements.

Chapter 6 has established a generalized surface-volume integral-equation approach for accurate modeling and analysis of the hybrid planar/NRD-guide integrated circuits. With the excitation of equivalent magnetic current from the slots in metal plates, not only the m=1 operating mode, but also the m=0 radiation mode and $m\geq 2$ evanescent modes were excited simultaneously. By extending the ORVIE method to the multi-mode case in the NRD-strip, the solution of the volume integral-equation concerning with the NRD-guide

circuits has been reduced to a 2-D planar problem in connection with each vertical mode. In this way, only the diagonal sub-matrices need to be calculated due to the orthogonal property of different vertical modes. A reduced calculation region technique was used for the high vertical modes in which the fields are confined in the slot areas and their vicinities. Generally, only a few vertical modes are needed in the hybrid structures. In this condition, the poles only exist in m=0 first order Green's function which represent the m=0 radiation mode. The radiation loss can be obtained by extracting m=0 poles in m=0 integrals. Since there are no poles in the integrals for m≥1 modes, they may be carried out in rectangular coordinate with fast convergence due to its sinusoidal oscillating behavior. The overall computational effort could be drastically reduced comparing the conventional SVIE method and this makes the proposed approach very effective for planar/NRD-guide hybrid circuits. The usefulness and potential applications of the proposed method were demonstrated through three distinct circuits in the hybrid technology. In the microstrip-coupled NRD-guide resonators, only two vertical modes (M=1) are required since the slots do not touch the dielectric which makes the field in m≥2 modes very small in dielectric region. However, up to thirteen vertical modes (M=12) are needed to make the calculation convergent because the fields in high modes are concentrated between the two slots in NRD interconnect between planar circuits. Generally, M=5 is accurate enough for the whole frequency band in the integrated transition of microstrip-line-to NRD-guide structures. These numerical results are in good agreement with measured results or the results obtained with other methods.

7.2 **Future work**

The work presented in this thesis can be extended in many ways. The system matrix entries can be carried out in space domain instead of spectral domain as in this thesis. In this way, the type of the sub-domain of basis functions is flexible and it suitable for objects with irregular shapes. However, the DGF in the integral equations does not have a closed form and have to be obtained from a Sommerfeld-type integral. Since there

are no poles in first-order Green's functions of the $m \geq 1$ mode, the singularities in the Sommerfeld-type integral were removed and made the evaluation of the integrals more promising. In the hybrid planar/NRD-guide integrated circuits, the kernel in the Sommerfeld-type integral related to planar circuits is still highly singular. The evaluation of the integrals in the moment method procedure is difficult when the observation point is within the integration range. The mixed potential integral equation (MPIE), which is a modification of the EFIE, is usually solved in the space domain. In comparison with the EFIE in the space domain, the kernel in the MPIE is less singular, which makes the evaluation of integrals more numerically simple and stable for two nearby elements.

Recently, a new substrate integrated circuits (SICs) which include substrate integrated rectangular waveguide (SIRW) and substrate integrated NRD-guide (SINRD) was proposed for establishing a robust framework for millimeter-wave circuit design. In this technology, non-planar waveguides are synthesized and transformed into planar form, thus allowing a complete single substrate planar integration of usually hybrid planar and non-planar circuits and components. The proposed ORVIE approach can be used for modeling and analyzing properties of the SIRW/SINRD guide structures by extending this method to both equivalent volume currents in the air holes of SINRD guide and surface currents in the posts of SIRW guide. Furthermore, the generalized SVEI approach can be used for the analysis of hybrid planar/SINRD-guide integrated circuits.

REFERENCES:

[1] E. C. Niehenke, R. A. Pucel, and I. J. Bahl, "Microwave and millimeter-wave integrated circuits," *IEEE Trans. Microwave Theory Tech.* vol. 50, pp. 846-857,Mar. 2002.

[2] H. H. Meinel, "Commercial applications of millimeter-waves history, present status, and future trends," *IEEE Trans. Microwave Theory Tech.* vol. 43, pp. 1639-1653, July, 1995.

[3] S. J. Fiedziuszko, I. C. Hunter, T. Itoh, Y. Kobayashi, T. Nishikawa, S. N. Sitzer, and K. Wakino, "Dielectric materials, devices, and circuits," *IEEE Trans. Microwave Theory Tech.* vol. 50, pp. 706-720, Mar. 2002.

[4] S. K. Koul, "*Millimeter wave and optical dielectric integrated guides and circuits*," A wiley-interscience publication, John wiley & sons, Inc. 1997.

[5] T. Yoneyama and S. Nishida, " Nonradiative dielectric waveguide for millimeter-wave integrated circuits," *IEEE Trans. Microwave Theory Tech.*, vol. 29, pp. 1188-1192, Nov. 1981.

[6] T. Yoneyama and S. Nishida, "Nonradiative dielectric waveguide circuit components," *Int. Journal of infrared and Millimeter Waves*, vol. 4, No. 3, pp. 439-449, May 1983.

[7] _____, "Nonradiative dielectric waveguide," in *Infrared and Millimeter Wave.* New York: Academic, vol. 11, ch. 2, pp. 61-98, 1984.

[8] F. Furoki and T. Yoneyama, "Nonradiative dielectric waveguide circuit components using beam-lead diodes," *Electronics and Communications in Japan*, vol. 73, no. 9, pt. 2, pp. 35-40, 1990.

[9] T. Yoneyama, "Millimeter wave integrated circuits using nonradiative dielectric waveguide," *Electron. Commun.*, vol. 74, pt. 2, no. 2, pp. 87-94, 1991.

[10] _____, "Recent development in NRD-guide technology," *Ann. Télécommun.*, vol. 47, nos. 11-12, pp. 508-514, 1992.

[11] F. Kuroki and T. Yoneyama, "NRD guide digital transceivers for millimeter wave LAN system," *IEICE trans. Commun.* Vol. E79-B, no. 12, pp. 1759-1764, 1996.

[12] T. Yoneyama, "Properties of guided wave and leaky waves in NRD-guide," in *Proc. of Asia-Pacific Microwave Conf.*, Yokohama, Japan, vol. 1, pp. 257-264, Dec. 1998.

[13] J. H. C. van Heuven, "A new integrated waveguide-microstrip transition," *IEEE Trans. Microwave Theory Tech.*, vol. 24, pp. 144-147, Mar. 1976.

[14] S. Moochalla and C. An, "Ridge waveguide used in microstrip transition," *Microwaves RF*, pp. 149-152, Mar. 1984.

[15] T. Ho and Y. Shih, "Spectral domain analysis of E-plane waveguide to microstrip transitions," *IEEE Trans. Microwave Theory Tech.*, vol. 37, pp. 388-392, Feb. 1989.

[16] W. Grabherr, B. Huber, and W. Menzel, "Microstrip to waveguide transition compatible with mm-wave integrated circuits," *IEEE Trans. Microwave Theory Tech.*, vol. 42, pp. 1842-1843, Sept. 1994.

[17] L. T. Hildebrand and J. Joubert, "Full-wave analysis of a new microstrip-to-waveguide interconnect configuration," *IEEE Trans. Microwave Theory Tech.*, vol. 48, pp. 1-7, Jan. 2000.

[18] J. Miao and T. Itoh, "Coupling between microstrip line and image guide through small apertures in the common ground plane," *IEEE Trans. Microwave Theory Tech.*, vol. 31, pp. 361-363, April, 1983.

[19] L. Han, K. Wu, and R. G. Bosisio, "An integrated transition of microwave to nonradiative dielectric waveguide for microwave and millimeter-wave circuits," *IEEE Trans. Microwave Theory Tech.*, vol. 44, pp. 1091-1096, July 1996.

[20] K. Wu and L. Han, "Hybrid integration technology of planar circuits and NRD-guide for cost-effective microwave and millimeter-wave applications," *IEEE Trans. Microwave Theory Tech.*, vol. 45, pp. 946-954, June 1997.

[21] J. Tang, K. Wu, "Co-layered integration and interconnect design platforms of planar circuit and nonradiative dielectric (NRD) waveguide," *IEEE Trans. Microwave Theory Tech.*, vol. 48, pp. 519-524, April 2000.

[22] K. Wu, "Integration and interconnect techniques of planar and non-planar structures for microwave and millimeter-wave circuits status and future trend", *in Proc. of Asia-Pacific Microwave Conf.*, Taipei, C. O. P., pp. 411-416, June, 2001.

[23] B. Ghosh, "Modal and TLM-based analyses of discontinuities in the non-radiating dielectric waveguide and components," Ph. D. thesis, Department of Electrical and Computer Engineering, The University of Monitoba, 2002.

[24] T. Yoneyama, S. Fujita, and S. Nishida, "Insulated nonradiative dielectric waveguide for millimeter-wave integrated circuits," *IEEE Trans. Microwave Theory Tech.*, vol. 31, pp. 1002-1008, Dec. 1983.

[25] W. X. Zhang and L. Zhu, "New leaky-wave antenna for millimeter-wave constructed from groove NRD waveguide," *Electron. Lett.*, vol. 23, pp. 1191-1192, Oct. 1987.

[26] L. Zhu and W. X. Zhang, "The bandwidth of single-mode operation in groove NRD waveguide," *Int. Journal of infrared & Millimeter Waves*, vol. 10, no. 3, pp. 371-379, Oct. 1989.

[27] C. E. Tong and R. Blundell, "Study of groove nonradiating dielectric waveguide," *Electron. Lett.* Vol. 25, pp. 934-936, July, 1989.

[28] K. Wu, J. Dallaire, and F. Boone, "Channelized nonradiative-dielectric (NRD) guide for hybrid and monolithic integration technology," *in Proc. of Asia-Pacific Microwave Conf.* Yokohama, Japan, 1998, pp. 265-268, Dec. 1998.

[29] J. Dallaire and K. Wu, "Complete characterization of transmission losses in generalized nonradiative dielectric (NRD) waveguide," *IEEE Trans. Microwave Theory Tech.*, vol 48, pp. 121-125, Jan. 2000.

[30] A. A. Oliner, S. T. Peng and K. M. Sheng, "Leakage from a gap in NRD guide," in *IEEE MTT-S Int. Microwave Symp. Dig.*, St. Louis, USA, pp. 619-622, June 1985.

[31] Y. Cassivi, D. Deslandes, and K. Wu, "Engraved NRD-guide for millimeter-wave integrated circuits," in *IEEE MTT-S Int. Microwave Symp. Dig.*, Boston, MA, pp. 605-608, June, 2000.

[32] Y. Cassivi, D. Deslandes, and K. Wu, "Design considerations of engraved NRD guide for millimeter-wave integrated circuits," *IEEE Trans. Microwave Theory Tech.*, vol. 50, pp. 165-171, Jan. 2002.

[33] A. L. Topa, C. R. paiva, and A. M. barbosa, "Full-wave analysis of a nonradiative dielectric waveguide with a pseudochiral Ω-slab," *IEEE Trans. Microwave Theory Tech.*, vol. 46, pp. 1263-1269, Sept. 1998.

[34] T. Yoneyama, M. Yamaguchi, and S. Nishida, "Bends in nonradiative dielectric waveguides," *IEEE Trans. Microwave Theory Tech.*, vol. 30, pp. 2146-2150, Dec. 1982.

[35] T. Yoneyama, H. Tamaki, and S. Nishida, "Analysis and measurements of nonradiative dielectric waveguide bends," *IEEE Trans. Microwave Theory Tech.*, vol. 34, pp. 876-882, Aug. 1986.

[36] H. Sawada, T. Yoneyama, and F. Kuroki, "Size reduction of NRD-guide bend," in *Proc. of Asia-Pacific Microwave Conf.*, Seoul, Korea, pp. 1450-1453, Nov., 2003.

[37] F. Boone and K. Wu, "Mode conversion and design consideration of integrated nonradiative dielectric (NRD) components and discontinuities," *IEEE Trans. Microwave Theory Tech.*, vol. 48, pp. 482-492, April 2000.

[38] J. A. G. Malherbe, J. H. Cloete, and I. E. Losch, "A transition from rectangular to nonradiating dielectric waveguide," *IEEE Trans. Microwave Theory Tech.*, vol. 33, pp. 539-543, June 1985.

[39] T. Yoneyama and S. Nishida, "Nonradiative dielectric waveguide T-junctions for millimeter-wave applications," *IEEE Trans. Microwave Theory Tech.*, vol. 33, pp. 1239-1241, Nov. 1985.

[40] F. Boone and K. Wu, "Full-wave modal analysis of NRD guide T-junction," *IEEE Microwave guided wave lett.*, vol. 10, pp. 228-230, June 2000.

[41] F. Boone and K. Wu, "Nonradiative Dielectric (NRD) waveguide diplexer for millimeter-wave applications," in *IEEE MTT-S Int. Microwave Symp. Dig.*, Philadelphia, Pennsylvania, pp. 1471-1474, June 2003.

[42] F. Frezza, A. Galli, G. gerosa, and P. Lampariello, "Whispering-gallery modes in non-radiative-dielectric resonators," in *Proc. of Asia-Pacific Microwave Conf.*, Hsinchu, Taiwan, vol. 1, pp. 5/19-22, Oct. 1993.

[43] F. Frezza, A. Galli, G. Gerosa, and P. Lampariello, "Characterization of the resonant and coupling parameters of dielectric resonators for NRD-guide filtering devices," *IEEE MTT-S Int. Microwave Symp. Dig.*, Atlanta, USA, vol. 2, pp.893-899, June 1993.

[44] F. Frezza, A. Galli, G. Gerosa, and P. Lampariello, "Resonant frequencies and quality factors in lossy NRD cylindrical resonators," *Int. Journal of Infrared & Millimeter Waves*, vol. 16, no. 3, pp. 675-688, Mar. 1995.

[45] F. Frezza, A. Galli, and P. Lampariello, "Coupling and quality factors in parallelpiped nonradiative dielectric resonators," *Int. Journal of Infrared & Millimeter Waves,* vol. 17, no. 1, pp. 137-152, Jan. 1996.

[46] T. Yoneyama, F. Kuroki, and S. Nishida, "Design of nonradiative dielectric waveguide filters," *IEEE Trans. Microwave Theory Tech.*, vol. 32, pp. 1659-1662, Dec. 1984.

[47] J. Huang, K. Wu, T. Wang, and R. G. Bosisio, "Rigorous fields theoretical design and optimization of novel window-coupled NRD-guide bandpass filters," in *Proc. of Asia-Pacific Microwave Conf.*, Hsinchu, Taiwan, vol. 1, pp. 5/79-82, Oct. 1993.

[48] J. C. Oliver and J. A. G. Malherbe, "A bandpass filter using circular discontinuities in nonradiative dielectric waveguide," *IEEE MTT-S Int. Microwave Symp. Dig.*, Las Vegas, USA, pp. 419-422, June 1987.

[49] J. Huang and K. Wu, "A two-path multimode bandpass filters using the nonradiative dielectric (NRD) waveguide technology," *IEEE MTT-S Int. Microwave Symp. Dig.*, Orlando, USA, pp. 1547-1550, May 1995.

[50] C. Di Nallo, F. Frezza, A. Galli, G. Gerosa, M. Guglielmi, and P. Lampariello, "Experimental investigation on NRD-guide dual-mode filters," *IEEE MTT-S Int. Microwave Symp.* Dig., San Diego, USA, vol. 1, pp. 237-240, May 1994.

[51] J. C. Olivier and J. A. Malherbe, "A bandstop filter constructed in non-radiative dielectric waveguide," *IEEE MTT-S Int. Microwave Symp. Dig.*, Baltimore, USA, pp. 415-416, June 1986.

[52] J. A. Malherbe and J. C. Olivier, "A bandstop filter constructed in coupled nonradiative dielectric waveguide," *IEEE Trans. Microwave Theory Tech.*, vol. 34, pp. 1408-1412, Dec. 1986.

[53] J. A. Malherbe and J. C. Coetzee, "Bandstop filter in nonradiative dielectric waveguide using rectangular resonators," *IEEE Trans. Microwave Theory Tech.*, vol. 35, pp. 1161-1163, Dec. 1987

[54] T. Yoneyama, N. Tozawa, and S. Nishida, "Coupling characteristics of nonradiative dielectric waveguides," *IEEE Trans. Microwave Theory Tech.*, vol. 31, pp. 648-653, Aug. 1983.

[55] F. Liu, W. Wang, W. Chen, and Y. Sheng, "Coupling of NRD-guide filled with low permittivity dielectric between waveguides," *Int. Journal of Infrared and Millimeter Waves*, vol. 21, no. 8, pp. 1331-1340, Oct. 2000.

[56] D. C. Niu, T. Yoneyama, and T. Itoh, "Analysis and Measurement of NRD-guide leaky wave coupler in Ka-band," *IEEE Trans. Microwave Theory Tech.*, vol. 41, pp. 2126-2132, Dec. 1993.

[57] H. Yoshinaga and T. Yoneyama, "Design and fabrication of a nonradiative dielectric waveguide circulator," *Trans. Microwave Theory Tech.*, vol. 36, pp. 1526-1529, Nov. 1988.

[58] L. Qi and J. Hong, "Development of Ka band NRD-guide power combiner," in *Proc. of Asia-Pacific Microwave Conf.*, Hsingchu, Taiwan, vol. 1, pp. 7/46-48, Oct. 1993.

[59] T. Yoneyama, "Millimeter-wave transmitter and receiver using the nonradiative dielectric waveguide," *IEEE MTT-S Int. Microwave Symp. Dig.*, Long Beach, USA, pp. 1083-1086, June 1989.

[60] K. Wu and L. Han, "Integrated planar NRD oscillator suitable for low-cost millimeter-wave applications," *IEEE Microwave Guided Wave Lett.*, vol. 6, pp. 329-331, Sept. 1996.

[61] J. Tang, X.-Y. Zeng, S.-J. Xu, and K. Wu, "Low-loss millimeter-wave propagation characteristics of NRD-guide surface-mounted on planar substrate for hybrid integrated circuit," *IEEE MTT-S Inter. Microwave Symp. Dig.*, pp. 1679-1682, Boston, USA. June, 2000

[62] P. Yang, D. Li, and K. Wu, "Leakage and guidance properties of unbalanced insulated NRD-guide for Co-layered integrated circuits," in *IEEE MTT-s Int. Microwave Symp. Dig.*, Vol. 3, pp. 2041-2044, June 2003.

[63] L. Han and K. Wu, "An integrated transition of CPW to NRD-guide for use in millimeter-wave circuits," in *Proc. of Asia-Pacific Microwave Conf.*, India, pp. 1277-1280, Dec., 1996,

[64] K. Wu, "Hybrid integration and interconnect design platforms of planar circuits and nonradiative dielectric (NRD) guide for millimeter-wave integrated circuits and systems," *30th Europ. Microwave Conf. Proc.* Vol. 2, pp. 359-362, 2002.

[65] A. Bacha and K. Wu, "Towards an optimum design of NRD-guide and microstrip transition for hybrid integration technology," *IEEE Trans. Microwave Theory Tech.*, vol. 46, pp. 1796-1800, Nov. 1998.

[66] A. Bacha and K. Wu, "LSE-mode balun for hybrid integration of NRD-guide and microstrip line," *IEEE Microwave Guided Wave Lett.*, vol. 8, pp. 199-201, May 1998.

[67] S. Qi, K. Wu, Z. Ou, "Hybrid integrated HEMT oscillator with a multiple ring non-radiative dielectric (NRD) resonator feedback circuits," *IEEE Trans. Microwave Theory Tech.*, vol. 46, pp. 1552-1558, Oct. 1998.

[68] Y. coulibaly, D. Deslandes, J.-B. Reynald, K. Wu and F. Boone, "Transition of non-radiative waveguide to slotline for hybrid integration of uniplanar circuit and NRD-guide," Monreal, *ISMOT 2001*, pp. 359-362, June 2001.

[69] Y. Cassivi and K. Wu, "Hybrid planar NRD-guide magic-Tee junction," *IEEE Trans. Microwave Theory Tech.*, vol. 50, pp. 2405-2408, Oct. 2002.

[70] T. Itoh, *Numerical Techniques for Microwave and Millimeter-Wave Passive Structure*, John Wiley & Sons, 1989.

[71] K. Watanabe and K. Yasumoto, "Coupled-mode formulation for double-strip NRD waveguides based on singular perturbation technique," *Third Int. Kharkov Symp. Physics and Engineering of Millimeter and Submillimeter Waves*, Kharkov, Ukraine, vol. 2, pp. 589-591, Sept. 1998.

[72] K. Watanabe and K. Yasumoto, "Coupled-mode analysis of an NRD-guide coupler based on singular perturbation technique," *International Journal of Infrared and Millimeter Waves*, vol. 20, no. 12, pp. 2163-2174, Dec. 1999.

[73] A. A. Sayyah and K. Wu, "Efficient analysis of microstrip-coupled nonradiative dielectric (NRD) resonators for hybrid integrated circuits," *IEEE Trans. Microwave Theory Tech.*, vol. 47, pp. 216-223, Feb. 1999.

[74] R. Mittra, Y. L. Hou, and V. jamnejad, "Analysis of open dielectric waveguides using mode-matching techniques and variational methods," *IEEE trans. Microwave Theory Tech.* Vol. 28, pp. 36-43, Jan. 1980.

[75] S. T. Peng and A. A. Oliner, "Guidance and leakage properties of a class of open dielectric waveguides, Part I : Mathematical formulations," *IEEE trans. Microwave Theory Tech.*, vol. 29, no. 9, pp. 843-855, Sept. 1981.

[76] A. A. Oliner, S. T. Peng, T. I. Hsu and A. Aanchez, "Guidance and leakage properties of a class of open dielectric waveguides, Part II : New physical effects," *IEEE trans. Microwave Theory Tech.*, vol. 29, no. 9, pp. 855-869, Sept. 1981.

[77] F. Boone and K. Wu, "A multiple strip nonradiative dielectric guide filter design," *Symp. on Antenna Technology and Applied Electromagnetics*, Montreal, Canada, pp. 815-818, Aug. 1996.

[78] F. Boone, D. Hindson, M. Caron, J. Abdulnour and K. Wu, "Design and properties of integrated millimeter-wave bandpass filters using nonradiative dielectric waveguide for broadband wireless system," *Proc. of Spie – the Int. Society for Optical Engineering*, vol. 3861, pp. 68-77, 1999.

[79] J. Miao and P. Yang, "The characteristics of NRD waveguide gratings," *Int. Journal of Infrared and Millimeter waves*, vol. 11, no. 2, pp. 175-188, Feb. 1990.

[80] X. Y. Zeng, S. J. Xu, T. Yoneyama, K. M. Luke and K. Wu, "A systematic investigation on leaky characteristics for NRD guide with arbitrary profile of cross-section," *Int. Journal of Infrared and Millimeter Waves*, vol. 20, no. 3, pp. 491-503, 1999.

[81] S. J. Xu, X. Y. Zeng, K. Wu and K. M. Luk, "Characteristics and design consideration of leaky-wave NRD-guides for use as millimeter-wave antenna," *IEEE trans. Microwave Theory Tech.*, vol. 46, no. 12, pp. 2450-2456, Dec. 1998.

[82] K. Wu, "A combined efficient approach for analysis of nonradiative dielectric (NRD) waveguide components," *IEEE Trans. Microwave Theory Tech.*, vol. 42, pp. 672-677, April 1994.

[83] J. L. Volaks, A. Chatterjee, and L. C. Kempel, *Finite Element Method for Electromagnetics*, IEEE Press, New York, USA, 1998.

[84] A. Taflove and S. C. Hagness, *Computational Electrodynamics: the Finite-Difference Time-Domain Method*, Artech House, Norwood, MA, USA, 2 edi., 2000.

[85] C. Christopoulos, *Transmission-Line Modeling Method: TLM*, IEEE Press, New York, USA, 1995.

[86] B. Ghosh, N. R. S. Simons, L. Shafai, A. Ittipiboon and A. Petosa, "TLM-based modal-extraction approach for the investigation of discontinuities in the rectangular waveguide and the NRD," *IEEE trans. Microwave Theory Tech.*, vol. 50, no. 10, pp. 2294-2304, Oct. 2002.

[87] A. F. Peterson, S. C. Ray, and R. Mittra, *Computational Methods for Electromagnetics*, IEEE Press, New York, USA, 1998.

[88] R. F. Harrington, *Field Computation by Moment Methods, Macmillan*, New York, 1968.

[89] J. S. Bagby, D. P. Nyquist, and B. C. Drachman, "Integral formulation for analysis of integrated dielectric waveguides," *IEEE trans. Microwave Theory Tech.* Vol. 33, pp. 906-915, Oct. 1985.

[90] E. W. Kolk, N. H. G. Baken, and H. Blok, "Domain integral equation analysis of integrated optical channel and ridge waveguides in stratified media," *IEEE trans. Microwave Theory Tech.* Vol. 38, pp. 78-85, Jan. 1990.

[91] J. F. Kiang, S. M. Ali, and J. A. Kong, "Integral equation solution to the guidance and leakage properties of coupled dielectric strip waveguides," *IEEE trans. Microwave Theory Tech.* Vol. 38, pp. 193-203, Feb. 1990.

[92] H. Y. Yang, J. A. Castaneda, and N. G. Alexopoulos, "An integral equation analysis of an infinite array of rectangular dielectric waveguides," *IEEE trans. Microwave Theory Tech.* Vol. 38, pp. 873-880, July 1990.

[93] G. Athnanasoulias and N. K. Uzunoglu, "An accurate and efficient entire-domain basis Galerkin's method for the integral equation analysis of integrated rectangular dielectric waveguides," *IEEE trans. Microwave Theory Tech.* Vol. 43, pp. 2794-2804, Dec. 1995.

[94] S. J. Polychronopoulos and N. K. Uzunoglu, "propagation and coupling properties of integral optical waveguides-an integral equation formulation," *IEEE trans. Microwave Theory Tech.* Vol. 44, pp. 641-650, May 1996.

[95] S. L. Lin and G. W. Hanson "An efficient full-wave method for analysis of dielectric resonators possessing separable geometries immersed in inhomogeneous environments," *IEEE Trans. Microwave Theory Tech.*, vol. 48, pp. 84-92, Jan. 2000.

[96] S. Y. Ke and Y. T. Cheng, "Integration equation analysis on resonant frequencies and quality factors of rectangular dielectric resonators," *IEEE Trans. Microwave Theory Tech.*, vol. 49, pp. 571-574, Mar. 2001.

[97] T. Vaupel and V. Hansen, "Electrodynamic analysis of combined microstrip and coplanar/slotline structures with 3-D components based on a surface/volume

integral-equation approach," *IEEE Trans. Microwave Theory Tech.*, vol. 47, pp. 1788-1800, Sep. 1999.

[98] D. Li, Y. Cassivi, P. Yang, and K. Wu, "Analysis and design of bridged NRD-guide coupler for millimeter-wave applications," *IEEE trans. Microwave Theory Tech.* vol. 53, pp. 2546-2551, Aug. 2005.

[99] D. Li, P. Yang, and K. Wu, "An order-reduced volume-integral equation approach for analysis of NRD-guide and H-guide millimeter-wave circuits," *IEEE trans. Microwave Theory Tech.*, vol. 53, pp. 799-812, Mar. 2005.

[100] D. Li and K. Wu, "A generalized surface-volume integral-equation (SVIE) approach for analysis of hybrid planar/NRD-guide integrated circuits," *IEEE trans. Microwave Theory Tech.* vol. 53, pp. 2732-2742, Sep. 2005.

[101] R. F. Harrington, *Time-Harmonic Electromagnetic field.* New York: McGraw-Hill, 1961.

[102] R. F. Harrington, "Boundary integral formulations for homogeneous material bodies," *J. Electromagn. Waves Applicat.*, vol. 3, no. 1, pp. 1-15, 1989.

[103] A. A. Sebak and L. Shafai, "Performance of various integral equation formulations for numerical solution of scattering by impedance objects," *Can. J. phys.* Vol. 62, pp. 605-615, 1984.

[104] A. W. Glisson, "Electromagnetic scattering by arbitrarily shaped surfaces with impedance boundary conditions," *Radio Sci.*, vol. 27, pp. 935-943, Nov./Dec. 1992.

[105] I. P. Theron and J. H. Cloete, "On the surface impedance used to model the conductor losses of microstrip structures," *Inst. Elect. Eng. Proc. Microwave antennas Propagat.*, vol. 142, pp. 35-40, Feb. 1995.

[106] C. M. Butler, Y. Rahmat-samii, and R. Mittra, "Electromagnetic penetration through apertures in conducting surfaces," *IEEE Trans. Antennas Propagat.*, vol. 26, pp. 82-93, Jan. 1978.

[107] B. L. Moiseiwitsch, *Integral Equations*, Longman, London, UK, 1977.

[108] R. F. Harrington, "The method of moments in electromagnetics," *J. Electromagn. Waves Applicat.*, vol. 1, no. 3, pp. 181-200, 1987.

[109] J. Strain, "Locally-corrected multidimensional quadrature rules for singular functions," *SIAM J. Sci. Comput.*, vol. 16, no. 4, pp. 992-1017, 1995.

[110] W. C. Chew, *Waves and Fields in Inhomogeneous Media*, Van Nostrand Reinhold, New York, 1990.

[111] K. A. Michalski and J. R. Mosig, "Multilayed media Green's functions in integral equation formulations," *IEEE Trans. Antennas Propaga.*, vol. 45, pp. 508-519, Mar. 1997.

[112] D. G. Dudley, "Error minimization and convergence in numerical methods," *Electromagnetics*, vol. 15, no. 1, pp. 89-97, Jan.-Feb. 1985.

[113] T. K. Sarkar, "A note on the choice of weighting functions in the method of moments," *IEEE Trans. Antennas Propagat.*, vol. 33, pp.436-441, April 1985.

[114] S. Wandzura, "Optimality of Garlerkin method for scattering computations," *Microwave and Optical Technology Letters*, vol. 4, pp. 199-200, April 1991.

[115] S. M. Rao, D. R. Wilton, and A. W. Glisson, "Electromagnetic scattering by surfaces of arbitrary shape," *IEEE Trans. Antennas Propagat.* Vol. 33, pp. 409-418, May 1982.

[116] A. W. Glisson and D. R. Wilton, "Simple and efficient methods for problems of electromagnetic radiation and scattering from surfaces," *IEEE Trans. Antennas Propagat.* Vol. 28, pp. 593-603, Sep. 1980.

[117] E. Jorgensen, Higher-Order integral equation methods in computational electromagnetics, Ph. D. Thesis, The Technical University of Denmark, 2003.

[118] F. J. Tischer, "A waveguide structure with low losses," *Arch. Elec. Ubertragung*, vol. 7, pp. 592-596, Dec. 1953.

[119] D. Kim, D. Kawabe, K. Araki, and Y. Naito, "Directly connected image guide 3-dB couplers with very flat coupling," *IEEE trans. Microwave Theory Tech.* Vol. 32, pp. 621-627, June 1984.

[120] D. M. Pozar, "Impedance and mutual coupling of rectangular microstrip antennas," *IEEE Trans. Antennas Propaga.*, vol. 30, pp. 1191-1196, Nov. 1982.

[121] C. D. Nallo, F. Frezza, and A. galli, "Full-wave modal analysis of arbitrary-shaped dielectric waveguides through an efficient boundary-element-method formulation," *IEEE Trans. Microwave Theory Tech.*, vol. 43, pp. 2982-2990, Dec. 1995.

[122] J. Sercu, N. Faché, F. Libbrecht and P. Lagusse, "Mixed potential integral equation technique for hybrid microstrip-slotline multilayered circuits using a mixed rectangular-triangular mesh," *IEEE Trans. Microwave Theory Tech.*, vol. 43, pp. 1162-1172, May, 1995.

[123] R. W. Jackson and D. Pozar, "Full-wave analysis of microstrip open-end and gap discontinuities," *IEEE Trans. Microwave Theory Tech.*, vol. 33, pp. 1036-1042, Oct. 1985.

[124] P. L. Sullivan and D. H. Schaubert, "Analysis of an aperture coupled microstrip antenna," *IEEE Trans. Antennas Propaga.*, vol. 34, pp. 977-984, Aug. 1986.

[125] L. T. Hildebrand and J. Joubert, "Full-wave analysis of a new microstrip-to-waveguide interconnect configuration," *IEEE Trans. Microwave Theory Tech.*, vol. 48, pp. 1-7, Jan. 2000.

[126] D. G. Kurup and A. Rydberg, "Dielectric connectors for multilayered RF integration," *Microwave Optical Technology Lett.*, Vol. 23, pp. 230-233, Nov. 1999.

Appendix A

Derivation of Dyadic Green's Functions in Multilayered Media

A large number of authors have worked on the derivation of DGF's for layered media, both isotropic and anisotropic. The derivation presented below is only for isotropic media and mainly comes from [111]. The geometry for the derivation of planar stratified-medium Green's function is shown in Fig. 2.2, including the definition of all relevant parameters. It is well known that a closed form solution to this problem only exists in the spectral domain. Therefore, we first transform the problem given in spatial coordinates into the spectral domain. Due to this spatial Fourier transform, the original problem is in fact reduced to that of solving an equivalent transmission-line network along the z coordinate.

A.1 Transformation to the Spectral Domain

Fields (***E***, ***H***) are to be calculated at an arbitrary point r due to a specified current distribution (***J***, ***M***), as illustrated in Fig. 2.2. These fields are governed by Maxwell's equations.

$$\nabla\times\mathbf{E} = -j\omega\mu_0\mathbf{H} - \mathbf{M} \tag{A.1}$$

$$\nabla\times\mathbf{H} = j\omega\varepsilon\mathbf{E} + \mathbf{J} \tag{A.2}$$

Since the medium is homogeneous and of infinite extent in any transverse (to z) plane, the analysis is facilitated by the Fourier transformation of all fields with respect to the transverse coordinates. Hence, we express any scalar field component as $f(\mathbf{r}) \equiv f(\boldsymbol{\rho}, z)$, where $\boldsymbol{\rho} = \hat{\mathbf{x}}x + \hat{\mathbf{y}}y$ is the projection of $\mathbf{r}$ on the (x, y) plane, and introduce the Fourier transform pair

$$\Im f(\mathbf{r}) \equiv \tilde{f}(\mathbf{k}_\rho; z) = \int_{-\infty}^{+\infty}\int_{-\infty}^{+\infty} f(\mathbf{r}) e^{j\mathbf{k}_\rho\cdot\boldsymbol{\rho}} dxdy \tag{A.3}$$

$$\Im^{-1}\tilde{f}\left(\mathbf{k}_\rho,z\right)\equiv f\left(\mathbf{r}\right)=\frac{1}{\left(2\pi\right)^2}\int_{-\infty}^{+\infty}\int_{-\infty}^{+\infty}\tilde{f}\left(\mathbf{k}_\rho,z\right)e^{-j\mathbf{k}_\rho\cdot\boldsymbol{\rho}}dk_x dk_y \tag{A.4}$$

where $\mathbf{k}_\rho=\hat{\mathbf{x}}k_x+\hat{\mathbf{y}}k_y$. Upon applying (A.3) to (A.1) and (A.2), and separating the transverse and longitudinal parts of the resulting equations, one obtains

$$\frac{d}{dz}\tilde{\mathbf{E}}_t=\frac{1}{j\omega\varepsilon}\left(k^2-\mathbf{k}_\rho\mathbf{k}_\rho\cdot\right)\left(\tilde{\mathbf{H}}_t\times\tilde{\mathbf{z}}\right)+\mathbf{k}_\rho\frac{\tilde{J}_z}{\omega\varepsilon}-\tilde{\mathbf{M}}_t\times\tilde{\mathbf{z}} \tag{A.5}$$

$$\frac{d}{dz}\tilde{\mathbf{H}}_t=\frac{1}{j\omega\mu_0}\left(k^2-\mathbf{k}_\rho\mathbf{k}_\rho\cdot\right)\left(\tilde{\mathbf{z}}\times\tilde{\mathbf{E}}_t\right)+\mathbf{k}_\rho\frac{\tilde{M}_z}{\omega\mu_0}-\tilde{\mathbf{z}}\times\tilde{\mathbf{J}}_t \tag{A.6}$$

$$-j\omega\varepsilon\tilde{E}_z=j\mathbf{k}_\rho\cdot\left(\tilde{\mathbf{H}}_t\times\tilde{\mathbf{z}}\right)+\tilde{J}_z \tag{A.7}$$

$$-j\omega\mu_0\tilde{H}_z=j\mathbf{k}_\rho\cdot\left(\tilde{\mathbf{z}}\times\tilde{\mathbf{E}}_t\right)+\tilde{M}_z \tag{A.8}$$

where $k=\omega\sqrt{\mu_0\varepsilon}$. The subsequent analysis is greatly simplified if one defines a rotated spectrum-domain coordinate system based on $\left(\mathbf{k}_\rho,\hat{\mathbf{z}}\times\mathbf{k}_\rho\right)$, with the unit vectors $\left(\hat{\mathbf{u}},\hat{\mathbf{v}}\right)$ given by

$$\hat{\mathbf{u}}=\frac{\mathbf{k}_\rho}{k_\rho}=\frac{k_x}{k_\rho}\hat{\mathbf{x}}+\frac{k_y}{k_\rho}\hat{\mathbf{y}},\qquad \hat{\mathbf{v}}=\hat{\mathbf{z}}\times\frac{\mathbf{k}_\rho}{k_\rho}=-\frac{k_y}{k_\rho}\hat{\mathbf{x}}+\frac{k_x}{k_\rho}\hat{\mathbf{y}} \tag{A.9}$$

where $k_\rho=\sqrt{k_x^2+k_y^2}$. If we now express the transverse electric and magnetic fields as

$$\tilde{\mathbf{E}}_t=\hat{\mathbf{u}}V^e+\hat{\mathbf{v}}V^h,\qquad \tilde{\mathbf{H}}_t\times\hat{\mathbf{z}}=\hat{\mathbf{u}}I^e+\hat{\mathbf{v}}I^h \tag{A.10}$$

and project (A.5) and (A.6) on $\hat{\mathbf{u}}$ and $\hat{\mathbf{v}}$, we find that these equations decouple into two sets of transmission line equations of the form

$$\frac{dV^p}{dz}=-jk_z^pZ^pI^p+v^p,\qquad \frac{dI^p}{dz}=-jk_z^pY^pV^p+i^p \tag{A.11}$$

where the superscript p assumes the values of e or h. Hence, the components of $\tilde{\mathbf{E}}_t$ and $\tilde{\mathbf{H}}_t$ in the (u, v) plane may be interpreted as voltages and currents on a transmission-line analog of the medium along the z axis, which was anticipated in the notation introduced in (A.9). The propagation wave numbers and the characteristic impedances and admittances of this transmission line are given as

$$k_z^p = \sqrt{k^2 - k_\rho^2} \tag{A.12}$$

$$Z^e = \frac{1}{Y^e} = \frac{k_z^e}{\omega\varepsilon}, \qquad Z^h = \frac{1}{Y^h} = \frac{\omega\mu_0}{k_z^h} \tag{A.13}$$

where the square root branch in (A.12) is specified by the condition that $-\pi < \arg\{k_z^p\} \leq 0$. The voltage and current sources in (A.11) are given by

$$v^e = \frac{k_\rho}{\omega\varepsilon}\tilde{J}_z - \tilde{M}_v, \qquad i^e = -\tilde{J}_u \tag{A.14}$$

$$i^h = -\frac{k_\rho}{\omega\mu_0}\tilde{M}_z - \tilde{J}_v, \quad v^h = \tilde{M}_u \tag{A.15}$$

In view of (A.9) and (A.6), (A.7), the spectral fields may now be expressed as

$$\tilde{\mathbf{E}} = \hat{\mathbf{u}}V^e + \hat{\mathbf{v}}V^h - \hat{\mathbf{z}}\frac{1}{j\omega\varepsilon}\left(jk_\rho I^e + \tilde{J}_z\right) \tag{A.16}$$

$$\tilde{\mathbf{H}} = -\hat{\mathbf{u}}I^h + \hat{\mathbf{v}}I^e + \hat{\mathbf{z}}\frac{1}{j\omega\mu_0}\left(jk_\rho V^h - \tilde{M}_z\right) \tag{A.17}$$

which indicate that outside the source region (V^e, I^e) and (V^h, I^h) represent fields that are, respectively, TM and TE to z. The original vector problem has thus been reduced to the scalar transmission line problem. The space-domain fields ($\boldsymbol{E}$, $\boldsymbol{H}$) are obtained from (A.16) and (A.17) via the inverse transform (A.4).

A.2 Dyadic Green's Functions

Consider the solutions of the transmission line equations (A.11) for unit-strength impulse sources. Hence, let $V_i^p(z \mid z')$ and $I_i^p(z \mid z')$ denote the voltage and current, respectively, at z due to a 1-A shunt current source at z', and let $V_v^p(z \mid z')$ and $I_v^p(z \mid z')$ denote the voltage and current, respectively, at z due to a 1-V series voltage source at z' (see Fig. A.1). Then, it follows from (A.11) that these transmission line Green's functions (TLGFs) satisfy the following:

$$\frac{dV_i^p}{dz} = -jk_z^p Z^p I_i^p, \quad \frac{dI_i^p}{dz} = -jk_z^p Y^p V_i^p + \delta(z-z') \tag{A.18}$$

$$\frac{dV_v^p}{dz} = -jk_z^p Z^p I_v^p + \delta(z-z'), \quad \frac{dI_p^p}{dz} = -jk_z^p Y^p V_v^p \tag{A.19}$$

where δ is the Dirac delta, and that they possess the reciprocity properties

$$\begin{aligned} V_i^p(z \mid z') &= V_i^p(z' \mid z), & I_v^p(z \mid z') &= I_v^p(z' \mid z) \\ V_v^p(z \mid z') &= -I_i^p(z' \mid z), & I_v^p(z \mid z') &= -V_v^p(z' \mid z) \end{aligned} \tag{A.20}$$

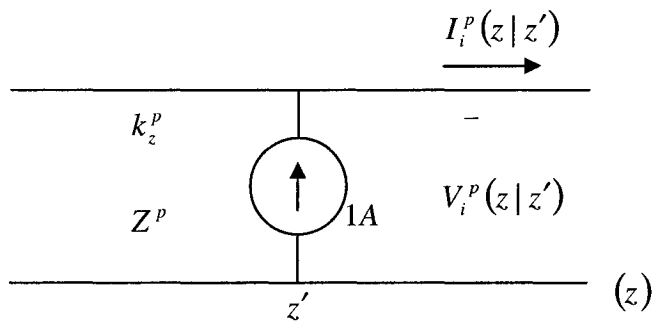

(a)

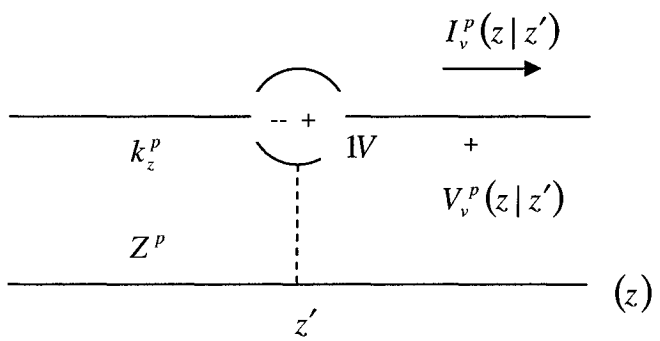

(b)

Fig. A.1. Network problems for the determination of the transmission-line Green's functions.

The linearity of the transmission line equations (A.11) allows one to obtain (V^p, I^p) at any point z via the superposition integrals

$$V^p = \left\langle V_i^p, i^p \right\rangle + \left\langle V_v^p, v^p \right\rangle, \qquad I^p = \left\langle I_i^p, i^p \right\rangle + \left\langle I_v^p, v^p \right\rangle \tag{A.21}$$

Upon substituting these equations into (A.16) and (A.17) and using (A.15), one obtains spectrum-domain counterparts of (2.3) and (2.4),

$$\tilde{\mathbf{E}} = \left\langle \tilde{\bar{\mathbf{G}}}^{EJ}; \tilde{\mathbf{J}} \right\rangle + \left\langle \tilde{\bar{\mathbf{G}}}^{EM}; \tilde{\mathbf{M}} \right\rangle \tag{A.22}$$

$$\tilde{\mathbf{H}} = \left\langle \tilde{\bar{\mathbf{G}}}^{HJ}; \tilde{\mathbf{J}} \right\rangle + \left\langle \tilde{\bar{\mathbf{G}}}^{HM}; \tilde{\mathbf{M}} \right\rangle \tag{A.23}$$

where the spectral DGFs $\tilde{\bar{\mathbf{G}}}^{PQ}\left(\mathbf{k}_\rho; z \mid z'\right)$ are given as

$$\tilde{\bar{\mathbf{G}}}^{EJ} = -\hat{\mathbf{u}}\hat{\mathbf{u}} V_i^e - \hat{\mathbf{v}}\hat{\mathbf{v}} V_i^h + \hat{\mathbf{z}}\hat{\mathbf{u}} \frac{k_\rho}{\omega\varepsilon} I_i^e + \hat{\mathbf{u}}\hat{\mathbf{z}} \frac{k_\rho}{\omega\varepsilon} V_v^e + \hat{\mathbf{z}}\hat{\mathbf{z}} \frac{1}{j\omega\varepsilon}\left[\frac{k_\rho^2}{j\omega\varepsilon} I_v^e - \delta\left(z - z'\right)\right] \tag{A.24}$$

$$\tilde{\bar{\mathbf{G}}}^{HJ} = \hat{\mathbf{u}}\hat{\mathbf{v}} I_i^h - \hat{\mathbf{v}}\hat{\mathbf{u}} I_i^e - \hat{\mathbf{z}}\hat{\mathbf{v}} \frac{k_\rho}{\omega\mu_0} V_i^h + \hat{\mathbf{v}}\hat{\mathbf{z}} \frac{k_\rho}{\omega\varepsilon} I_v^e \tag{A.25}$$

$$\tilde{\bar{\mathbf{G}}}^{EM} = -\hat{\mathbf{u}}\hat{\mathbf{v}} V_v^e + \hat{\mathbf{v}}\hat{\mathbf{u}} V_v^h + \hat{\mathbf{z}}\hat{\mathbf{v}} \frac{k_\rho}{\omega\varepsilon} I_v^e - \hat{\mathbf{v}}\hat{\mathbf{z}} \frac{k_\rho}{\omega\mu_0} V_i^h \tag{A.26}$$

$$\tilde{\bar{\mathbf{G}}}^{HM} = -\hat{\mathbf{u}}\hat{\mathbf{u}} I_v^h - \hat{\mathbf{v}}\hat{\mathbf{v}} I_v^e + \hat{\mathbf{z}}\hat{\mathbf{u}} \frac{k_\rho}{\omega\mu_0} V_v^h + \hat{\mathbf{u}}\hat{\mathbf{z}} \frac{k_\rho}{\omega\mu_0} I_i^h + \hat{\mathbf{z}}\hat{\mathbf{z}} \frac{1}{j\omega\mu_0}\left[\frac{k_\rho^2}{j\omega\mu_0} V_i^h - \delta\left(z - z'\right)\right] \tag{A.27}$$

A.3 Solution of Equivalent Transmission-Line Problem

The formulation developed so far is for an unspecified stratification, since no assumption has been made regarding the z dependence of the media parameters. We now specify it to the case of a multilayered media with piecewise-constant parameters. The parameters pertaining to layer n with boundaries at z_n and z_{n+1} are distinguished by a subscript n. The transmission line analog of the layered medium consists of a cascade connection of uniform transmission line sections, where section n with terminals at z_n and z_{n+1} has propagation constant and characteristic impedance. To find the TLGFs we

excite the transmission line network by unit-strength voltage and current sources at z' in section n and compute the voltage and current at z in section m. Hence, the primed media parameters assume the values pertaining to layer n, while the unprimed ones are those of layer m. The source section is illustrated in Fig. A.2, where $\bar{\Gamma}_n^p$ and $\bar{\Gamma}_n^p$ are the voltage reflection coefficients looking to the left and right, respectively, out of the terminals of sections n. These coefficients, which are referred to z_n and z_{n+1}, respectively, may be computed from the relations

$$\bar{\Gamma}_{n+1}^p = \frac{\Gamma_{n,n+1}^p + \bar{\Gamma}_n^p t_n^p}{1 + \Gamma_{n,n+1}^p \bar{\Gamma}_n^p t_n^p} \tag{A.28}$$

$$\bar{\Gamma}_{n-1}^p = \frac{\Gamma_{n,n-1}^p + \bar{\Gamma}_n^p t_n^p}{1 + \Gamma_{n,n-1}^p \bar{\Gamma}_n^p t_n^p} \tag{A.29}$$

where

$$\Gamma_{ij}^p = \frac{Z_i^p - Z_j^p}{Z_i^p + Z_j^p} \tag{A.30}$$

and $t_n^p = e^{-j2k_{zn}^p d_n}$ with $d_n = z_{n+1} - z_z$. These formulas follow from the source-free transmission line (A.9) and the continuity of the voltage and currents at the line junctions. One applies (A.28) and (A.29) recursively beginning at, respectively, the left and the right ends of the transmission line network.

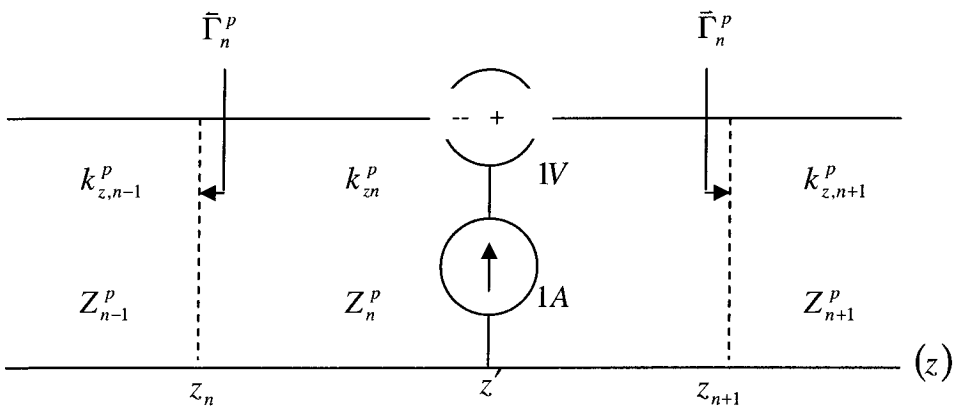

Fig. A.2. Voltage and current point sources in a transmission-line section.

Consider first the case m=n, when z is within the source section. The TLGF V_i^p is then readily determined from (A.18) as

$$V_i^p(z\,|\,z') = \frac{Z_n^p}{2}\left[e^{-jk_{zn}^p|z-z'|} + \frac{1}{D_n^p}\sum_{s=1}^{4} R_{ns}^p e^{-jk_{zn}^p \gamma_{ns}}\right] \tag{A.31}$$

where

$$D_n^p = 1 - \bar{\Gamma}_n^p \bar{\Gamma}_n^p t_n^p \tag{A.32}$$

$$R_{n1}^p = \bar{\Gamma}_n^p, \qquad R_{n2}^p = \bar{\Gamma}_n^p, \qquad R_{n3}^p = R_{n4}^p = \bar{\Gamma}_n^p \bar{\Gamma}_n^p \tag{A.33}$$

$$\gamma_{n1} = 2z_{n+1} - (z+z'), \qquad \gamma_{n2} = (z+z') - 2z_n$$

$$\gamma_{n3} = 2d_n + (z-z'), \qquad \gamma_{n4} = 2d_n - (z-z') \tag{A.34}$$

The first term in (A.31) represents the direct ray between the source and the field point, while the second term represents the rays that undergo partial reflections at the upper and lower slab boundaries before reaching the observation point. The remaining TLGF's may already be derived from (A.31) upon using (A.18)-(A.20). For example, one may obtain I_i^p from V_i^p via the first equation of (A.18), from which follows via from the third equation of (A.20). The result is

$$V_v^p(z\,|\,z') = \frac{1}{2}\left[\pm e^{-jk_{zn}^p|z-z'|} - \frac{1}{D_n^p}\sum_{s=1}^{4}(-1)^s R_{ns}^p e^{-jk_{zn}^p \gamma_{ns}}\right] \tag{A.35}$$

Where the upper and lower signs pertain to $z > z'$ and $z < z'$, respectively. To conserve space, we do not list the expressions for I_v^p and I_i^p which, as is evident from (A.18) and (A.19), are dual to those for V_i^p and V_v^p, respectively, and may be obtained from the latter by replacing the impedances by admittances (which has also the effect of changing the signs of reflection coefficients).

Consider next the case $m < n$, where z is outside the source section and $z < z'$. Given the voltage $V^p(z_n)$ across the left terminals of section n, the voltage $V^p(z)$ and current $I^p(z)$ at any point z in section m can be found from the homogeneous form of the transmission-line equations (A.9) as.

$$\begin{Bmatrix} V^p(z) \\ I^p(z) \end{Bmatrix} = V^p(z_n) \frac{\prod_{k=m+1}^{n-1} \tilde{T}_k^p}{1+\tilde{\Gamma}_m^p t_m^p} \times \begin{Bmatrix} \tilde{\tau}_m^p(z) \\ \tilde{y}_m^p(z) \end{Bmatrix} e^{-jk_{zm}^p(z_{m+1}-z)} \tag{A.36}$$

where

$$\tilde{T}_k^p \equiv \frac{V^p(z_k)}{V^p(z_{k+1})} = \frac{(1+\tilde{\Gamma}_k^p)\theta_k^p}{1+\tilde{\Gamma}_k^p t_k^p} \tag{A.37}$$

with $\theta_k^p = e^{-jk_{kz}^p d_k}$, and where

$$\tilde{\tau}_m^p(z) = 1+\tilde{\Gamma}_m^p e^{-j2k_{zm}^p(z-z_m)} \tag{A.39}$$

$$\tilde{y}_m^p(z) = -Y_m^p\left[1-\tilde{\Gamma}_m^p e^{-j2k_{zm}^p(z-z_m)}\right] \tag{A.39}$$

Analogous formulas may be developed for the case $m>n$, when z is outside the source section and $z>z'$. However, this is hardly necessary because the reciprocity theorems (A.21) allow one to interchange the source and field point locations. For example, $V_v^p(z\,|\,z')$ may be computed as $-I_i^p(z'\,|\,z)$. This application of reciprocity also results in a shorter and more efficient computer code.

Appendix B

The Integrands Used in the Integrals in NRD-Guide Open-Ends

The Fourier transforms of $\mathbf{f}_j(x,y)$ and $\mathbf{f}_p(x,y)$ are

$$\tilde{P}_q(k_x)=\frac{\sin(k_x D_x/2)}{k_x}e^{-jk_x x_q} \qquad \tilde{W}_r(k_y)=\frac{\sin(k_y D_y/2)}{k_y}e^{-jk_y y_r} \tag{B.1}$$

$$\tilde{f}_j(k_x,k_y)=\frac{\sin(k_x D_x/2)}{k_x}\cdot\frac{\sin(k_y D_y/2)}{k_y}e^{-jk_x x_q - jk_y y_r} \tag{B.2}$$

$$f_p(k_x)=\frac{j}{k_x \mp \beta}\left(1-e^{j(k_x \mp \beta)\Delta x}\right) \tag{B.3}$$

$$g_p^s(k_y)=\frac{2j}{k_y^2-\beta_y^2}\cdot\left(k_y \sin\langle\beta_y b/2\rangle\cos\langle k_y b/2\rangle-\beta_y\cos\langle\beta_y b/2\rangle\sin\langle k_y b/2\rangle\right) \tag{B.4}$$

$$g_p^c(k_y)=\frac{2}{k_y^2-\beta_y^2}\cdot\left(k_y \cos\langle\beta_y b/2\rangle\sin\langle k_y b/2\rangle-\beta_y\sin\langle\beta_y b/2\rangle\cos\langle k_y b/2\rangle\right) \tag{B.5}$$

The integrands Int_{ij}^{uv} and $Int_{i,p}^{uv}$ are

$$Int_{i,j(p)}^{xx} = f^* f_{s,q(p)}(k_x)_{even}\cdot g^* g_{t,r(p)}^s(k_y)_{even} \tag{B.6a}$$

$$Int_{i,j(p)}^{xy} = f^* f_{s,q(p)}(k_x)_{odd}\cdot g^* g_{t,r(p)}^c(k_y)_{odd} \tag{B.6b}$$

$$Int_{i,j(p)}^{xz} = f^* f_{s,q(p)}(k_x)_{odd}\cdot g^* g_{t,r(p)}^s(k_y)_{even} \tag{B.6c}$$

$$Int_{i,j(p)}^{yx} = f^* f_{s,q(p)}(k_x)_{even}\cdot g^* g_{t,r(p)}^s(k_y)_{even} \tag{B.6d}$$

$$Int_{i,j(p)}^{yy} = f^* f_{s,q(p)}(k_x)_{even}\cdot g^* g_{t,r(p)}^c(k_y)_{even} \tag{B.6e}$$

$$Int_{i,j(p)}^{yz} = f^* f_{s,q(p)}(k_x)_{even}\cdot g^* g_{t,r(p)}^c(k_y)_{odd} \tag{B.6f}$$

$$Int_{i,j(p)}^{zx} = f^* f_{s,q(p)}(k_x)_{odd}\cdot g^* g_{t,r(p)}^s(k_y)_{even} \tag{B.6g}$$

$$Int_{i,j(p)}^{zy} = f^* f_{s,q(p)}(k_x)_{even}\cdot g^* g_{t,r(p)}^c(k_y)_{odd} \tag{B.6h}$$

$$Int^{zz}_{i,j(p)} = f^{*} f_{s,q(p)}\left(k_x\right)_{even} \cdot g^{*} g^{s}_{t,r(p)}\left(k_y\right)_{even} \tag{B.6i}$$

where

$$f^{*} \cdot f_{s,p}\left(k_x\right)_{even} = \frac{\text{-2sin}\left\langle \mathrm{k_x} D_x / 2 \right\rangle}{k_x} \cdot \left\{ \frac{\pm j\beta\left[\cos\left(k_x\left(x_s - D_x/2\right)\right) - \cos\left(k_x\left(x_s - D_x/2 - \Delta x\right)\right)\right]}{k_x^2 - \beta^2} - \frac{k_x\left[\sin\left(k_x\left(x_s - D_x/2\right)\right) - \sin\left(k_x\left(x_s - D_x/2 - \Delta x\right)\right)\right]}{k_x^2 - \beta^2} \right\} \tag{B.7}$$

$$f^{*} \cdot f_{s,p}\left(k_x\right)_{odd} = \frac{\text{-2sin}\left\langle \mathrm{k_x} D_x / 2 \right\rangle}{k_x} \cdot \left\{ \frac{jk_x\left[\cos\left(k_x\left(x_s - D_x/2\right)\right) - \cos\left(k_x\left(x_s - D_x/2 - \Delta x\right)\right)\right]}{k_x^2 - \beta^2} + \frac{\mp\beta\left[\sin\left(k_x\left(x_s - D_x/2\right)\right) - \sin\left(k_x\left(x_s - D_x/2 - \Delta x\right)\right)\right]}{k_x^2 - \beta^2} \right\} \tag{B.8}$$

$$f^{*} \cdot f_{sq}\left(k_x\right)_{even} = \left(\frac{2\sin\left\langle \mathrm{k_x} D_x / 2 \right\rangle}{k_x} \right)^2 \cos\left(k_x\left(x_s - x_q\right)\right) \tag{B.9}$$

$$f^{*} \cdot f_{sq}\left(k_x\right)_{odd} = j\left(\frac{2\sin\left\langle \mathrm{k_x} D_x / 2 \right\rangle}{k_x} \right)^2 \sin\left(k_x\left(x_s - x_q\right)\right) \tag{B.10}$$

$$g^{*} g^{s}_{t,p}\left(k_y\right)_{even} = \frac{2\sin\left(k_y D_y / 2\right)}{k_y} \cdot \frac{-2}{k_y^2 - \beta_y^2} \cdot \sin\left(k_y\left(y_t + D_y/2\right)\right) \cdot \left(k_y \sin\left\langle \beta_y b/2 \right\rangle \cos\left\langle k_y b/2 \right\rangle - \beta_y \cos\left\langle \beta_y b/2 \right\rangle \sin\left\langle k_y b/2 \right\rangle\right) \tag{B.11}$$

$$g^{*} g^{s}_{t,p}\left(k_y\right)_{odd} = \frac{2\sin\left(k_y D_y / 2\right)}{k_y} \cdot \frac{2j}{k_y^2 - \beta_y^2} \cdot \cos\left(k_y\left(y_t + D_y/2\right)\right) \cdot \left(k_y \sin\left\langle \beta_y b/2 \right\rangle \cos\left\langle k_y b/2 \right\rangle - \beta_y \cos\left\langle \beta_y b/2 \right\rangle \sin\left\langle k_y b/2 \right\rangle\right) \tag{B.12}$$

$$g^{*} g^{c}_{t,p}\left(k_y\right)_{even} = \frac{2\sin\left(k_y D_y / 2\right)}{k_y} \cdot \frac{2}{k_y^2 - \beta_y^2} \cdot \cos\left(k_y\left(y_t + D_y/2\right)\right) \cdot \left(k_y \cos\left\langle \beta_y b/2 \right\rangle \sin\left\langle k_y b/2 \right\rangle - \beta_y \sin\left\langle \beta_y b/2 \right\rangle \cos\left\langle k_y b/2 \right\rangle\right) \tag{B.13}$$

$$g^* g^c_{t,p}(k_y)_{odd} = \frac{2\sin(k_y D_y/2)}{k_y} \cdot \frac{2j}{k_y^2 - \beta_y^2} \cdot \sin\left(k_y\left(y_t + D_y/2\right)\right) \cdot \left(k_y \cos\langle\beta_y b/2\rangle \sin\langle k_y b/2\rangle - \beta_y \sin\langle\beta_y b/2\rangle \cos\langle k_y b/2\rangle\right) \tag{B.14}$$

$$g^* g_{tr}(k_y)_{even} = \left(\frac{2\sin(k_y D_y/2)}{k_y}\right)^2 \cdot \cos\left(k_y\left(y_t - y_r\right)\right) \tag{B.15}$$

$$g^* g_{tr}(k_y)_{odd} = j\left(\frac{2\sin(k_y D_y/2)}{k_y}\right)^2 \cdot \sin\left(k_y\left(y_t - y_r\right)\right) \tag{B.16}$$

$w^{uv}_{i,p}$ have the following expressions,

$$w^{xx}_{i,p} = w^{zz}_{i,p} = \frac{-2\sin(\beta\Delta x/2)\cdot e^{\pm j\beta\left(x_{i_s} - D_x/2\right)}}{\beta} \cdot \frac{\cos(\beta_y y_t) - \cos\left(\beta_y (y_t + D_y)\right)}{\beta_y} \tag{B.17}$$

$$w^{yy}_{i,p} = \frac{-2\sin(\beta\Delta x/2)\cdot e^{\pm j\beta\left(x_{i_s} - D_x/2\right)}}{\beta} \cdot \frac{\sin\left(\beta_y (y_t + D_y)\right) - \sin(\beta_y y_t)}{\beta_y} \tag{B.18}$$

The asymptotic equations of $f^* f_{s,p}(k_x)_{even}$ and $f^* f_{s,q}(k_x)_{even}$ are

$$f^* f_{s,p}(k_x)^A_{even} = 2\sin\langle k_x D_x/2\rangle \cdot \frac{\sin\left(k_x\left(x_s - D_x/2\right)\right) - \sin\left(k_x\left(x_s - D_x/2 + \Delta x\right)\right)}{k_x^2} \tag{B.19}$$

$$f^* f_{s,q}(k_x)^A_{even} = f^* \cdot f_{sq}(k_x)_{even}$$

Appendix C

Dyadic Green's Functions of Hybrid Planar/NRD-Guide Integrated Structure

The explicit form of Green's functions in spectral domain in Fig. C.1 can be obtained from Appendix A.

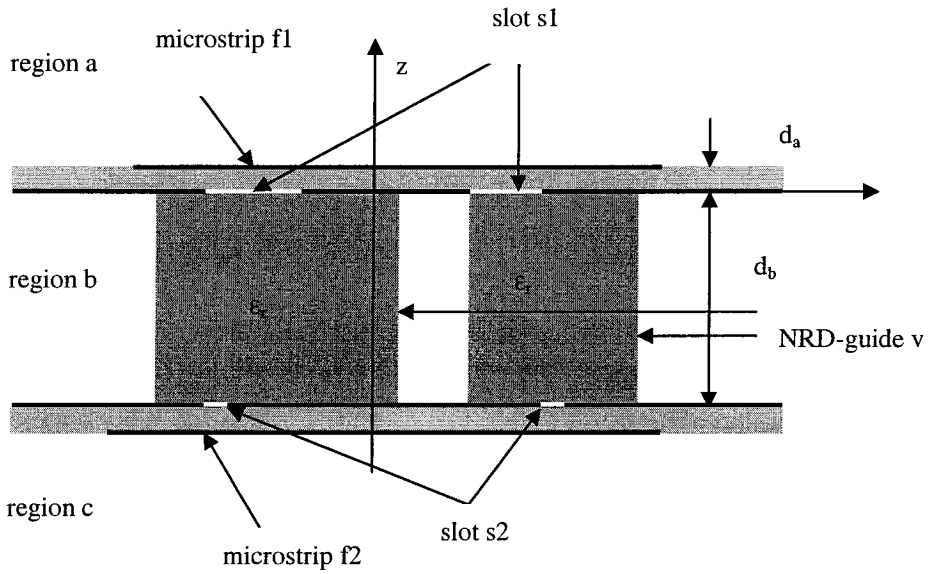

Fig. C.1. Hybrid planar/NRD-guide integrated structure

The following definitions are used in the expressions:

$$k_s^2 = \omega^2 \mu_0 \varepsilon_s$$

$$k_{1a} = \left(\varepsilon_r^a k_s^2 - k_\rho^2\right)^{1/2}, \quad \mathrm{Im}\{k_{1a}\} < 0, \ \mathrm{Re}\{k_{1a}\} > 0$$

$$k_2 = \left(k_s^2 - k_\rho^2\right)^{1/2}, \quad \mathrm{Im}\{k_2\} < 0, \ \mathrm{Re}\{k_2\} > 0$$

$$k_\rho^2 = k_x^2 + k_y^2$$

$$T_e^a = k_{1a} \cos(k_{1a} d_a) + j k_2 \sin(k_{1a} d_a)$$

$$T_m^a = \varepsilon_r^a k_2 \cos(k_{1a} d_a) + j k_{1a} \sin(k_{1a} d_a)$$

$$Z_s = (\mu_0 / \varepsilon_s)^{1/2}$$

The Green's functions in region a are as follows;

$$\tilde{G}_{xx}^{EJ} = \frac{-j\sin(k_{z1}d)}{\omega\varepsilon}\frac{(k_1^2 - k_x^2)k_{z2}\cos(k_{z1}d) + j(k_2^2 - k_x^2)k_{z1}\sin(k_{z1}d)}{T_e T_m} \tag{C.1}$$

$$\tilde{G}_{xy}^{EJ} = \frac{j\sin(k_{z1}d)}{\omega\varepsilon}k_x k_y \frac{k_{z2}\cos(k_{z1}d) + jk_{z1}\sin(k_{z1}d)}{T_e T_m} \tag{C.2}$$

$$\tilde{G}_{yx}^{EJ} = \tilde{G}_{xy}^{EJ} \tag{C.3}$$

$$\tilde{G}_{ayy}^{EJ}(k_x, k_y, d_a, d_a) = -j\frac{Z_0}{4\pi^2 k_0} \cdot \frac{(\varepsilon_r^a k_0^2 - k_y^2)k_2\cos(k_{1a}d_a) + j(k_0^2 - k_y^2)k_{1a}\sin(k_{1a}d_a)}{T_e^a T_m^a}\sin(k_{1a}d_a) \tag{C.4}$$

$$\tilde{G}_{axy}^{HJ}(k_x, k_y, 0, d_a) = \frac{1}{4\pi^2}\cdot\frac{-\varepsilon_r^a k_{1a}k_2\cos(k_{1a}d_a) + j(k_y^2(\varepsilon_r^a - 1) - k_{1a}^2)k_{1a}\sin(k_{1a}d_a)}{T_e^a T_m^a} \tag{C.5}$$

$$G_{ayx}^{EM}(k_x, k_y, d_a, 0) = -\tilde{G}_{axy}^{HJ}(k_x, k_y, 0, d_a) \tag{C.6}$$

$$\tilde{G}_{axx}^{HM}(k_x, k_y, 0, 0) = \frac{-j}{4\pi^2 k_0 Z_0}\frac{1}{k_{1a}T_e^a T_m^a}\cdot[jk_x^2 k_{1a}^2(\varepsilon_r^a - 1) + (\varepsilon_r^a k_0^2 - k_x^2) \times\{k_{1a}k_2(\varepsilon_r^a + 1)\sin(k_{1a}d_a)\cos(k_{1a}d_a) + j(\varepsilon_r^a k_2^2\sin^2(k_{1a}d_a) - k_{1a}^2\cos^2(k_{1a}d_a))\}] \tag{C.7}$$

The Green's functions in region b are as follows:

$$\tilde{\bar{\mathbf{G}}}_b^{HM}(k_x, k_y, 0, 0) = \tilde{\bar{\mathbf{G}}}_b^{HM}(k_x, k_y, -d_b, -d_b) = \frac{1}{4\pi^2}\frac{1}{k_s Z_s}\begin{bmatrix} j(k_s^2 - k_x^2)g_1 & -jk_x k_y g_1 \\ -jk_x k_y g_1 & j(k_s^2 - k_y^2)g_1 \end{bmatrix} \tag{C.8}$$

where $g_1 = \cos(k_z d_b)/(k_z \sin(k_z d_b))$. It denotes the tangential magnetic field contribution in s1(s2) from the magnetic surface current in s1(s2).

$$\tilde{\tilde{\mathbf{G}}}_b^{HM}\left(k_x,k_y,0,-d_b\right)=\tilde{\tilde{\mathbf{G}}}_b^{HM}\left(k_x,k_y,-d_b,0\right)$$
$$=\frac{1}{4\pi^2}\frac{1}{k_s Z_s}\begin{bmatrix} j\left(k_s{}^2-k_x^2\right)g_2 & -jk_xk_yg_2 \\ -jk_xk_yg_2 & j\left(k_s{}^2-k_y^2\right)g_2 \end{bmatrix} \tag{C.9}$$

where $g_2=1/\left(k_z\sin\left(k_zd_b\right)\right)$. It denotes the tangential magnetic field contribution in s1(s2) from the magnetic surface current in s2(s1).

$$\tilde{\tilde{\mathbf{G}}}_b^{EM}\left(k_x,k_y,z,0\right)=\frac{1}{4\pi^2}\begin{bmatrix} 0 & g_3 \\ -g_3 & 0 \\ -jk_yg_4 & jk_xg_4 \end{bmatrix} \tag{C.10}$$

where $g_3=\sin\left(k_z\left(z+d_b\right)\right)/\sin\left(k_zd_b\right)$ and $g_4=\cos\left(k_z\left(z+d_b\right)\right)/\left(k_z\sin\left(k_zd_b\right)\right)$. It denotes the electric field contribution in v from the magnetic surface current in s1.

$$\tilde{\tilde{\mathbf{G}}}_b^{EM}\left(k_x,k_y,z,-d_b\right)=\frac{1}{4\pi^2}\begin{bmatrix} 0 & g_5 \\ -g_5 & 0 \\ -jk_yg_6 & jk_xg_6 \end{bmatrix} \tag{C.11}$$

where $g_5=\sin\left(k_zz\right)/\sin\left(k_zd_b\right)$ and $g_6=\cos\left(k_zz\right)/\left(k_z\sin\left(k_zd_b\right)\right)$. It denotes the electric field contribution in v from the magnetic surface current in s2.

$$\tilde{\tilde{\mathbf{G}}}_b^{HJ}\left(k_x,k_y,0,z'\right)=\frac{1}{4\pi^2}\begin{bmatrix} 0 & g_7 & -jk_yg_8 \\ -g_7 & 0 & jk_xg_8 \end{bmatrix} \tag{C.12}$$

where $g_7=\sin\left(k_z\left(z'+d_b\right)\right)/\sin\left(k_zd_b\right)$ and $g_8=\cos\left(k_z\left(z'+d_b\right)\right)/\left(k_z\sin\left(k_zd_b\right)\right)$. It denotes the tangential magnetic field contribution in s1 from the volume current in v.

$$\tilde{\tilde{\mathbf{G}}}_b^{HJ}\left(k_x,k_y,-d_b,z'\right)=\frac{1}{4\pi^2}\begin{bmatrix} 0 & g_9 & -jk_yg_{10} \\ -g_9 & 0 & jk_xg_{10} \end{bmatrix} \tag{C.13}$$

where $g_9=\sin\left(k_zz'\right)/\sin\left(k_zd_b\right)$ and $g_{10}=\cos\left(k_zz'\right)/\left(k_z\sin\left(k_zd_b\right)\right)$. It denotes the tangential magnetic field contribution in s2 from the volume current in v.

$$\tilde{\tilde{\mathbf{G}}}_b^{EJ}\left(k_x,k_y,z,z'\right)=$$

$$\frac{1}{4\pi^2}\frac{Z_s}{k_s}\cdot\begin{bmatrix} j\left(k_s^2-k_x^2\right)g_{11} & -jk_xk_yg_{11} & k_xg_{12} \\ -jk_xk_yg_{11} & j\left(k_s^2-k_x^2\right)g_{11} & k_yg_{12} \\ -k_xg_{13} & -k_yg_{13} & j\left(k_x^2+k_y^2\right)g_{14}+j\delta\left(z-z'\right) \end{bmatrix} \tag{C.14}$$

where $g_{11}=\begin{cases}\sin\left(k_z\left(z+d_b\right)\right)\sin\left(k_zz'\right)/\left(k_z\sin\left(k_zd_b\right)\right) & z<z' \\ \sin\left(k_zz\right)\sin\left(k_z\left(z'+d_b\right)\right)/\left(k_z\sin\left(k_zd_b\right)\right) & z>z'\end{cases}$,

$g_{12}=\begin{cases}\sin\left(k_z\left(z+d_b\right)\right)\cos\left(k_zz'\right)/\sin\left(k_zd_b\right) & z<z' \\ \sin\left(k_zz\right)\cos\left(k_z\left(z'+d_b\right)\right)/\sin\left(k_zd_b\right) & z>z'\end{cases}$,

$g_{13}=\begin{cases}\cos\left(k_z\left(z+d_b\right)\right)\sin\left(k_zz'\right)/\sin\left(k_zd_b\right) & z<z' \\ \cos\left(k_zz\right)\sin\left(k_z\left(z'+d_b\right)\right)/\sin\left(k_zd_b\right) & z>z'\end{cases}$,

and $g_{14}=\begin{cases}\cos\left(k_z\left(z+d_b\right)\right)\cos\left(k_zz'\right)/\left(k_z\sin k_zd_b\right) & z<z' \\ \cos\left(k_zz\right)\cos\left(k_z\left(z'+d_b\right)\right)/\left(k_z\sin k_zd_b\right) & z>z'\end{cases}$. It denotes the electric field contribution in v from the polarized equivalent volume current in v.

In these Green's functions, the poles at which denominator equals to zero represent radiation modes, also referred to parallel plate waveguide modes. These poles occur at $k_zd_b=m\pi, m=0,1,2,3,\ldots$, where $k_\rho=\sqrt{k_s^2-\left(m\pi/d_b\right)^2}$ ($k_\rho^2=k_x^2+k_y^2$). There is always at least one pole which represents the m=0 continuous radiation mode in the above Green's functions. With the increasing of frequency (k_0) or increasing of the distance between two plates, $k_s>m\pi/d_b$ more poles (m≥1) will appear in these Green's functions.

The Green's functions in region c are same as that in region a.

Appendix D

Proof of Orthogonal Property

If we can show that the coupling terms in (6.7) between the slot and LSE modes are zeros, we should be able to conclude that no LSE modes can be excited in this structure. The field distribution in LSE modes are

$$E_x(x,y) = jC\omega\mu_0 (m\pi / d_b)\cos(\beta_y y)e^{-j\beta x} \tag{D.1}$$

$$E_y(x,y) = 0 \tag{D.2}$$

$$E_z(x,y) = C\omega\mu_0\beta\cos(\beta_y y)e^{-j\beta x} \tag{D.3}$$

Because $G_{xx}^{HJ}(k_x,k_y,0,z)=0$ and $E_y(x,y)=0$, only $ZY_{mk',j}^{zx}(v/s1)$ exists.

$$\begin{aligned} ZY_{mk',j}^{zx}(v/s1) &= \int_{k_x}\int_{k_y} \tilde{G}_{m,zx}^{EM}(k_x,k_y,0)\cdot \tilde{f}_{z,k'}^{*}(k_x,k_y)\cdot \tilde{f}_{x,j}(k_x,k_y)dk_x dk_y \\ &= A_z\int_{-\infty}^{\infty} M^s(k_x)\cdot f(k_x)dk_x \cdot \int_{-\infty}^{\infty} k_y M^s(k_y)\cdot g(k_y)dk_y \end{aligned} \tag{D.4}$$

We only take care of the k_y component integral and

$$M^s(k_y) = \frac{2\sin(k_y W_s/2)}{W_s k_y} \tag{D.5}$$

$$g_c(k_y) = \frac{2}{k_y^2-\beta_y^2}\left[k_y\cos(\beta_y W_v/2)\sin(k_y W_v/2) - \beta_y\sin(\beta_y W_v/2)\cos(k_y W_v/2)\right] \tag{D.6}$$

$M^s(k_y)$ and $g(k_y)$ are even functions, so the integral for k_y is zero. Then

$$ZY_{mk',j}^{zx}(v/s1) = 0 \tag{D.7}$$

Thus, no LSE modes can be excited in this structure.